ABSTRACT

Title of Dissertation:	SAMPLE-TO-ANSWER POINT-OF-CARE VIRUS DIAGNOSTIC SYSTEM USING THERMALLY RESPONSIVE ALKANE PARTITIONS
	David John Boegner Doctor of Philosophy, 2024
Dissertation directed by:	Professor Ian M. White Department of Bioengineering

Many viral infections can be accurately diagnosed using today's most sophisticated detection systems. Unfortunately, many of these detection systems fail to benefit society as a whole, but rather favor select areas of the world that are able to install and maintain the infrastructure such diagnostics require. Thus, in an effort to eliminate the barrier of access to diagnosis and treatment in low-and-middle-income areas, portable point-of-care devices are fabricated such that rapid results can be obtained without the need for bulky lab equipment or skilled technicians. An ideal point-of-care diagnostic device can easily collect an untampered sample and limits a patient's encounter with a clinician to a single visit for both the diagnosis and the treatment. Many so-called point-of-care diagnostics for blood-borne viruses first require blood sample preparation (e.g. centrifugation) prior to testing in the device. Other point-of-care devices sacrifice diagnostic accuracy in favor of speed and portability. Both cases demonstrate our inability to properly distribute the benefits of sophisticated diagnostics worldwide.

I present a solution in the form of an affordable handheld diagnostic device with the sensitivity and specificity of benchtop lab equipment and built-in automatic sample preparation. Automatic sample preparation will be achieved using thermally responsive alkane partitions, which are solid at ambient temperatures and liquid at moderately elevated temperatures. When liquid, the alkane partitions allow passage of magnetically activated microbeads coated with material that captures viruses. Despite magnetic beads with virus particles passing through, the alkane partition continues to prevent unwanted sample components (e.g. blood cells, DNases, etc.) from interfering with the virus-detecting mechanism on the other side. To address the lack of sensitivity in many point-of-care diagnostics, the virus-detecting mechanism will feature isothermal amplification which enables detection of attomolar concentrations of virus within 30 minutes without expensive thermo-cycling equipment that standard detection systems require. The novel technology described here is demonstrated in a platform which detects SARS-CoV-2 from blood, a capability currently unachievable in point-of-care settings.

SAMPLE-TO-ANSWER POINT-OF-CARE VIRUS DIAGNOSTIC SYSTEM USING THERMALLY RESPONSIVE ALKANE PARTITIONS

by

David John Boegner

Dissertation submitted to the Faculty of the Graduate School of the
University of Maryland, College Park, in partial fulfillment
of the requirements for the degree of
Doctor of Philosophy
2024

Advisory Committee:
Professor Ian White, Chair
Associate Professor Giuliano Scarcelli
Assistant Professor Jenna Mueller
Associate Professor Ryan Sochol
Professor Don DeVoe

Dedication

To my parents, profound sources of motivation, encouragement, inspiration, and love.

To my brothers and sisters, whose company brings harmony and hilarity to my life.

To my friends, past and present, who support me greatly in my endeavors.

To God, Existence itself, without whom I and my work are nothing.

Acknowledgements

My progress and accomplishments made throughout the course of my graduate studies was heavily impacted by the following individuals.

Dr. Micaela Everitt, an alum from the Amplified Molecular Sensors Lab, helped significantly in my first few years as a grad student through her mentorship, teamwork, brainstorming, and sisterly support. Other members of the lab, past and present, have improved my experience and research as well. Notably, Dr. Shannon Hilton, Evan Benke, Rachel Warren, Miso Na, and Alex Pueschel have all in their own way had a positive impact on me, whether through advice, feedback, or time to hang out and chat. Miso especially has been helpful during data collection for several aspects of my work. Dr. John Rzasa manufactured device hardware used in later portions of this work. Dr. Don DeVoe dedicated time to fruitful conversations with me regarding aspects of the earlier portions of this work. Dr. John Goertz's work (another alum from the Amplified Molecular Sensors Lab) was crucial for the success of my work in this dissertation. Dr. Anthony Harris, Dr. Robert Christenson, Dr. Coleen Damcott, Dr. Brent King, LaToya Stubbs, and Dr. Peter Rock, members of the University of Maryland School of Medicine supplied patient samples used to validate the technology developed in this dissertation. My advisor, Dr. Ian White, has been a great support and mentor who has motivated me and kept me on the right track. Through his mentorship, I have become a much better researcher and have significantly improved and diversified my skillset.

Funding for my work comes from the Fischell Department of Bioengineering, National Institutes of Health, and the Fischell Fellowship.

Table of Contents

List of Figures

Figure 8. Vertical hydrophobic channel. (A) Photograph of a melted TRAP in a vertical hydrophobic channel. (B) 2D schematic of a cross section along the center of the channel parallel to the image plane in (A) before and after melting the TRAP. (C) Data showing TRAPs that remained intact (green circles) and TRAPs that breached (red triangles) as well as the threshold (dashed line) determined by a mathematical approximation.

Figure 9. Vertical hydrophilic channel. (A) Photograph of a melted TRAP in a vertical hydrophilic channel. (B) 2D schematic of a cross section along the center of the channel parallel to the image plane in (A) before and after melting the TRAP. (C) Data showing TRAPs that remained intact (green circles) and TRAPs that breached (red triangles) as well as the threshold (dashed line) determined by a mathematical approximation.

Figure 10. (A) In a 3 x 3 mm channel, 36 μL of blue-dyed water with 0.01% Triton surfactant was loaded under 27 μL of eicosane which was under 36 μL of yellow-dyed water. (B) Image of the same device in (A) after being vertically oriented on a 60 °C hot plate until the eicosane melted. (C) In a 3 x 3 mm channel, 36 μL of blue-dyed water with 0.1% Triton was loaded under 27 μL of eicosane which was under 36 μL of yellow-dyed water. (D) Image of the same device in (C) after being vertically oriented on a 60 °C hot plate until the eicosane melted. The data suggests that the behavior of TRAPs is modified above a certain threshold of surfactant concentration.

Figure 11. Horizontal hydrophobic channel. (A) Photograph of a melted TRAP in a horizontal hydrophobic channel. (B) 2D schematic of a cross section along the center of the channel parallel to the image plane in (A) before and after melting the TRAP. (C) Data showing TRAPs that remained intact (green circles) and TRAPs that breached (red triangles) as well as the threshold (dashed line) determined by the mathematical approximation from the vertical hydrophobic case.

Figure 12. Horizontal hydrophilic channel. (A) Photograph of a melted TRAP in a horizontal hydrophilic channel. (B) 2D schematic of a cross section along the center of the channel parallel to the image plane in (A) before and after melting the TRAP. (C) Data showing TRAPs that remained intact (green circles) and TRAPs that breached (red triangles) as well as the threshold (dashed line) determined by a mathematical approximation.

Figure 13. (A) Schematic of the experiment in which a fluorescence measurement was taken before and after magnetic beads were transferred across a TRAP. (B) Data showing fluorescence values of the FAM side (green) and water side (blue) of the TRAP. N = 3. ArduCAM gain value: 12. Error bars are one standard deviation from the mean.

Figure 14. (A) Schematic depicting that fewer magnetic beads and a thicker TRAP (top) will not bridge while more beads and a thinner TRAP (bottom) may bridge, causing the two liquids to mix. (B) Data showing which experimental combinations of

TRAP thickness and bead mass in a horizontal hydrophobic channel caused TRAPs to remain intact (green circles) or bridge (red triangles). (C) Before (top) and after (bottom) photos of 64 μg of beads traveling through a 2 mm TRAP thickness with no TRAP bridging.

Figure 15. (A) Fluorescence signals of antibody-bound beads that traveled through one, two, or three TRAPs as well as a no-target control (NTC) which included beads with no antibodies that traveled through one TRAP. N = 3. ArduCAM gain value: 25. (B) Fluorescence signals of antibody-bound beads that passed through a TRAP, picked up HRP-antibodies, then passed through two rinse layers. As in (A), the background point included beads with no antibodies that traveled through one TRAP. N = 3. ArduCAM gain value: 25. Error bars are one standard deviation from the mean.

Figure 16. Absorbance data of HRP-conjugated antibodies that were attached to beads at 60 °C and 22 °C. No significant difference was observed between the two results. n = 3. Error bars are each one standard deviation from the mean. The following methods describe how these results were obtained in detail.

Figure 17. Schematic of the mechanisms within a cassette during the diagnostic test. After a blood sample is loaded into the cassette, magnetic microbeads functionalized with aptamers capture virus particles present in the sample. The temperature is increased to melt the eicosane layer, allowing a magnet to pull beads through, isolating virus particles from the blood sample. Once through, the virus particles are lysed. After lysis, the hexacosane layer is melted, initiating the LAMP reaction.

Figure 18. Photo and schematic of prototype device hardware. The photo includes a penny for scale. This device is capable of testing four samples at one time.

Figure 19. (A) Photos depicting each stage of the assay within a cassette with dyes in each solution. Magnetic beads traverse the eicosane stationary TRAP without red dye leaking through. When the hexacosane removable TRAP melts, the layers on either side quickly mix. (B) Data representing the speed at which two liquids mix upon melting a removable TRAP.

Figure 20. LAMP results from a sample of virus particles after an incubation with Proteinase K (orange curve) compared to a sample of virus particles without a Proteinase K incubation (green curve), along with a no-target control (blue curve).

Figure 21. LAMP results from a sample of virus particles after capture onto magnetic beads and transfer across a melted eicosane TRAP (orange curve) compared to transfer across an oil partition at room temperature (green curve), along with a no-target control (blue curve).

Figure 22. (A) Fluorescence data from our portable reader device plotted on an annotated graph that includes the temperature profile inside the device (dotted line). (B) Compiled results from 35 blood tests using our device.

Figure 23. COVID-19 patient plasma samples tested via RT-qPCR (x-axis) and via our sample-to-answer device (y-axis). Samples confirmed positive by RT-qPCR are colored orange while those not detected by RT-qPCR are colored blue.

Figure 24. Schematic of the Saliva-STAT diagnostic test for the SARS-CoV-2 virus. After a saliva sample is deposited into the funnel attached to a cassette, magnetic microbeads functionalized with aptamers capture virus particles present in the sample. The temperature is increased to melt the eicosane layer, allowing a magnet to pull beads through, isolating virus particles from the saliva sample. Once through, the virus particles are lysed. After lysis, the hexacosane layer is melted, initiating the LAMP reaction.

Figure 25. (A) Rendering of the assembled Saliva-STAT handheld instrument and exploded view. (B) Photo of the instrument with a sample cassette.

Figure 26. Images of a cassette with a funnel attachment as magnetic beads are pulled down in a saliva sample. The data represents the bead transfer from the saliva sample to the saliva-TRAP interface. The red color value was extracted from a small window in the images just under the bottom of the funnel hardware.

Figure 27. (A) Fluorescence readout of the bottom region in a cassette during a hexacosane melt, which causes intercalating fluorescent dye to mix with a solution of DNA. (B) The temperature profile shows that the hexacosane breaches within 1 minute of when the cassette reaches the melting point (~57 °C).

Figure 28. (A) Fluorescence curves resulting from adding 5 µL of SARS-CoV-2-spiked saliva samples directly to LAMP reaction solutions and running the reaction at 65 °C. (B) Fluorescence curves resulting from adding 5 µL of saliva-free, purified (via bead capture and rinses) SARS-CoV-2 samples.

Figure 29. LAMP in the Saliva-STAT. (A) Representative amplification curves for 500 copies and 0 copies of viral RNA in the cassette under a layer of eicosane, heated and measured in the Saliva-STAT instrument. (B) Mean times-to-positive for 0, 5, 50, and 500 copies of RNA in the Saliva-STAT cassette under a layer of eicosane, heated and measured in the Saliva-STAT instrument (N=3). Error bars represent +/- one standard deviation.

Figure 30. Compiled Saliva-STAT test results using 500 µL saliva samples with varying concentrations of SARS-CoV-2.

List of Abbreviations

ASSURED – Affordable, Sensitive, Specific, User-friendly, Rapid/robust, Equipment-free, Deliverable
CLIA – Clinical Laboratory Improvement Amendment
COVID-19 – Coronavirus Disease 2019
CoV-STAT – SARS-CoV-2 Sample-to-Answer Test
ELISA – Enzyme-Linked Immunosorbent Assay
EV – Extracellular Vesicle
FAM – 6-Carboxyfluorescein
FBS – Fetal Bovine Serum
HCV – Hepatitis C Virus
HIV – Human Immunodeficiency Virus
HRP – Horseradish Peroxidase
IgG – Immunoglobulin G
IPA – Isopropyl Alcohol
LAMP – Loop-Mediated Isothermal Amplification
LFIA – Lateral Flow Immunoassay
NAAT – Nucleic Acid Amplification Test
NTC – No-Target Control
PASC – Post-Acute Sequelae of COVID-19 (i.e. Long COVID)
PBS – Phosphate Buffered Saline
PCR – Polymerase Chain Reaction
PID – Proportional, Integral, Derivative
PK – Proteinase K
PoC – Point-of-Care
PWM – Pulse Width Modulation
qPCR – Quantitative Polymerase Chain Reaction
RT – Reverse Transcription
SARS-CoV-2 – Severe Acute Respiratory Syndrome Coronavirus 2
TRAP – Thermally Responsive Alkane Partition
TTP – Time to Positive
UDG – Uracil DNA Glycosylase
WHO – World Health Organization

Chapter 1: Introduction

Imagine, with a snap of my fingers, every person in the world suddenly knows the entirety of physical problems and diseases – communicable and noncommunicable – that they currently have. In an instant, we would all know what to do to prevent others from catching our diseases. A short time after snapping my fingers, all communicable diseases could be eradicated. No more COVID, no more HIV/AIDS, no more Hepatitis, Flu, sexually transmitted infections, tuberculosis, all of it, gone – just like that.

But there is no magic finger snap that can achieve this. Instead, we are stuck with lab tests and hospital visits. We could begin to cough or feel weak and go to the doctor to get tested. We might give a sample of saliva or blood. In many cases we go home and wait for a few days. Then we get a call or go back to the doctor for a follow-up. Then finally we get a diagnosis and a treatment plan. If my disease is communicable, I could have infected dozens of people by then. Or what if I don't want to go back to the doctor for my treatment? We have progressed significantly as a society, but this diagnostic process is far from perfect.

How close can we get to that perfect "finger-snap diagnostic," where I snap my fingers and you know what's wrong with you? I have worked hard to pinpoint obstacles and develop technology capable of dismantling several of the barriers hindering this utopian concept.

Taking a more global perspective, millions of individuals die each year due to infectious diseases. Contracting an infectious disease, especially one that is treatable, could be avoided with enough information and care. However, in many cases, those infected with potentially deadly diseases tend to have less reliable access to healthcare for diagnostics. The most accurate virus detection systems nowadays perform very well for a wide variety of diseases. Unfortunately, many areas of the world do not have access to these sophisticated diagnostics due to the technical requirements and lack of portability of modern diagnostic equipment. The situation around Hepatitis C is especially glaring. The disease can be easily cured with widely available anti-viral medication and treatment. But the vast majority of infected people around the world are unaware they have the virus in their bloodstream, which is both deadly and contagious.

Thus, in an effort to reduce the barrier of access to diagnosis and treatment, portable point-of-care diagnostics are designed to provide rapid results without the need for bulky laboratory equipment or a skilled technician. Additionally, these devices are meant to limit a patient's contact with a clinician to a single visit as the testing process is rapid enough to provide a diagnosis and treatment before the patient leaves the test site. Several attempts to design point-of-care diagnostics for blood-borne viruses and biomarkers lack a vital feature, however: "sample-to-answer." This is a term used to describe diagnostics that easily collect an untampered patient sample and provide a result without any intervention from a user. This is incredibly important for communities that lack the time, technology, and personnel to prepare a sample prior to inserting into a diagnostic device. Many so-called point-of-care diagnostics for blood-

borne viruses first require the blood sample to be diluted and/or centrifuged to transfer plasma to the diagnostic device. This cannot be considered sample-to-answer as a trained user is required to prepare the sample.

To address the lack of sample-to-answer capabilities in point-of-care diagnostic systems, this dissertation details novel technology that provides solutions to obstacles diagnostic device makers face. The first obstacle addressed is the difficulty for diagnostic devices to automatically isolate biomarkers from complex samples such as blood. This dissertation introduces and validates the effectiveness of Thermally Responsive Alkane Partitions (TRAPs) in automatic sample preparation. TRAPs are solid at ambient temperatures and liquid at moderately elevated temperatures. When liquid, the alkane partitions allow passage of magnetically activated microbeads coated with material that captures biomarkers without affecting the integrity of the partition (i.e. the liquids on either side do not mix even after pulling beads through). These alkane partitions are demonstrated in a temperature-controlled prototype portable fluorescence reader. Another obstacle in the way of effective point-of-care diagnostics is proper sensitivity without sacrificing accessibility. This work establishes an isothermal amplification technique within portable hardware. Amplification of signal is necessary for small amounts of biomarker to be detected. The isothermal nature of the amplification, in contrast with thermal-cycling detection methods such as PCR, will allow for the diagnostic device to be rapid and affordable. TRAPs and isothermal amplification are combined and demonstrated to detect SARS-CoV-2 viremia in spiked blood samples and patient plasma samples. After these novel technological advancements are described, I will then reveal an end-user-ready device which was

developed in collaboration with the Fischell Institute for Biomedical Devices and tested with SARS-CoV-2 saliva samples.

Chapter 2: Literature Review

2.1 Point-of-Care Rationale

Over the past several decades, large strides have been made in medical technological advances. Unfortunately, a large portion of these advancements fail to benefit society as a whole, but rather favor select areas which are capable of installing and maintaining resource-intensive state-of-the-art medical devices. Several charitable efforts to distribute health benefits have been made by supplying low-income areas with advanced medical devices. Although good in thought, due to a lack of proper systems for training and maintenance, as well as failure to continuously supply consumed resources (e.g. syringes, needles, blood collection tubes, etc.), up to 70% of donated medical devices end up out of service and congregate in so-called "equipment graveyards."[1,2]

The field of point-of-care diagnostics is a more pragmatic approach to providing advanced medical care to lower-income areas. In this field, we aim to create medical devices which are usable and sustainable anywhere in the world – i.e. at the point of care rather than in centralized testing facilities. The World Health Organization has set guidelines for diagnostic devices intended for use at the point of care.[3] The guidelines use the acronym, ASSURED, and state that a point-of-care diagnostic device must be Affordable, Sensitive (minimal false-negatives), Specific (minimal false-positives), User-friendly, Rapid (such that treatment options can be given during the same encounter as the test), Equipment-free (no refrigeration or other large or complicated

equipment), and Deliverable (small and resilient to mechanical disturbances in shipping).

The United States FDA has required diagnostic devices that are specifically designed to be used outside of certified labs to follow a similar set of characteristics (the Clinical Laboratory Improvement Amendment, or CLIA).[4] However, they also expand on the user-friendly aspect by stating a decentralized (i.e. point-of-care) diagnostic device must not require extensive training, precise measurements, user interpretation, or user intervention. Much of the current diagnostic device research focuses primarily on improving accuracy metrics (e.g. sensitivity and specificity). A small portion of this set of research is able to achieve rapid, affordable, and equipment-free diagnostics. However, little success is seen in this subset of research for devices that are truly user-friendly and deliverable. The following subsections detail the state of the art of several types of diagnostics, including those for protein biomarkers and nucleic acid biomarkers, both of which are targeted in virus detection systems.

2.2 Protein Biomarker Detection

Today, the most common method for PoC protein biomarker detection is the lateral flow immunoassay (LFIA). All reagents are incorporated and stabilized, implying that precise reagent transfers are not necessary. Furthermore, the wicking of the membrane enables automated sample movement without the need for fluidics equipment (see Figure 1). When the biomarker is present, a sandwich assay forms at a specific location on a paper strip, producing a visible line. As LFIAs require no wash steps, they are significantly faster and more hands-off than their gold standard counterparts, enzyme-linked immunosorbent assays (ELISAs, see Figure 2).

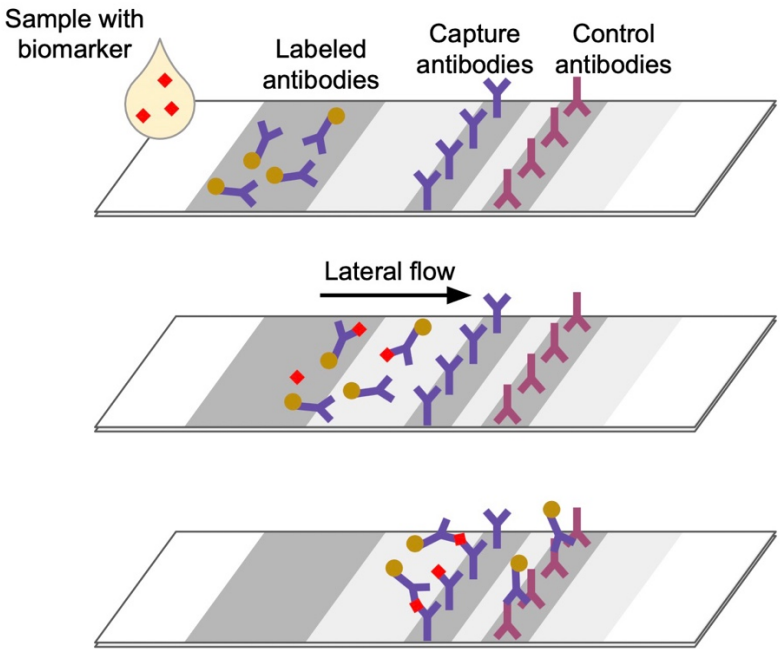

Figure 1. Schematic of a typical Lateral Flow Immunoassay (LFIA). A sample is added to the test strip and gets wicked along the membrane of the assay. Labeled antibodies automatically get added to the mix as the sample flows along the strip. These antibodies will bind to a control strip of antibodies, indicating a successful test. With biomarker present, the labeled antibodies will also bind to a capture strip of antibodies, resulting in two visible lines on the strip indicating a biomarker-positive sample for easy user analysis.

Saliva-based LFIA tests for HIV were an initial commercial success,[5] and multiple nasal swab-based COVID-19 tests quickly emerged in 2020, further proving the technology. Other applications have been reported in the literature, including diagnostics for hormones,[6,7] inflammation,[8,9] illegal substances,[10–12] bacterial infections,[13,14] and cancer.[15,16] This technology has been developed into diagnostic assays to rapidly diagnose viruses in serum or virus transport mediums such as ebolavirus[17–19] and influenza.[20–22] While saliva samples can be applied directly to the LFIA, complex raw samples like whole blood require preparation before the test can be performed.[23] Although some progress has been made to separate plasma from whole

blood by integrating a membrane-based separator into the LFIA,[24] there are no commercially available LFIAs for protein detection in whole blood that are truly sample-to-answer when using complex raw samples.

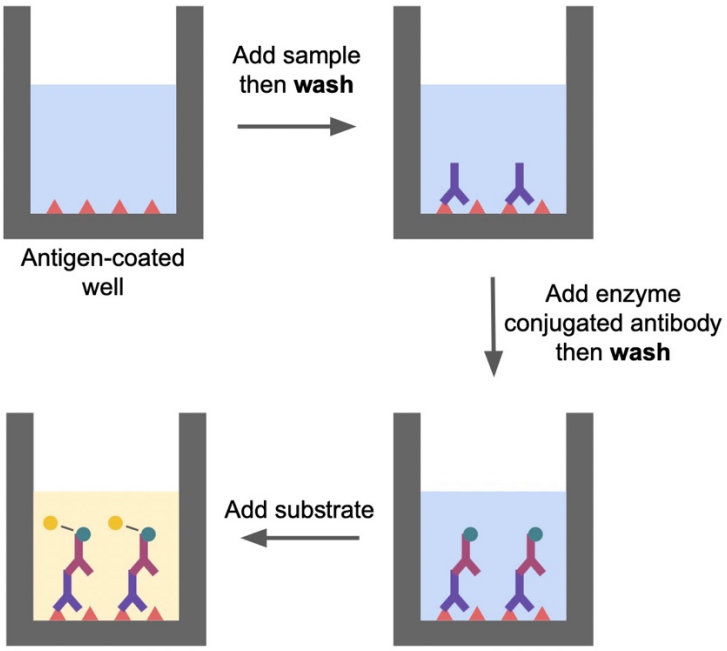

Figure 2. Schematic of an indirect Enzyme-Linked Immunosorbent Assay (ELISA). A well is coated with antigen particles to which the biomarker (target antibody) binds. After a sample is added, the solution is washed to rinse away unwanted components. Enzyme-conjugated antibodies are then added to complete the complex and the solution is washed again. Finally, substrate is added which is acted upon by the enzyme on the secondary antibody to cause a change in solution properties when the target antibody is present.

2.3 Conventional Nucleic Acid Detection

The gold standard and most common method for detecting nucleic acid biomarkers from a sample is by polymerase chain reaction (PCR).[25] In the case of RNA viruses, the RNA genome must be reverse transcribed into DNA before PCR is possible. Once the sample is adequately prepared (i.e. background material which may interfere with RT-PCR is removed), RT-PCR reagents are added to isolated viral RNA. RT-PCR first

consists of short single-stranded primers of DNA attaching onto the poly-A tail of a viral RNA genome. A reverse transcriptase enzyme then is able to extend the short strand all the way along the viral RNA, creating a complementary single-stranded DNA (ssDNA) sequence as seen in Figure 3. At this point, the reverse transcription is complete and the polymerase chain reaction can occur. An initial increase in temperature causes the two complementing strands to detach. A decrease in temperature follows, allowing the two strands to either reanneal or anneal to one of the abundant amount of short PCR primers floating in solution. These primers are designed to only attach to nucleic acid sequences of interest, contributing to the high specificity of PCR diagnostics. If each of the original strands finds a primer, a DNA polymerase enzyme then extends the primers down the length of the complementary strand, resulting in up to twice the amount of DNA. The cycling of heat is repeated and the doubling continues until the polymerase runs out of energy (reaction ATP is depleted) or more commonly until the solution runs out of primers. To monitor the progress of PCR, fluorophores are often added as one of the reagents. These fluorophores are excited and can fluoresce only when bound to DNA. Therefore, a brighter solution correlates to more DNA. In diagnostics, the size of the resulting signal is much less important than the timing of the amplification itself. The more initial DNA there is, the more likely the amplification will start earlier. Thus, the nucleic acid biomarker of interest can be quantified based on when it's PCR signal begins to rise (also known as the cycle threshold or Ct).

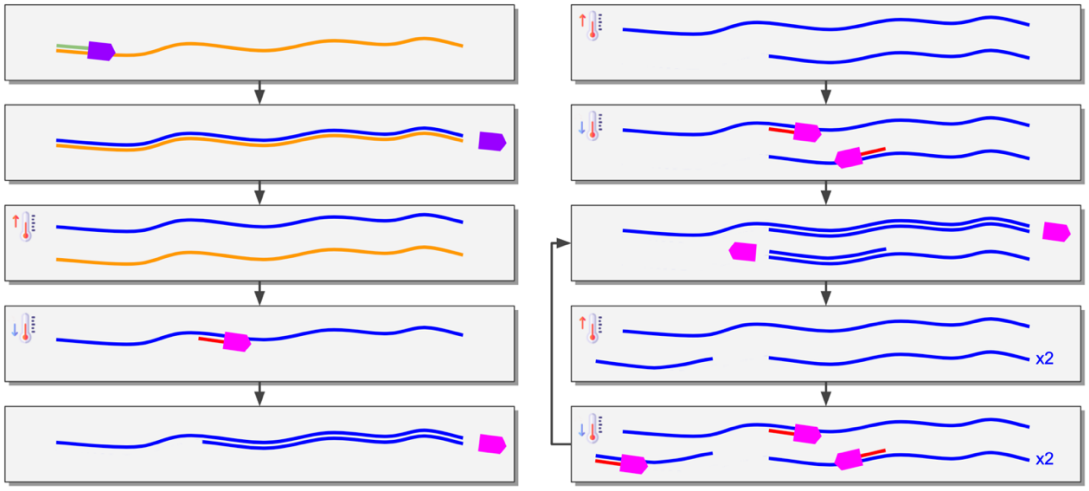

Figure 3. Schematic of a Reverse-Transcription Polymerase Chain Reaction (RT-PCR). The left column demonstrates reverse transcription. First, a reverse transcriptase enzyme (purple) extends an attached RT primer (green) into a cDNA strand (blue). Temperature is increased to melt the double strand into single strands. As the temperature cools, PCR primers anneal to the new strand, giving polymerase enzymes (pink) something to extend. At this point, as the right column depicts, a series of temperature cycling generates more and more DNA.

2.4 Point-of-Care Potential for Nucleic Acid Detection

While RT-PCR is a highly sensitive and specific virus detection system, it is far from being employable in point-of-care settings due to its requirement for a skilled technician, large & expensive equipment, and consumable resources. To eliminate the need for an expensive benchtop thermocycler, recent developments have resulted in several nucleic acid amplification techniques which do not require cycling through different temperatures. Some of the more established isothermal amplification techniques include nucleic acid sequence-based amplification (NASBA),[26] exponential strand displacement amplification (E-SDA),[27] rolling circle amplification (RCA),[28] loop-mediated isothermal amplification (LAMP),[29] helicase-dependent amplification (HDA),[30] recombinase polymerase amplification (RPA),[31] exponential amplification reaction (EXPAR),[32] and whole genome amplification (WGA).[33] Of the many

isothermal amplification methods, LAMP is among the most specific and fastest and is simple to set up, making it very ideal for point-of-care applications. LAMP can also be used to detect RNA using the same reverse transcription step in RT-PCR (called RT-LAMP).

The biochemical mechanism of LAMP is much more complicated than that of PCR. Briefly, the LAMP reaction contains three sets of two primers instead of one set of two as in PCR. Two of these primers (the inner primers FIP and BIP) are able to loop onto the DNA generated from their extension, resulting in sites for polymerase to continue generating complement DNA strands. Two outer primers (F3 and B3) are designed to bind behind the inner primers and cause the DNA extended from the outer primers to peel off already generated DNA, multiplying the amount of ssDNA that additional primers can bind to. The last set of two primers (LoopF and LoopB) is optional and takes advantage of sites on the DNA generated from the other sets of primers that allow for more DNA generation, speeding up the reaction. The single-stranded loop region is key as it allows for primers to continue to bind without requiring double-stranded DNA to heat up and separate into ssDNA. Therefore, LAMP is able to operate at a single temperature (often between 60 – 65 °C). As in PCR, fluorophores activated by the presence of DNA can be added to the reaction to monitor its progression.

Due to LAMP's single-temperature operation, devices utilizing LAMP are much easier and more affordable to fabricate than PCR devices. Controlled heating to maintain a constant temperature up to 65 °C has been achieved in portable devices using several methods. Chemical approaches, which often do not require an external

power source, utilize the combination of exothermic reactions and phase-change materials.[34,35] Temperature control is achieved by selecting a material that melts at the desired target temperature. To start the LAMP reaction, typically a user initiates the exothermic reaction by breaking a seal between the reagents. The temperature of the phase-change material increases due to the exothermic reaction but stops once it begins using thermal energy to convert phases. Thus, the device maintains the target temperature while the phase-change material melts, which is enough time for the LAMP reaction to provide a result.

Others have achieved temperature control via an electronic approach. Such designs can be open-loop where a constant DC value is sent through a small heating pad. The designs could also be closed-loop where a temperature sensor shuts off current supply to a heating pad if it reads a value higher than the desired temperature.[36]

2.5 Conventional Sample Preparation for Nucleic Acid Biomarkers

Sample preparation can sometimes be the most critical part of an accurate diagnosis. When preparing a blood sample for instance, if a lab technician accidentally pipettes more than just plasma, the resulting data could be misleading, possibly leading to a false-negative or false-positive outcome depending on the biomarker. For blood-borne viruses, the process typically starts by centrifuging a blood sample to separate out the plasma from the rest of the blood components. The plasma is then loaded into a lysis buffer which breaks open the outer shell of any virus present. This results in the release of viral RNA. This RNA often needs to be isolated from the rest of the solution since unwanted proteins may interfere with RT-PCR. One way to do this is by transporting the solution into surface-modified wells, or by introducing surface-modified

microbeads into the solution. The surface modification can be a coating of short strands of single-stranded DNA that are complementary to a portion of the viral RNA genome of interest. The matching nucleotides result in an immobilization of the viral RNA. Upon this capture, wash and rinse steps remove the unwanted material and RT-PCR reagents are then added to the isolated RNA. A schematic of this process can be seen in Figure 4.

Commercial kits[37] (e.g. Qiagen's QIAmp DNA/RNA purification kit, NucliSens isolation kit, and the Puregene DNA isolation kit) are available to help reduce the number of manual steps in a sample preparation process like the one detailed above. These kits can substantially reduce the time needed to prepare a sample, but they still cannot be applied in point-of-care settings due to their requirement for precise pipetting and lab benchtop equipment.

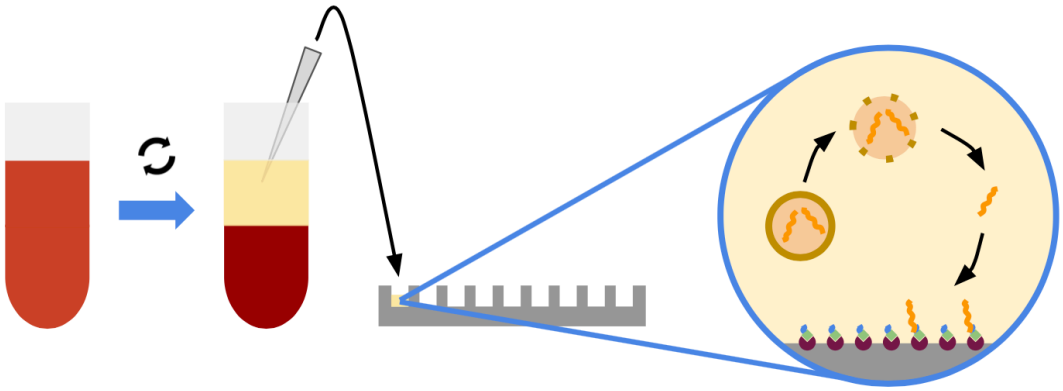

Figure 4. Schematic of blood sample preparation for nucleic acids. From left to right, a tube of blood collected from a patient is centrifuged to separate blood components. Next, blood plasma is pipetted out of the tube and placed into a well-plate. The wells include lysis buffer which breaks open the viral envelope to release viral RNA. The RNA is then immobilized onto the surface of the well via single strands of nucleic acids which are bound to the well by streptavidin-biotin bonds. From this point, the sample can then be washed and nucleic acid detection reactions can be conducted on the isolated RNA.

2.6 Point-of-Care Potential for Nucleic Acid Sample Preparation

Several attempts have been made to create point-of-care devices which can automatically prepare a sample for a nucleic acid detection. The field of microfluidics has long pursued PoC diagnostics under the premise that precise reagent transfer steps can be automated by microfluidics while biosensors can be integrated into the microsystems. Several reports demonstrate a reduction in the number of steps through non-chemical-based bacterial/viral lysis methods[17,38] and alternative DNA/RNA purification methods.[39,40] While a reduction in the number of steps represents progress, these approaches still require one or more precise reagent transfer steps. A few microfluidic methods have demonstrated sample-to-answer capabilities, but either the chips are cost-prohibitive because of the integration of complex functions, or external pumps with manual tubing exchanges are required.[39,41,42] Stumpf et al. avoided pumps and reagent exchanges using spinning disk microfluidics[43] for a sample-to-answer nucleic acid amplification test (NAAT) for Influenza A,[44] though equipment is required and that equipment can only process one sample at a time, limiting throughput. This method has been successful at reducing the cost of PCR diagnostic methods while maintaining incredible sensitivity. However, automatically distributing sample to the PCR reagents is the only part of this system that is automated. The sample inserted into the spiral channel must be cleaned and prepared beforehand; blood cannot be loaded into such a device. In another promising sample-to-answer immunoassay in the literature, Chin et al. used a low-cost plastic chip in a gold-nanoparticle-based immunoassay in which reagents are preloaded into a tube that plugs into the chip,[45] though the sample and the reagents must be loaded in separate steps by the user.

Magnetofluidics has recently emerged as a means to automate sample preparation and thus to provide hands-off assay operation in PoC diagnostics. In initial reports, ferrofluids were manipulated with magnets underneath the device surface to transport droplets of reagents along the top of a surface, enabling automatic sample preparation for NAATs.[46–49] The surface of the nanoparticles serves to bind molecules within a droplet (e.g., DNA from cell lysate) and transport them to other droplets of reagents (e.g., rinsing and elution solutions). While these clever implementations pioneered a new hands-free method of sample manipulation, the reagents are typically not enclosed and are thus susceptible to contamination, evaporation, and mechanical disturbance. A more advanced version of these magnetofluidic devices has been developed to detect HCV.[50] In this device, the necessary reagents are enclosed in a cartridge within the device, making it more robust. However, this device requires serum to be pipetted into the cartridge rather than whole blood, leaving room for further progress. Promising development from Shin, et al. demonstrates a system which immobilizes viral RNA onto magnetic beads and automatically isolates these bead-virus complexes from solution by magnetic actuation and oil partitions.[51] After rinsed and isolated, the viral RNA is then transferred to a LAMP reaction chamber where isothermal amplification takes place in the presence of positive samples. This system is far from ideal, however. First, the sample input into the device must be pipetted in after diluting by a factor of 500. A precise dilution like this requires skilled technicians and/or sophisticated lab equipment, both of which may not be available at the point of care. Also, the oil partitions used in the device are not resistant to mechanical disturbances such as vibrations during shipping. The device is not deliverable since the

cartridges will be ruined in transport. Magnetofluidic devices have been applied to screen for several diseases, including chlamydia,[51] influenza,[52] and HCV.[50] To date, however, magnetofluidics have only been applied to sample preparation for NAATs and not to immunoassays.

Reagent integration and release is also critical for the implementation of diagnostics at the point of care. A common method today for reagent integration and release is blister packs, but these require the user to release the reagents, implying that the release of multiple reagents throughout the assay would require manual interventions. As an alternative to a blister pack, Thurgood et al. demonstrated a reagent-loaded PDMS sponge that operates similar to blister packs; reagents are released by squeezing the sponge with a turned screw.[53] Automated solutions analogous to blister packs that enable automated and timed release of reagents offer a better solution for point-of-care diagnostics. One solution is to use the actuation of flexible membranes to release reagents. Chen et al. deflected an elastomeric membrane with a programmed linear actuator to drive reagents out of reservoirs,[54] while Czurratis et al. used pneumatic pressure to deflect membranes for reagent release.[55] In both cases, multilayer microfluidic chips are required, as is integration of reagents under an elastomeric layer. In the spinning disk microfluidic approach reported by Stumpf et al., aluminum foil pouches are packaged inside the microfluidic disk; when the disk achieves a particular spinning speed, the centrifugal pressure ruptures the packet, releasing the reagents into the channel.[44]

Because integrating reagents into microfluidic devices during manufacturing can be complicated, it may be desirable to have the reagents preloaded into an external

device. In work reported by Xu et al., the reagents for sample preparation preceding a NAAT were loaded into a cartridge that is attached onto the microfluidic chip before use.[56] In the reported design, however, two syringe pumps were used for reagent loading, which may be cumbersome for PoC applications. In a simpler implementation, Chin et al. integrated all reagents for an immunoassay into a tube (that plugs into the chip) in the proper order with air spacers between reagents; reagents were loaded by attaching the tube to the chips and drawing back a syringe plunger to create negative pressure.[45] Yobas et al. also used an external preloaded cartridge with air spacers and utilized peristaltic action of magnetic ball bearings to drive the liquids through the chip.[57]

2.7 Significance of Point-of-Care Technology in the Context of SARS-CoV-2

Coronavirus Disease 2019 (COVID-19), caused by the SARS-CoV-2 virus, killed at least 7 million people between 2019 and 2023, with nearly one billion documented cases.[58] Although SARS-CoV-2 is a respiratory virus, it is known to enter the circulatory system if it evades the patient's initial immune response. Numerous studies have shown that SARS-CoV-2 viremia (i.e., live virus particles in the bloodstream) is correlated with health outcomes.[59–65] A study by Cardenoso Domingo et al. showed that COVID-19 patients with SARS-CoV-2 viremia were 11.2 times more likely to have poor health outcomes and 13.5 times more likely to die.[59] In fact, in their study, all patients in the cohort who died had viremia. Similarly, another study by Jacobs et al. showed that RNA levels in blood correlated strongly with whether a COVID-19 patient was hospitalized and whether the hospitalization included the intensive care unit (ICU).[60] Li et al. reported that viremia predicted the severity of COVID-19 disease and

death in a dose-dependent manner.[61] These studies point to the significance of viremia as an indicator of health outcomes. In fact, Fajnzylber et al. showed that RNA load in blood is a better predictor of outcomes than nasopharyngeal swabs.[62]

While SARS-CoV-2 primarily infects the respiratory system, it is known to afflict the entire body and to persist in the form of post-acute sequelae of COVID-19 (PASC). In PASC, or long COVID, patients experience new, returning, or ongoing health problems four or more weeks following the initial SARS-CoV-2 infection.[66–68] Symptoms of PASC include post-exertional malaise, fatigue, brain fog, dizziness, gastrointestinal symptoms, palpitations, changes in sexual desire or capacity, loss of or change in smell or taste, thirst, chronic cough, chest pain, and abnormal movements.[68] Viremia appears to be the link between the initial respiratory infection and extrapulmonary multi-organ disease.[61] In fact, Su et al. determined that circulating SARS-CoV-2 RNA is a predicting factor for PASC.[69] Moreover, one study found that PASC patients had circulating SARS-CoV-2 RNA levels equivalent to levels at hospitalization.[70] Also, a study by Siddiqi et al. supported this as well, as 76% of patients with viremia suffered myocardial injury.[71]

It is evident that detecting SARS-CoV-2 virus (or RNA) in blood could be used as a predictor for short term and long-term health outcomes, as well as a diagnostic for PASC. Ideally, this could be implemented in the form of a point-of-care (PoC) diagnostic so that tests could be performed in walk-in clinics, emergency departments, and primary care provider offices. However, while PoC tests for COVID-19 diagnosis from nasal swabs are commercially available, PoC tests for viremia are unavailable. Viremia tests represent a significant challenge for PoC tests, as the viral load is much

lower than nasopharyngeal swabs and thus RNA amplification is required; this implies RNA purification from a blood sample. While this can be done in a sophisticated lab setting with trained technicians and expensive equipment, PoC tests must be low in cost, portable, and sample-to-answer (i.e., no user interventions).

Chapter 3: Thermally Responsive Alkane Partitions for Assay Automation

3.1 Overview

For point-of-care diagnostic tools to be impactful, they must be inexpensive, equipment-free, and sample-to-answer (i.e., require no user intervention). Here, we report a new approach to enable sample-to-answer diagnostics that utilizes thermally responsive alkane partitions (TRAPs) as automated pseudo-valves. When combined with the magnetic manipulation of microbeads, TRAPs enable the pumpless automation of all steps in complex assays. We demonstrate that in relatively narrow channel geometries, liquified alkane partitions continue to separate reagents on each side of the partition while enabling the transition of magnetic beads from one reagent to the next, replacing manual pipetting steps in conventional assays. In addition, we show that in relatively broader geometries, liquified partitions breach, enabling the addition/mixing of preloaded reagents. Through calculation and experimentation, we determine the geometric design rules for implementing the stationary and removable partitions in fluidic channels. In addition, we demonstrate that magnetic microbeads can be pulled through liquified stationary TRAPs without disrupting partition integrity and without disrupting bound protein complexes attached at the microbead surface. The TRAP technology introduced here can enable a new low-cost and equipment-free approach for fully automated sample-to-answer diagnostics.

3.2 Introduction

Despite decades of research, the commercial impact of point-of-care (PoC) diagnostics has been minimal, and numerous critical global health diagnostic needs remain unaddressed. The lack of translation from research labs to the field may be due to incorrect assumptions and prioritizations about the requirements for use at the point of care. While efforts to shrink sensors or automate functions through microfluidics aim to satisfy some of the requirements outlined by the World Health Organization's "ASSURED" criteria,[3] often, the user-friendly (U in ASSURED) point is overlooked despite its importance. In fact, in the United States, the Food and Drug Administration requires that diagnostic tests seeking approval for use outside of the central lab (i.e., to receive a CLIA waiver) must be performed without the need for precise manual steps or interventions.[4] This implies that diagnostic solutions should be sample-to-answer to enable deployment beyond the central lab. To be a viable sample-to-answer diagnostic, a system must be able to process raw samples (including whole blood), enable precise reagent transfer and mixing, and perform rinses, all without manual interventions, bulky robotics, or complex valve control.

Today, the most common method for PoC protein biomarker detection is the lateral flow immunoassay (LFIA). All reagents are incorporated and stabilized, implying that precise reagent transfers are not necessary. Furthermore, the wicking of the membrane enables automated sample movement without the need for fluidics equipment. When the biomarker is present, a sandwich assay forms at a specific location on a paper strip, producing a visible line. As LFIAs require no wash steps, they

are significantly faster and more hands-off than their gold standard counterparts, enzyme-linked immunosorbent assays (ELISAs).

Saliva-based LFIA tests for HIV were an initial commercial success,[5] and multiple nasal swab-based COVID-19 tests quickly emerged in 2020, further proving the technology. Other applications have been reported in the literature, including diagnostics for hormones,[6,7] inflammation,[8,9] illegal substances,[10–12] bacterial infections,[13,14] and cancer.[15,16] This technology has been developed into diagnostic assays to rapidly diagnose viruses in serum or virus transport mediums such as ebolavirus[17–19] and influenza.[20–22] While saliva samples can be applied directly to the LFIA, complex raw samples like whole blood require preparation before the test can be performed.[23] Although some progress has been made to separate plasma from whole blood by integrating a membrane-based separator into the LFIA,[24] there are no commercially available LFIAs for protein detection in whole blood that are truly sample-to-answer when using complex raw samples.

The field of microfluidics has long pursued PoC diagnostics under the premise that precise reagent transfer steps can be automated by microfluidics while biosensors can be integrated into the microsystems. Several reports demonstrate a reduction in the number of steps through non-chemical-based bacterial/viral lysis methods[17,38] and alternative DNA/RNA purification methods.[39,40] While a reduction in the number of steps represents progress, these approaches still require one or more precise reagent transfer steps. A few microfluidic methods have demonstrated sample-to-answer capabilities, but either the chips are cost-prohibitive because of the integration of complex functions, or external pumps with manual tubing exchanges are

required.[39,41,42] Stumpf et al. avoided pumps and reagent exchanges using spinning disk microfluidics for a sample-to-answer nucleic acid amplification test (NAAT) for Influenza A,[44] though equipment is required and that equipment can only process one sample at a time, limiting throughput. In another promising sample-to-answer immunoassay in the literature, Chin et al. used a low-cost plastic chip in a gold-nanoparticle-based immunoassay in which reagents are preloaded into a tube that plugs into the chip,[45] though the sample and the reagents must be loaded in separate steps by the user.

Magnetofluidics has recently emerged as a means to automate sample preparation and thus to provide hands-off assay operation in PoC diagnostics. In initial reports, ferrofluids were manipulated with magnets underneath the device surface to transport droplets of reagents along the top of a surface, enabling automatic sample preparation for NAATs.[46–49] The surface of the nanoparticles serves to bind molecules within a droplet (e.g., DNA from cell lysate) and transport them to other droplets of reagents (e.g., rinsing and elution solutions). While these clever implementations pioneered a new hands-free method of sample manipulation, the reagents are typically not enclosed and are thus susceptible to contamination, evaporation, and mechanical disturbance. A more advanced version of these magnetofluidic devices has been developed to detect HCV.[50] In this device, the necessary reagents are enclosed in a cartridge within the device, making it more robust. However, this device requires serum to be pipetted into the cartridge rather than whole blood, leaving room for further progress. Magnetofluidic devices have been applied to screen for several diseases,

including chlamydia,[51] influenza,[52] and HCV.[50] To date, however, magnetofluidics have only been applied to sample preparation for NAATs and not to immunoassays.

Reagent integration and release is also critical for the implementation of diagnostics at the point of care. A common method today for reagent integration and release is blister packs, but these require the user to release the reagents, implying that the release of multiple reagents throughout the assay would require manual interventions. As an alternative to a blister pack, Thurgood et al. demonstrated a reagent-loaded PDMS sponge that operates similar to blister packs; reagents are released by squeezing the sponge with a turned screw.[53] Automated solutions analogous to blister packs that enable automated and timed release of reagents offer a better solution for point-of-care diagnostics. One solution is to use the actuation of flexible membranes to release reagents. Chen et al. deflected an elastomeric membrane with a programmed linear actuator to drive reagents out of reservoirs,[54] while Czurratis et al. used pneumatic pressure to deflect membranes for reagent release.[55] In both cases, multilayer microfluidic chips are required, as is integration of reagents under an elastomeric layer. In the spinning disk microfluidic approach reported by Stumpf et al., aluminum foil pouches are packaged inside the microfluidic disk; when the disk achieves a particular spinning speed, the centrifugal pressure ruptures the packet, releasing the reagents into the channel.[44]

Because integrating reagents into microfluidic devices during manufacturing can be complicated, it may be desirable to have the reagents preloaded into an external device. In work reported by Xu et al., the reagents for sample preparation preceding a NAAT were loaded into a cartridge that is attached onto the microfluidic chip before

use.[56] In the reported design, however, two syringe pumps were used for reagent loading, which may be cumbersome for PoC applications. In a simpler implementation, Chin et al. integrated all reagents for an immunoassay into a tube (that plugs into the chip) in the proper order with air spacers between reagents; reagents were loaded by attaching the tube to the chips and drawing back a syringe plunger to create negative pressure.[45] Yobas et al. also used an external preloaded cartridge with air spacers and utilized peristaltic action of magnetic ball bearings to drive the liquids through the chip.[57]

Our lab recently reported a new method to automate the precise addition and mixing of reagents using thermally actuated single-use valves.[35,72] Reagents for the assay are initially partitioned within the assay tube by alkane layers. Upon moderate warming (e.g., >37 °C for the case of eicosane), the alkane layers liquify and float up, causing the two initially separated reagent layers to mix. We have demonstrated that the initially partitioned reagents rapidly mix through convection as the alkane layer breaches, though density and viscosity differences between liquids can slow mixing.[73] We demonstrated nucleic acid amplification assays with this methodology. More recently, the thermally responsive alkane partitions (TRAPs) have been applied for the sample-to-answer detection of circulating histones in whole blood.[74] Importantly, the TRAP technology does not require microfluidics, and thus the manufacturing and reagent integration are simple and easily scalable. However, this previously reported approach does not support continued partitioning for rinses (e.g., immunoassays) or purifications (e.g., in NAATs).

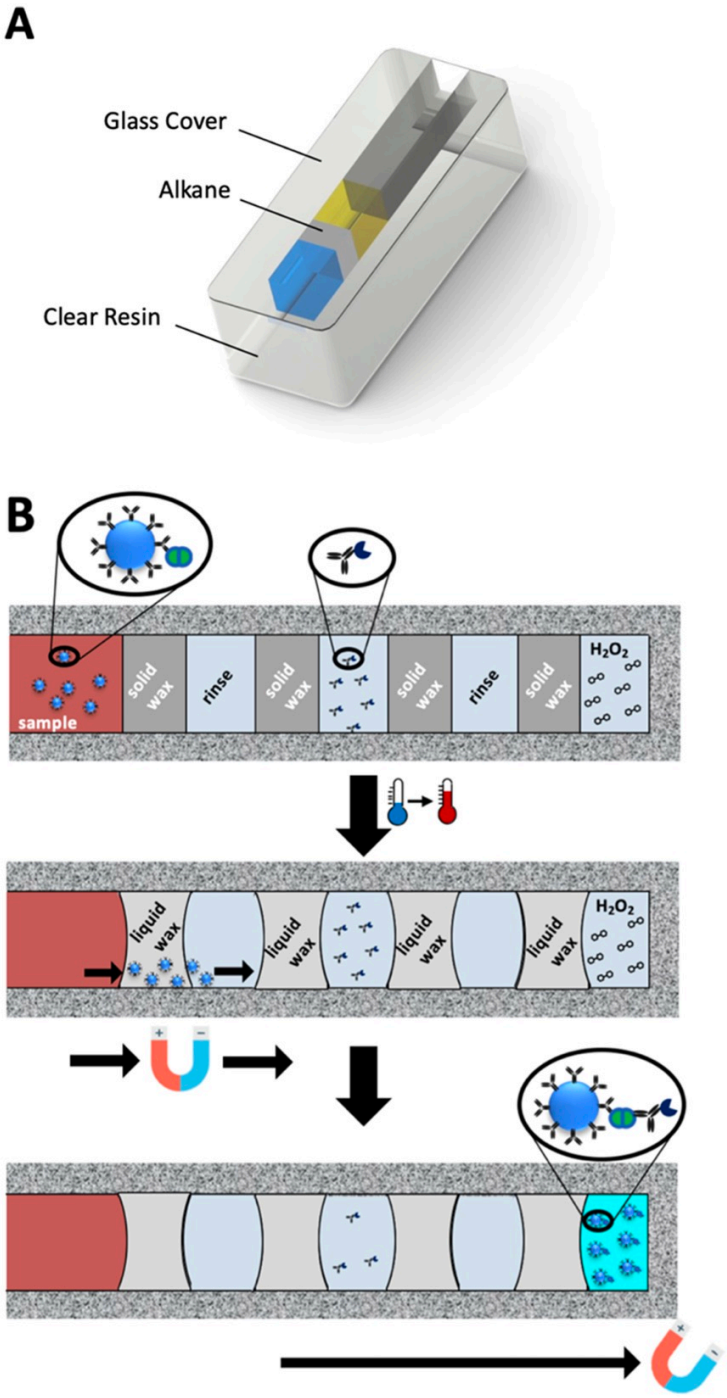

Figure 5. (A) Three-dimensional (3D) representation of a device with a TRAP partitioning two liquids. (B) Hypothetical immunoassay using TRAPS. Alkane wax layers partition all reagents. When warmed, the partitions liquify, enabling magnetic beads to be pulled from one reagent zone to the next, enabling sample-to-answer assays.

In this work, we introduce a new, more flexible form of TRAP in which liquified partitions remain in place and continue to separate reagents while magnetic beads can be pulled through the liquified partitions in a magnetofluidic assay (Figure 5). We show that the alkane partitions can continue to separate reagents when confined within sufficiently small geometries. Two previous reports have demonstrated the partitioning of reagents and magnetofluidic reagent manipulation using microfluidic systems,[17,20] though in both cases, the partition is oil (constantly liquified), which may not be stable in channels that scale beyond microfluidics. Using phase-changing alkanes as partitions, we show that the TRAPs serve as a stable partition even in broader channel geometries (which have advantages in terms of cost and ease of use), while magnetofluidic manipulation of reagents across partitions can be conducted following thermal actuation.

Herein, we establish the design rules that dictate whether the partition is removed for reagent addition or remains stationary for continual partitioning. Because of the density and polarity differences between the alkane and the aqueous reagents, the behavior is dependent upon the surface energy of the reaction vessel and the vessel orientation (i.e., vertical versus horizontal); we report design rules for all permutations of these conditions. We also investigate the design rules for pulling magnetic microbeads through liquified partitions without causing reagent breaches. Finally, we demonstrate the potential for this technology to be implemented in PoC immunoassays by validating that antibody binding remains stable as complexes are pulled through liquified TRAPs. The results reported here are expected to lead to the possibility of sample-to-answer immunoassays with complex, raw samples.

3.3 Materials & Methods

3.3.1 Materials

All devices were 3D printed with resin from Formlabs. Coverslips were obtained from Fisher Scientific. Blue and yellow dyes purchased from Wilton Color Right were used to dye water. The alkane used in these experiments was n-eicosane (melting point ~37 °C), 99%, purchased from Alfa Aesar. Streptavidin magnetic beads (1.05 μm diameter) were purchased from BioLabs. The magnet used to attract the magnetic beads was a 25.4 × 6.35 × 6.35 mm3 neodymium magnet. The glue used to adhere glass to resin was Scotch liquid super glue. Heat-inactivated fetal bovine serum (FBS) from ATCC was used as a means to hydrophilize surfaces. Amplex Red (peak absorbance wavelength: 572 nm, peak emission wavelength: 586 nm) was purchased from Biotium. Hydrogen peroxide, used to react with Amplex Red to form resorufin, was purchased from Fisher Scientific. The biotinylated rabbit IgG antibody and the HRP-conjugated anti-rabbit IgG antibody were both purchased from Thermo Fisher. The bead wash buffer was made with 25 mM Tris and 150 mM NaCl, both from Sigma-Aldrich. Finally, the phosphate buffer was made with components from JT Baker.

3.3.2 Channel Properties and Surface Modifications

Devices with various channel geometries were fabricated of resin that was 3D printed by a Form 2 stereolithography printer (Formlabs). The parts were cleaned with IPA to ensure no uncured resin remained. The outer dimensions of each device are the same (unless otherwise noted): $10 \times 8 \times 25$ mm^3. There are five different channel geometries used in this study, all 22 mm long: 2×2 mm^2, 3×3 mm^2, 4×4 mm^2, 4.5×4.5 mm^2,

and 5 × 5 mm^2. One 22 mm long face of these inner dimensions is open to air when printed and is covered by a glass coverslip, 10 mm wide, 25 mm long, and ~0.15 mm thick, glued in place. Some channels were modified to be hydrophilic; these channels were filled with FBS and soaked at room temperature for 2 h to increase hydrophilicity.

To quantify the hydrophobicity of the resin material in these experiments, the contact angle of a drop of water on a resin slab was measured. This was done by placing the slab and a drop of water onto a contact angle goniometer and recording the resulting angle. The contact angle of the untreated resin was found to be 82.0° (S.D. = 2.8°, N = 5), while the contact angle of the FBS-treated resin was measured as 38.8° (S.D. = 8.3°, N = 5), indicating an increase in hydrophilicity.

3.3.3 Investigation of TRAP Behavior for Various Channel Geometries

To investigate the behavior of TRAPs in various geometries, channels were filled with two layers of water separated by a TRAP. First, channels were filled with the respective volume of blue dyed water to fill 4 mm along the channel, as seen in Figure 6. To deposit eicosane, it was first melted and then pipetted on top of the water. Eicosane was melted by placing it in a glass vial on a hot plate at 120 °C. Melted eicosane quickly hardens when deposited atop the water, sealing the blue dyed water layer. Yellow dyed water was pipetted on top of the hardened eicosane. The volume of yellow dyed water equaled that of the blue dyed water, except for the case of the 5 × 5 mm^2 channels, for which the volume of yellow dyed water was doubled to ensure the eicosane layer never contacted air when the channel was positioned horizontally. Once filled, each device was placed on a 60 °C hot plate either horizontally (resting on the 25 × 10 mm^2 resin face) or vertically (resting on the 10 × 8 mm^2 resin face). After a short time (about 3

min), the eicosane melted and was either breached, allowing the two dyes to combine, or remained in place, preventing the two dyes from mixing. A breach is defined by green color appearing in the region near the TRAP or if any part of the TRAP was detached from the channel walls. The volume of eicosane used was experimentally varied to observe which TRAP thicknesses (calculated by dividing the volume of eicosane by the channel cross-sectional area) caused a TRAP to be breached or to stay in place.

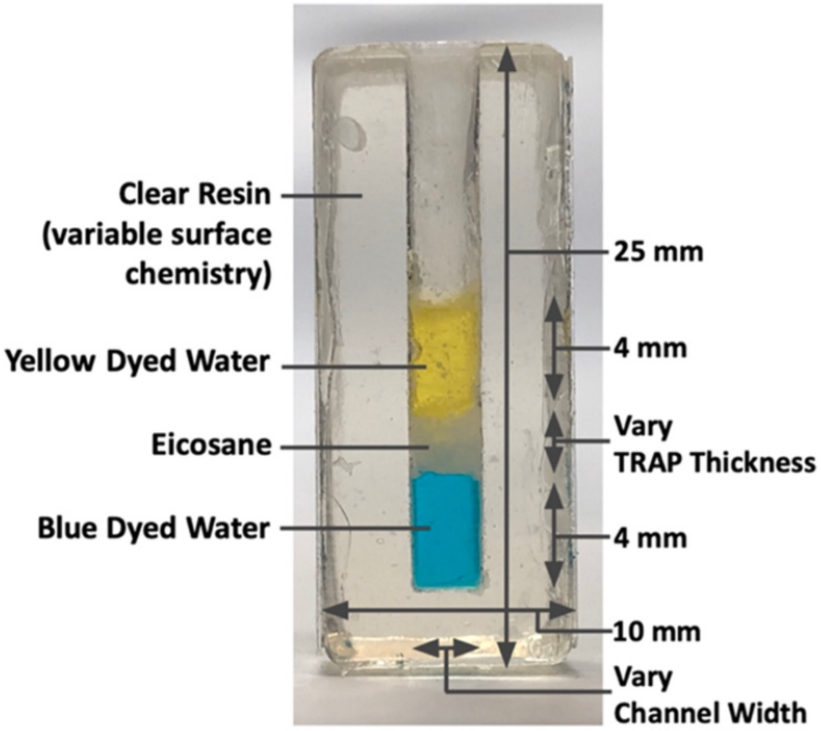

Figure 6. Labeled photograph of a TRAP with yellow dyed water on top of eicosane on top of blue dyed water.

3.3.4 Investigation of Partition Bridging Due to Magnetic Beads

To investigate the potential to use TRAPs in magnetofluidic methods, we tested the stability of stationary TRAPs and the leakage of TRAPs as magnetic beads are pulled through the liquified partitions. Water was placed in a 3 × 3 mm^2 channel such that 4 mm of the channel was filled (36 μL). Briefly, 18 μL of melted eicosane was placed on top of the water to fill another 2 mm of the channel. Then, 36 μL of a solution containing 10 μM FAM (fluorescein) and 40 μg magnetic beads in water were placed on top of the eicosane layer. The peak absorbance wavelength of FAM is 495 nm, while the peak emission wavelength is 520 nm. After the channel was set up, fluorescence measurements of both sides of the TRAP were taken. The channel was then placed on a 60 °C hot plate. Once the eicosane melted, the magnetic beads were gathered against the glass cover by holding a neodymium magnet against the glass on the outside of the channel. The magnet was then slowly moved along the glass to the other side of the TRAP at about 2 mm/s, pulling the beads along with it. The magnet was removed, and the channel was taken off the hot plate. Once the eicosane rehardened, another set of fluorescence measurements of both sides of the TRAP was taken.

To study the geometry constraints to prevent leakage, blue dyed water was placed into a 3 × 3 mm^2 channel such that 4 mm of the channel was filled (36 μL). Melted eicosane was placed on top of the water. Yellow dyed water with magnetic beads filled 8 mm of the channel on top of the eicosane (72 μL). The channel was then placed on a 60 °C hot plate. Once the eicosane melted, the magnetic beads were gathered against the glass cover by holding a neodymium magnet against the glass on the outside of the channel. The magnet was then slowly moved along the glass to the

other side of the TRAP, pulling the beads along with it. The magnet was removed, and the channel was taken off the hot plate. The TRAP was classified as "bridged" if color mixing was observed or if the eicosane had separated from the glass surface. The amount of eicosane and magnetic beads were experimentally varied to determine which combinations of partition thickness and bead mass caused the TRAP to bridge or remain intact.

3.3.5 Investigation of Immunoassay Capabilities

To determine whether antibodies in this system remain viable and maintain their function after being pulled through a TRAP (which is a nonpolar environment at an elevated temperature), we tested whether antibodies captured on magnetic beads can be transferred across one, two, and three layers of melted TRAPs without significant loss of bound antibody. 960 μg of streptavidin-coated magnetic microbeads were incubated in 1056 μL of 1000 ng/mL biotinylated rabbit IgG antibody for 90 min at room temperature. They were then washed by magnetically gathering them to the side of the tube, aspirating out the supernatant, and rinsing them with 200 μL of 25 mM Tris and 150 mM NaCl buffer three times. After the final rinse, 600 μL of 1000 ng/ mL HRP-conjugated anti-rabbit IgG antibodies in 0.1 M phosphate buffer was added to the mass of the beads and incubated for 90 min at room temperature. Then the wash step was repeated, except that after the final rinse, 65 μL of 0.1 M phosphate buffer was added to the mass of beads. A 30 μL solution of 5 μM Amplex Red and 1 mM hydrogen peroxide was added to the bottom of a $3 \times 3 \times 42$ mm^3 channel. Then, 30 μL of melted eicosane was placed on top of the solution. Three sets of three channels were designated to represent three different scenarios: magnetic beads traveling through one, two, and

three layers of melted TRAPs. In the first set, 23 μL of 0.1 M phosphate buffer and 7 μL of the antibody-bound magnetic bead solution were placed on top of the eicosane layer. In the second set, a 50 μL phosphate buffer rinse layer was placed on top of the eicosane, followed by 30 μL of melted eicosane. Then, 23 μL of phosphate buffer and 7 μL of the antibody-bound magnetic bead solution were added. In the third set, an additional rinse layer and TRAP were included. In each case, the devices were horizontally placed on a 60 °C hot plate to melt the eicosane layers. Once the eicosane was melted, the magnetic beads were gathered against the glass cover by holding a neodymium magnet against the glass on the outside of the channel. The magnet was then slowly moved along the glass to the Amplex Red layer, pulling the beads along with it. The magnet was then removed and the channel was taken off the hot plate. After 10 min, a fluorescence measurement of the final layer was taken. As a no-target control, three additional channels were prepared as follows. First, 320 μg of streptavidin-coated magnetic microbeads were washed with 200 μL of 25 mM Tris and 150 mM NaCl buffer three times and resuspended in 22 μL 0.1 M phosphate buffer. A channel with a single TRAP (as described above) was assembled, and the bead manipulation experiment was performed (as described above).

To further demonstrate the compatibility of TRAPs with magnetofluidic immunoassays, we mimicked the capture of antibodies onto beads, rinses, and detection, all in a channel with reagents partitioned by TRAPs. Three sets of three channels were prepared. For each set, 320 μg of streptavidin-coated magnetic microbeads were incubated in 352 μL of 1000 ng/mL (first set), 100 ng/mL (second set), or 0 ng/mL (third set) biotinylated rabbit IgG antibody for 90 min at room

temperature. They were then washed by gathering them to the side of the tube with a magnet, aspirating out the supernatant, and rinsing them with 200 μL of 25 mM Tris and 150 mM NaCl buffer three times. After the final rinse, 22 μL of 0.1 M phosphate buffer was added to each mass of beads. A 30 μL solution of 5 μM Amplex Red and 1 mM hydrogen peroxide was added to the bottom of a 3 × 3 × 42 mm^3 channel. Then, 30 μL of melted eicosane was placed on top of the solution. Two rinse layers were added by adding two sets of 50 μL of 0.1 M phosphate buffer separated by 30 μL of melted eicosane for partitioning. Next, 50 μL of 1300 ng/mL HRP-conjugated anti-rabbit IgG antibodies in phosphate buffer was added on top of the rinse layers and partitions, followed by 30 μL of eicosane. Then, 23 μL of phosphate buffer and 7 μL of each respective magnetic bead solution (sets one, two, and three) were placed on top. Each channel was placed horizontally on a 60 °C hot plate. Once the eicosane was melted, a magnet gathered the beads and was slowly moved along the glass until the beads reached the HRP-antibody layer. The channels were then removed from the hot plate and the beads were left to incubate for 30 minutes. After the incubation, the channels were placed on the hot plate again, and the beads were gathered and transferred across both rinse layers and into the Amplex Red and peroxide layer. After 10 minutes, a fluorescence measurement of the final layer was taken. The three background control points for this experiment were prepared the same way as the no-target control points from above. Note that with 320 μg of streptavidin-coated magnetic microbeads, the saturating protein concentration according to the manufacturer is 440 ng, which would be 1.25 μg/mL (much higher than what was used here and much higher than would be detected in typical immunoassays).

3.3.6 Fluorescence Measurements & Image Processing

All fluorescence measurements were taken by placing a device into a portable fluorescence reader designed in-house (modified from Everitt et al., 2021[74]), shown in Figure 7 (schematic and photo). The device consists of a 3D printed support that houses an ArduCAM MT9M001 Camera with an ArduCAM USB2 Camera Shield (ArduCAM), a longpass filter (Thorlabs) on the lens of the camera (530 nm for the FAM readings or 570 nm for the Amplex Red readings), two LEDs to excite the sample (470 nm for the FAM readings or 525 nm for the Amplex Red readings), and a support that secures a device in a precise location relative to the camera.

Image processing was performed with a MATLAB script that automatically cropped an image to a 64 × 80 pixel window (for the FAM experiment) or a 24 × 40 pixel window (for the Amplex Red experiments), which only contained the region of interest along a channel. Fluorescence values reported in this paper were calculated by taking the mean of the set of all grayscale pixel values within the pixel window.

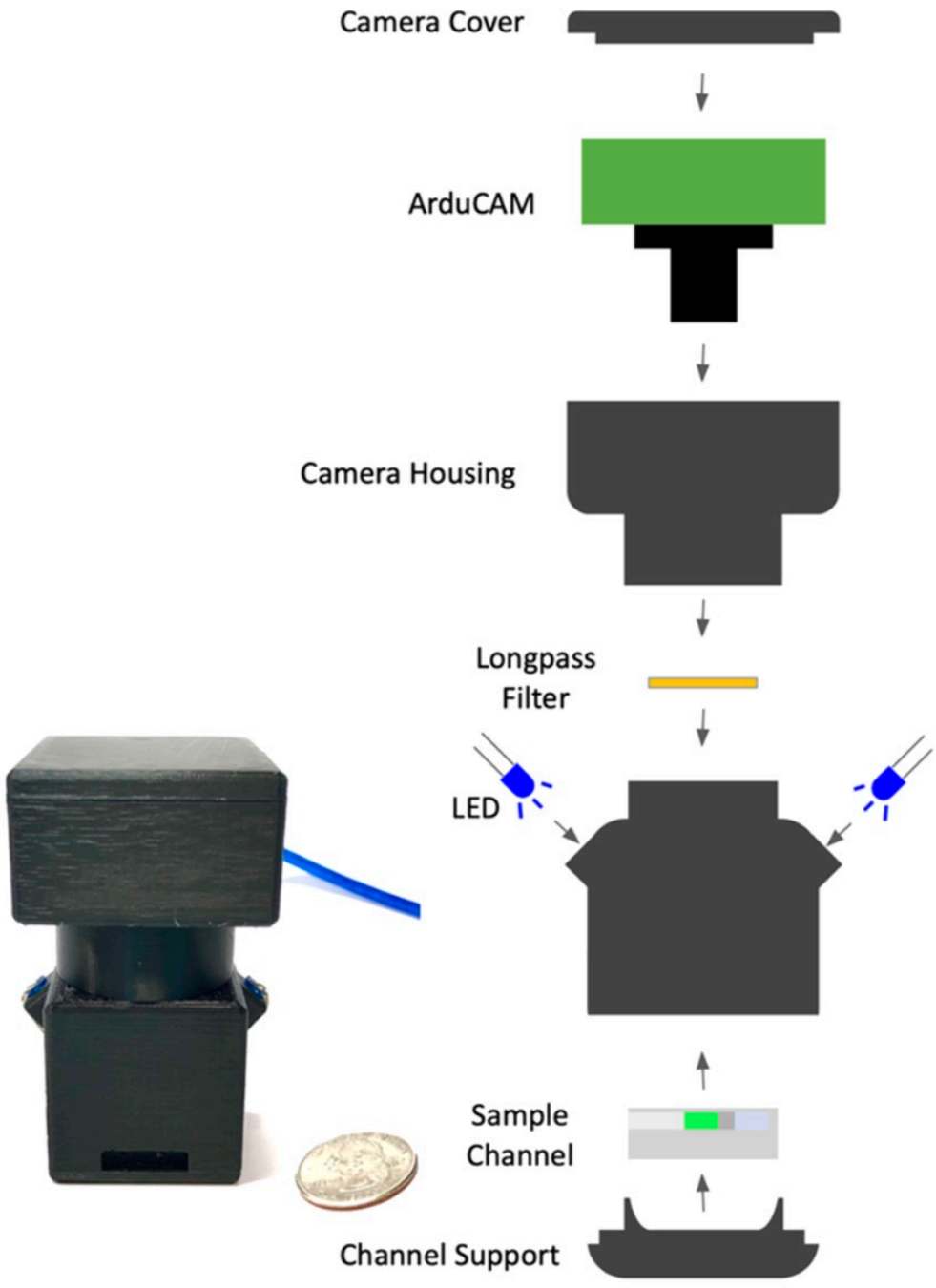

Figure 7. Photograph and schematic of the in-house designed portable fluorescence reader used in this work, with a US quarter for scale.

3.4 Results & Discussion

Our previous work using alkane to initially separate assay reagents in microtubes showed that wax liquification led to a partition breach in which reagents could automatically be added and mixed on-demand.[35,72–74] We hypothesized that in a narrower channel, surface tension and the hydrophobic interactions between wax and resin would keep the liquified alkane partition in place despite the density difference between it and the surrounding liquids. Here, we determine the geometric design rules, mathematically and experimentally, that govern when the liquified alkane barrier continues to partition and when it breaches, promoting reagent mixing.

3.4.1 Vertical Hydrophobic Channel

We start by considering a vertically oriented channel with hydrophobic channel walls (Figure 8A). We observed that because of the hydrophobic surface, the liquified eicosane formed a concave meniscus at each aqueous interface, as shown in Figure 8B. The angle of the water-eicosane boundary against the wall at a corner (θ) was measured to be 45° with a standard deviation of 5.9°. Because of the meniscus shapes, we concluded that as the partition thickness (P) decreases, the thickness of the partition at the center point will reach zero for a non-zero partition thickness, thus causing a breach in the TRAP and allowing the two initially separated layers to mix. To mathematically predict the threshold partition length (P_{th}) that determines whether a breach will occur, the following assumptions were made: (1) the meniscus at a water-eicosane interface is a portion of the surface of a sphere constrained by the square cross section of a channel whose centerline includes the center of the sphere (see the red dashed curve in Figure 8B) and (2) breaching only occurs when the two meniscuses touch along the

centerline of the channel (i.e., when $P_n - 2h = 0$, where P_n is the distance between the two meniscuses at a corner of the channel, and h is the depth of a meniscus at the centerline of the channel, as depicted in Figure 8B). P_{nw} denoted in Figure 8B is similar to P_n but is the distance between the two aqueous layers along the center of the channel wall as opposed to along the corner ($P_{nw} < P_n$). Equation 1 dictates how the threshold value of the partition thickness P_{th} varies with respect to the channel width D and contact angle θ, which is the angle between the eicosane and water at a corner of the channel (Figure 8B). It is important to note that the cross section schematic seen in Figure 8B is parallel to the image plane in Figure 8A; since the angle calculations for θ were done at the corners of the channel, our equation operates along the diagonal of the channel, hence the use of √2 D.

Equation 1

$$P = \frac{\sqrt{2}\,D}{cos(\theta)}(1 - sin(\theta)) - \frac{\pi}{6\sqrt{2}\,D} \times \frac{1 - sin(\theta)}{cos(\theta)}\left(\left(\frac{3}{4}\sqrt{2}\,D\right)^2 + \left(\frac{1}{2}\sqrt{2}\,D \times \frac{1 - sin(\theta)}{cos(\theta)}\right)^2\right)$$

We assembled TRAPs in channels with varying TRAP thicknesses and channel geometry and observed whether the TRAP breached upon liquification. The data from the experiment confirms the predictive ability of the mathematical derivation. As shown in Figure 8C, when an eicosane partition in the channel has a partition thickness below the estimated threshold, the melted eicosane layer breaches and allows the liquids to mix (Figure 8C, red triangles). When the partition thickness is above the estimated threshold, the melted eicosane remains intact, and no mixing occurs (Figure 8C, green circles). We note that the dashed line in Figure 8C is a geometric approximation. As the channel becomes thinner (e.g., 2 mm), the assumed spherical

geometry is imperfect, and the partition breaches for a slightly thicker TRAP than predicted.

The data in Figure 8C demonstrates that we can predictably produce TRAPs that either remain intact or breach by controlling the channel width and TRAP thickness. Since the TRAPs remain intact at relatively small partition thicknesses, the vertical hydrophobic channel appears to be well-suited for continually partitioning reagents in sample-to-answer magnetofluidic immunoassays. They can also serve as removable TRAPs simply using a wider channel geometry.

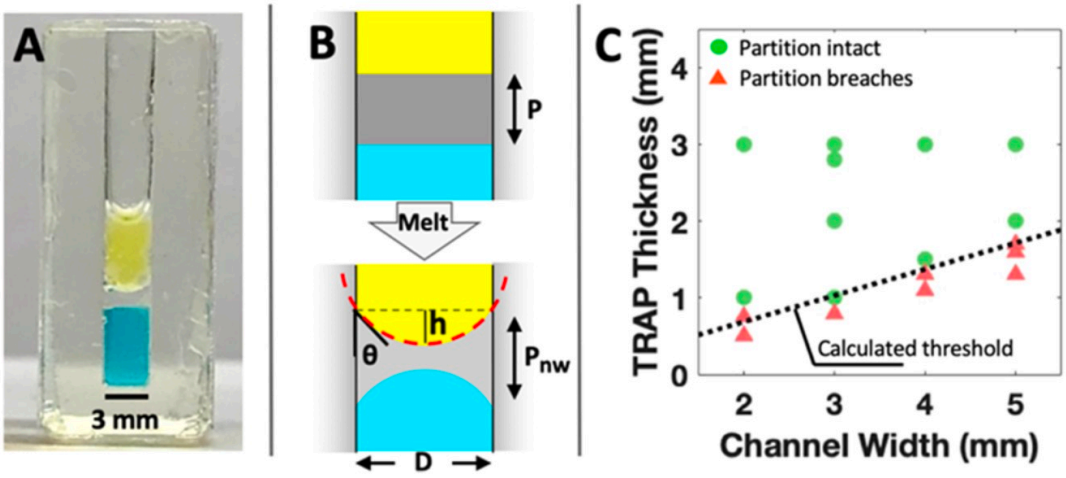

Figure 8. Vertical hydrophobic channel. (A) Photograph of a melted TRAP in a vertical hydrophobic channel. (B) 2D schematic of a cross section along the center of the channel parallel to the image plane in (A) before and after melting the TRAP. (C) Data showing TRAPs that remained intact (green circles) and TRAPs that breached (red triangles) as well as the threshold (dashed line) determined by a mathematical approximation.

3.4.2 Vertical Hydrophobic Channel

We demonstrated that TRAPs can maintain partitioning capability in a vertical channel despite gravity, due to surface tension and the hydrophobic interactions between wax

and resin. Next, we investigated the behavior of the system when the channel has a hydrophilic wall surface. In this case, the hydrophilic wall caused liquid wax to separate off of the wall, especially at thinner partition thicknesses (Figure 9). This enabled breaching along the corners of the channel and ultimately led to floating wax in many cases. To mathematically predict the threshold that determines whether a breach will occur given a certain partition thickness and square channel width, the following assumptions were made: (1) the wax will form a sphere and float up through the water with no interference from channel walls and (2) with interference from channel walls, the wax will only remain in place as a partition when the radius of the sphere it would become given the input volume equals the length from the center of the channel to a corner. Equation 2, which determines the threshold partition length at which a TRAP will breach, is derived by equating the threshold input volume ($D \times D \times P_{th}$) with the assumed spherical shape that forms when the wax melts and attempts to break free of the channel walls (see Figure 9B). The threshold, P_{th}, is plotted as a dashed black line in Figure 9C. The experiments confirm the predictive capability of this equation. Most combinations of partition thickness and channel width that were below the threshold line resulted in the mixing of the two initially partitioned liquids (Figure 9C red triangles). Likewise, most combinations of partition thickness and channel width that were above the threshold line resulted in a stationary partition that prevented the two liquids from mixing.

Equation 2

$$P = \frac{\sqrt{2}}{3}\pi D$$

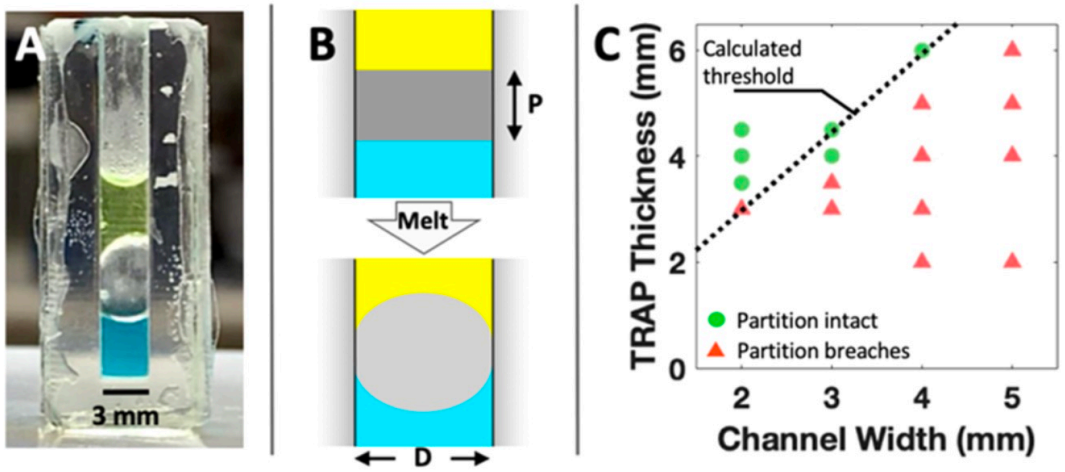

Figure 9. Vertical hydrophilic channel. (A) Photograph of a melted TRAP in a vertical hydrophilic channel. (B) 2D schematic of a cross section along the center of the channel parallel to the image plane in (A) before and after melting the TRAP. (C) Data showing TRAPs that remained intact (green circles) and TRAPs that breached (red triangles) as well as the threshold (dashed line) determined by a mathematical approximation.

Comparing the results in Figure 9 with those in Figure 8, it is clear that in the hydrophobic channel, the hydrophobic interactions assist in the stabilization of the alkane position (this is further validated in that the addition of surfactant to the water causes the hydrophobic channel to behave like the hydrophilic channel, Figure 10). In the hydrophilic channel, the behavior is dictated only by the balance of gravity and surface tension. The stability in the narrower channels suggests that at this scale, surface tension is still dominant (i.e., Bond number Bo < 1), though, as the channel width approaches 1 cm, gravity appears to dominate[72] (Bo > 1).

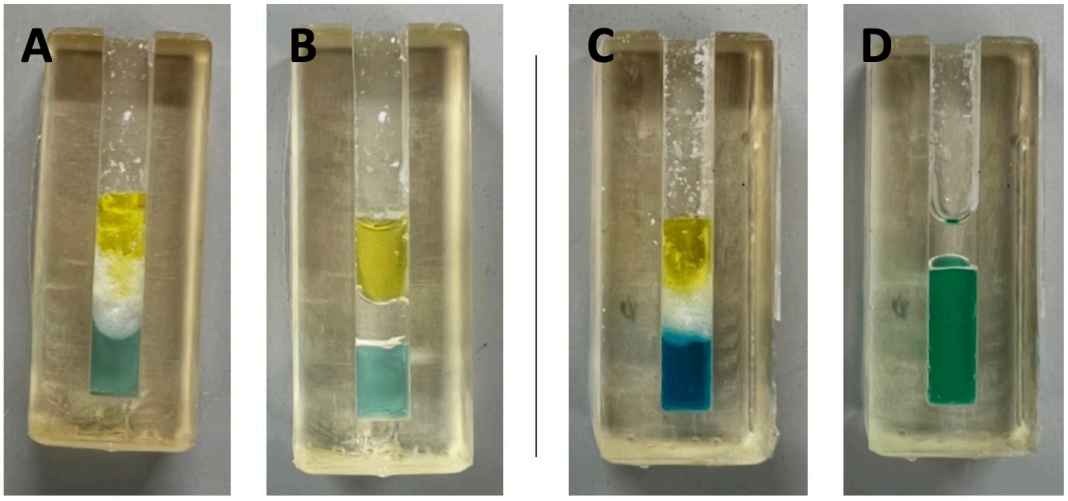

Figure 10. (A) In a 3 x 3 mm channel, 36 µL of blue-dyed water with 0.01% Triton surfactant was loaded under 27 µL of eicosane which was under 36 µL of yellow-dyed water. (B) Image of the same device in (A) after being vertically oriented on a 60 °C hot plate until the eicosane melted. (C) In a 3 x 3 mm channel, 36 µL of blue-dyed water with 0.1% Triton was loaded under 27 µL of eicosane which was under 36 µL of yellow-dyed water. (D) Image of the same device in (C) after being vertically oriented on a 60 °C hot plate until the eicosane melted. The data suggests that the behavior of TRAPs is modified above a certain threshold of surfactant concentration.

3.4.3 Horizontal Hydrophobic Channel

The experiments above (Figures 8 and 9) demonstrate the impact of surface energy on the behavior of the liquified partition. Because gravity also plays an important role in the behavior of the liquified partitions, we repeated the above investigations for a channel placed horizontally. We begin by analyzing the case of a hydrophobic channel surface. In this case, the meniscuses observed in the vertical hydrophobic case were present again; however, under the influence of gravity, these meniscuses are asymmetric, with more wax along the top wall of the channel, especially in larger channel widths (Figure 11A,B). Thus, we conclude that when the partition thickness is thin enough, the breach still occurs near the center of the channel. Because the

breaching behavior is similar to the vertical hydrophobic case and since the asymmetry due to gravity is not as prevalent in smaller channel widths, we used the same mathematical analysis as in the vertical hydrophobic case. As expected, this model matches with the data at smaller channel widths but is less accurate when predicting the behavior at larger channel widths (>3 mm; at broader channel widths, the alkane is able to float up slightly, causing it to deviate from the assumed geometry in the prediction). The experimental results demonstrate that, as one might expect, TRAPs in a horizontally oriented hydrophobic channel are well-suited for continually partitioning reagents in sample-to-answer magnetofluidic immunoassays. They can also serve as removable TRAPs simply using a wider channel geometry.

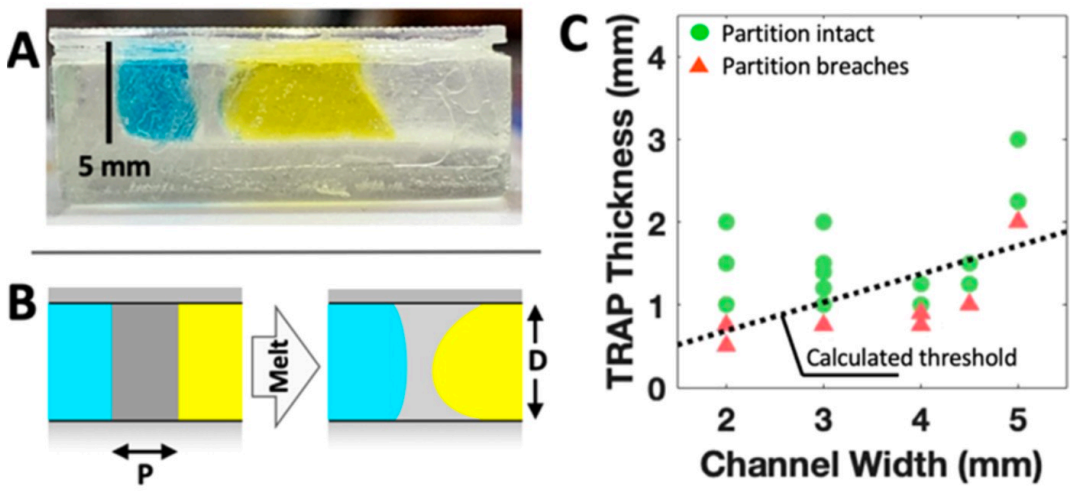

Figure 11. Horizontal hydrophobic channel. (A) Photograph of a melted TRAP in a horizontal hydrophobic channel. (B) 2D schematic of a cross section along the center of the channel parallel to the image plane in (A) before and after melting the TRAP. (C) Data showing TRAPs that remained intact (green circles) and TRAPs that breached (red triangles) as well as the threshold (dashed line) determined by the mathematical approximation from the vertical hydrophobic case.

3.4.4 Horizontal Hydrophilic Channel

Following the horizontal hydrophobic channel experiments, we then repeated the analysis for horizontal hydrophilic channels. These channels resulted in similar wax behavior as the vertical hydrophilic case in which the wax tended to detach from the channel walls and form a spherical shape when subjected to no external interference. However, since gravity is now in a perpendicular direction relative to the length of the channels, the sphere of wax floats up against the surface of the glass cover, forming the bulged shape seen in Figure 12A. We observed that the wax sealed the channel when this bulge shape pressed against the sidewalls of the channel such that the wax reached all corners of the channel. At this point, the wax in contact with a sidewall formed a near-semicircular shape. This semicircle cross section of the TRAP maintained roughly the same shape throughout the width of the channel at the threshold between sealed and unsealed, increasing in area slightly at the center of the channel.

Because of this, our mathematical analysis estimates the volume of the wax at the threshold as the area of a semicircle (whose diameter d equals the channel width D) times the channel width with an adjustment factor, α, which modifies the equation to account for deviations in the cross section from a perfect semicircle across the width of a channel. α is necessary because of the combinations of partition thicknesses and channel widths that result in an almost broken TRAP; in this domain, eicosane surface tension forces cause a liquid bridge to form that extends the eicosane semicircle shape toward the wall, sealing the channel even though the geometry would result in a semicircle with a radius smaller than the width of the channel. Equating this formula to the volume of the input wax ($D \times D \times P$) and setting $\alpha = 0.9$ (determined empirically)

results in Equation 3, plotted as a dashed black line in Figure 12C. The data matches well with the mathematical approximation; each TRAP above the threshold line remained intact (Figure 12C green circles), and most points below the line allowed the liquids to mix (Figure 12C red triangles). As with the vertical hydrophilic channels, these horizontal hydrophobic channels result in relatively unstable partitions. Thus, this arrangement is also suitable for applications in which the partition is to be removed to automate precise reagent additions and mixing.

Equation 3

$$P = \frac{\pi}{2} D$$

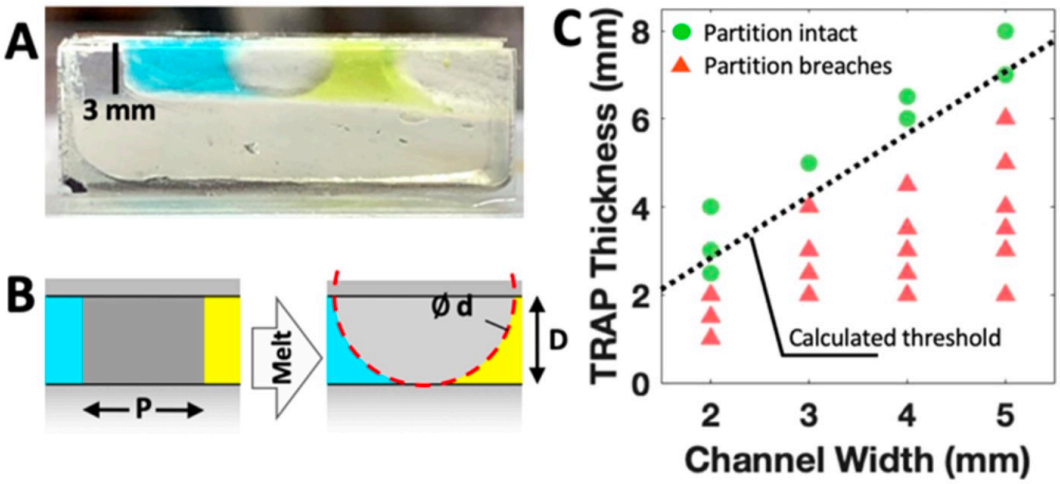

Figure 12. Horizontal hydrophilic channel. (A) Photograph of a melted TRAP in a horizontal hydrophilic channel. (B) 2D schematic of a cross section along the center of the channel parallel to the image plane in (A) before and after melting the TRAP. (C) Data showing TRAPs that remained intact (green circles) and TRAPs that breached (red triangles) as well as the threshold (dashed line) determined by a mathematical approximation.

3.4.5 Volumetric Limitations

TRAP designs that breach can be used to store and release reagents in assays. Based on the geometry requirements for TRAPs that breach, we hypothesize that there are also geometric requirements for the aqueous reagent volume. In the vertical hydrophobic channel, the 4 × 4 mm^2 design will breach with a TRAP of less than 1.5 mm thick. In that experiment, about 50 μL of aqueous volume was used for each reagent layer.

We explored limits on the smallest amount of liquid that could be stored and released in this system. A horizontal 4 × 4 mm^2 channel was prepared as described in the channel geometry investigation in the methods mentioned above, except that only 10 μL of blue dyed water was placed below a 0.75 mm TRAP (12 μL eicosane). In this setup, the TRAP breached and the liquids mixed. It would be difficult to implement volumes smaller than 10 μL in this geometry; for smaller volumes, we observed that the surface tension of the polar liquid prevents it from contacting the walls of a channel. When the aqueous volume does not contact the entire channel surface, the TRAP layers on each side of the stored volume merge during manufacturing. Similarly, we anticipate that a sample volume that does not contact all walls may not result in proper mixing. However, we note that the channel width can be modulated along the length to reduce the cross section of the aqueous reagent so that volume requirements can be reduced.

3.4.6 Device Robustness

To confirm the resilience against mechanical disturbances of the device used in this study, the following experiment was conducted. A 3 × 3 mm^2 channel with a 2 mm TRAP (18 μL eicosane) between blue dyed water and yellow dyed water was prepared as described in the channel geometry investigation in the methods above. An additional

2 mm TRAP was placed on top of the yellow dyed water to seal the liquid in place. Once the eicosane hardened, the device was dropped from 20 cm five times, followed by five 40 cm drops, followed by five 3 m drops. The device was unaffected by each drop, i.e., the liquid and eicosane layers had no visible changes after the drops.

3.4.7 Continual Partitioning for Magnetofluidics

The experiments above (Figures 8 and 11) demonstrate that when confined in small hydrophobic channels, the TRAPs remain stationary upon liquification. We hypothesized that the liquified partitions would be permeable to magnetic beads driven by an external magnet and would remain stationary as the beads are pulled through, thus continuing to partition the solutions while the beads are transferred from one solution to another. To verify this capability, we constructed a channel in which a TRAP partitioned water and an aqueous solution with the fluorophore FAM; magnetic beads were also loaded into the FAM solution. The handheld fluorescence reader (Figure 7) was used to measure the fluorescence on both sides of the partition before and after the magnetic beads were pulled through the TRAP. As shown in Figure 13, the beads were pulled from one side of the partition to the other without disturbing the partition. Furthermore, no fluorescence change is measurable on the destination side of the partition, suggesting that the TRAP continued to partition during the bead transfer.

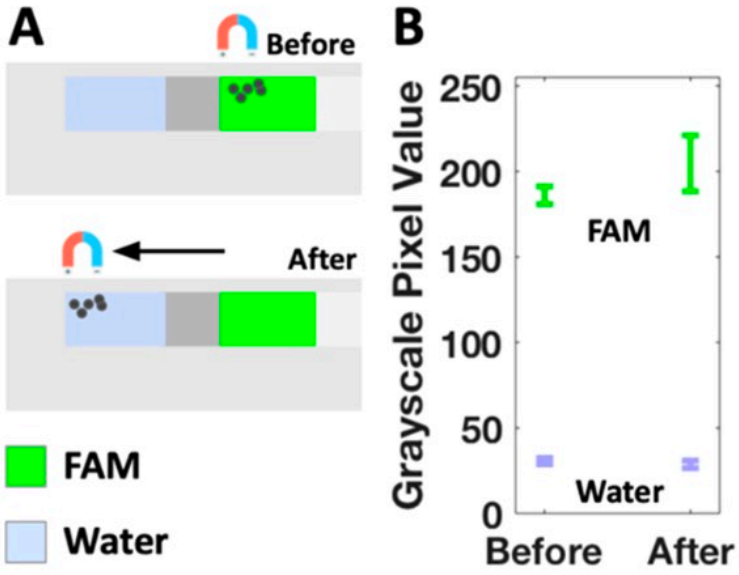

Figure 13. (A) Schematic of the experiment in which a fluorescence measurement was taken before and after magnetic beads were transferred across a TRAP. (B) Data showing fluorescence values of the FAM side (green) and water side (blue) of the TRAP. N = 3. ArduCAM gain value: 12. Error bars are one standard deviation from the mean.

While the system in Figure 13 shows continued partitioning, we hypothesized that if the partition length is short enough and if the bead cluster volume is large enough, bridging between the partitioned zones can occur (Figure 14A). Thus, the geometric design rules must also account for this possibility. To investigate this, we varied the partition thickness and the bead volume and determined which conditions resulted in breaching of the partition. As shown in the photo in Figure 14B, an eicosane partition initially separated blue and yellow dyed liquid; after warming the eicosane, the beads were pulled from the yellow to the blue liquid. In the photo in Figure 14B, no bridging occurred, as is apparent by the continued isolation of the two colors. Bridging occurs when the cluster of beads that is pulled across a TRAP connects the two liquids on either side; the TRAP does not reseal once the two aqueous layers are

bridged. As expected, the data in Figure 14C demonstrates that thinner partitions and larger quantities of beads led to bridging (red triangles). These experimental results serve to supplement the data in Figures 8 and 11 when designing continually partitioning TRAPs for magnetofluidic assays.

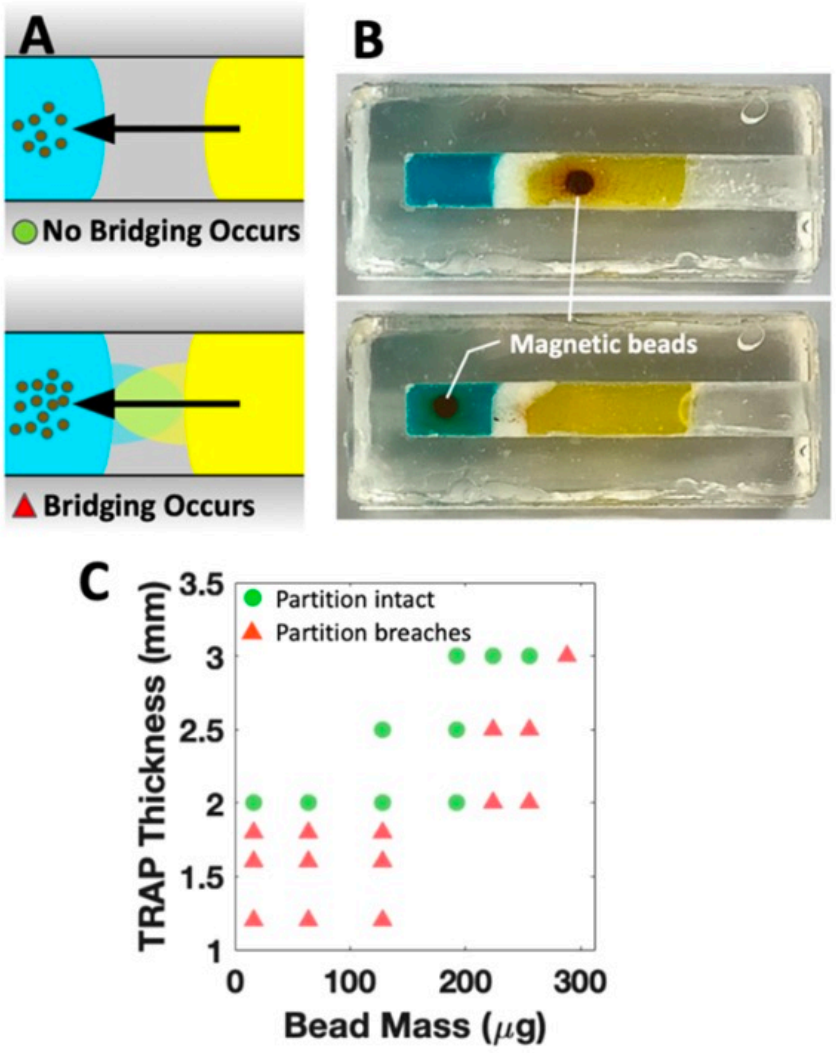

Figure 14. (A) Schematic depicting that fewer magnetic beads and a thicker TRAP (top) will not bridge while more beads and a thinner TRAP (bottom) may bridge, causing the two liquids to mix. (B) Data showing which experimental combinations of TRAP thickness and bead mass in a horizontal hydrophobic channel caused TRAPs to remain intact (green circles) or bridge (red triangles). (C) Before (top) and after (bottom) photos of 64 μg of beads traveling through a 2 mm TRAP thickness with no TRAP bridging.

3.4.8 Immunoassay Capabilities

The permeability of the liquid partitions to magnetic beads suggests the potential to operate as a pseudo-valve in an immunoassay in which magnetic beads pull bound protein complexes through multiple reactions and rinse layers. Potential barriers to this functionality are the temperature of the liquid alkane and the nonpolar nature of the alkane, as both of these characteristics could cause proteins to denature and release from bound complexes. To assess the stability of protein complexes as they are pulled through TRAPs, we assembled an antibody complex onto magnetic beads and pulled them through multiple TRAPs. HRP-conjugated anti-rabbit IgG antibodies were bound to rabbit IgG antibodies that were attached to the beads via biotin-streptavidin linkage. The complex was transferred across different numbers of TRAPs to determine whether the system would allow antibodies to be pulled across without loss due to denaturation/unbinding. The number of TRAPs was varied to observe the fraction of antibodies lost from beads at each partition. The data in Figure 15A demonstrate no significant difference between fluorescence signals of the antibody-bound beads after traveling through one TRAP, as well as through subsequent numbers of TRAPs. This suggests that the bound protein complexes remain stable as they pass through the alkane partitions, despite the nonpolar environment and increased temperature (Figure 16 further demonstrates that the temperature increase alone does not disrupt the bound complex on the beads).

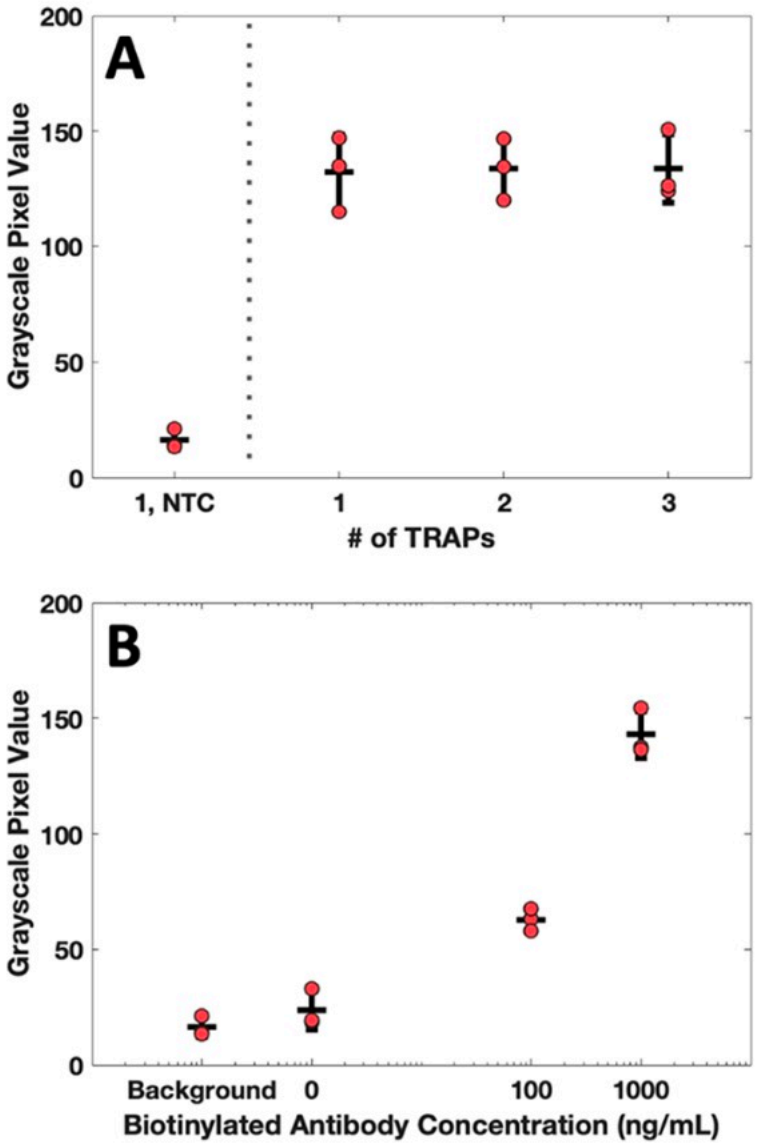

Figure 15. (A) Fluorescence signals of antibody-bound beads that traveled through one, two, or three TRAPs as well as a no-target control (NTC) which included beads with no antibodies that traveled through one TRAP. N = 3. ArduCAM gain value: 25. (B) Fluorescence signals of antibody-bound beads that passed through a TRAP, picked up HRP-antibodies, then passed through two rinse layers. As in (A), the background point included beads with no antibodies that traveled through one TRAP. N = 3. ArduCAM gain value: 25. Error bars are one standard deviation from the mean.

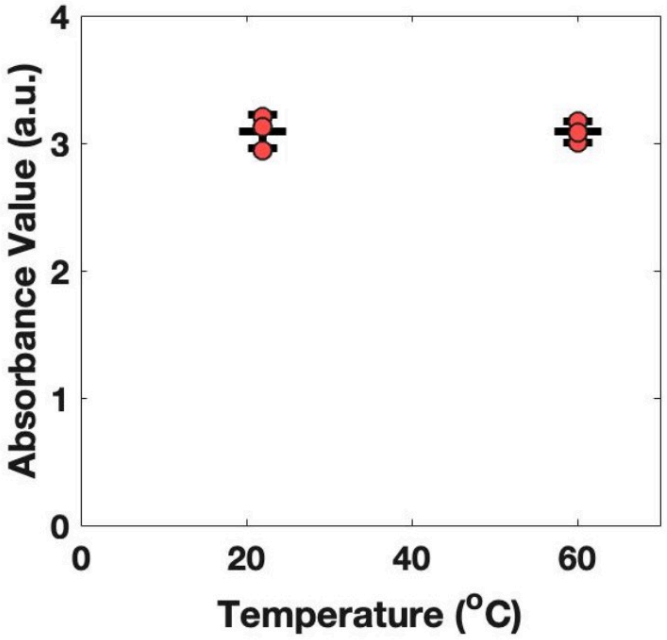

Figure 16. Absorbance data of HRP-conjugated antibodies that were attached to beads at 60 °C and 22 °C. No significant difference was observed between the two results. n = 3. Error bars are each one standard deviation from the mean. The following methods describe how these results were obtained in detail.

To further illustrate that the TRAP technology is viable for sample-to-answer magnetofluidic immunoassays, we demonstrated that antibody-functionalized magnetic beads could capture HRP-labeled antibodies and pull them through TRAPs and into a detection zone. Magnetic beads with rabbit IgG were pulled through a TRAP into a zone with anti-rabbit IgG antibodies. After a brief incubation, the beads were pulled through three TRAPs and two rinse zones (between the TRAPs) into a detection zone containing Amplex Red. The results for two different rabbit IgG concentrations are shown in Figure 15B, along with a negative control (beads with no antibodies). As expected, more signal is produced when more biotinylated antibodies are bound to the beads. The clear difference between the three concentrations indicates that the magnetic beads specifically captured secondary antibody from one aqueous zone, carried it

through rinse layers, and delivered it to a detection zone, as would be done in a magnetofluidic immunoassay.

3.5 Conclusions

There continues to be a need for fully automated sample-to-answer technology to enable PoC diagnostics from complex samples. Here, we have introduced a new approach to assay automation using thermally actuated alkane pseudo-valves. We determined the geometric thresholds that dictate whether a TRAP design results in a stationary, continually partitioning TRAP or a removable TRAP. Geometric models were validated by experiments for each of four cases that included hydrophobic and hydrophilic vertically and horizontally oriented channels. The results demonstrate that through simple geometric design, one can reliably implement TRAPs that remain stationary upon liquification (but permeable to magnetic microbeads) as well as TRAPs that are removable upon liquification (for automatically combining reagents). We further investigated stationary TRAPs for magnetofluidic immunoassays, demonstrating that beads can be pulled through stationary TRAPs without disrupting partition integrity and without disrupting bound protein complexes, including antibody labeling. Taken together, the results demonstrate that thermally actuated alkane partitions can be leveraged to construct fully automated sample-to-answer magnetofluidic assays.

In future work, fully automated assays can be implemented using the TRAP technology, as the control is simple. First, the portable reader developed in this work can be expanded to include a motorized magnet or electromagnet array to automatically manipulate the magnetic beads along the channel. Heating elements under the control

of a microcontroller can also be integrated in alignment with the TRAPs to liquify the partitions. The portable reader is separate from the chip (which contains the TRAPs and reagents) and thus is reusable. Simple sample addition should also be considered in the design, though for the biomarker concentration to be determined precisely, the sample volume should be known.

We also note that more complicated assays than what was demonstrated here can be implemented with the TRAP technology. Here, we showed components of a simple immunoassay that utilized only the stationary TRAPs. Assays that use the stationary TRAPs to support rinse zones in addition to removable TRAPs for reagent addition can easily be implemented by modulating the channel cross section along the length of the channel. That is, a stationary TRAP can be located in a thin section of the channel, while a removable TRAP can be located in a broader section of the same channel. Ultimately, through simple engineering to assemble a fully automated handheld control unit and designing variable channel widths (using the geometric design rules reported here), point-of-care diagnostic tools that perform sophisticated assays can be developed from the TRAP technology.

Chapter 4: Sample-to-Answer Detection of SARS-CoV-2 Viremia using Thermally Responsive Alkane Partitions

Reprinted from an accepted submission to Analytical Chemistry: "Sample-to-Answer Detection of SARS-CoV-2 Viremia using Thermally Responsive Alkane Partitions" by D. Boegner, M. Na, A. Harris, R. Christenson, C. Damcott, B. King, L. Stubbs, P. Rock, and I. White. Accepted 2024.

4.1 Overview

The diagnosis of bloodborne viral infections (viremia) is currently relegated to central labs because of the complex procedures required to detect viruses in blood samples. The development of point-of-care diagnostics for viremia would enable patients to receive a diagnosis and begin treatment immediately instead of waiting days for results. Point-of-care systems for viremia have been limited by the challenges of integrating multiple precise steps into a fully automated (i.e. sample-to-answer), compact, low-cost system. We recently reported the development of thermally responsive alkane partitions (TRAPs), which enable the complete automation of diagnostic assays with complex samples. Here we report the use of TRAPs for the sample-to-answer detection of viruses in blood using a low-cost portable device and easily manufacturable cassettes. Specifically, we demonstrate the detection of SARS-CoV-2 in spiked blood samples, and we show that our system detects viremia in COVID-19 patient samples with good agreement to conventional RT-qPCR. We anticipate that our sample-to-answer system can be used to rapidly diagnose SARS-CoV-2 viremia at the point of care, leading to better health outcomes for patients with severe COVID-19 disease, and that our system can be applied to the diagnosis of other life-threatening bloodborne viral diseases, including Hepatitis C and HIV.

4.2 Introduction

Coronavirus Disease 2019 (COVID-19), caused by the SARS-CoV-2 virus, killed at least 7 million people between 2019 and 2023, with nearly one billion documented cases.[58] Although SARS-CoV-2 is a respiratory virus, it is known to enter the circulatory system if it evades the patient's initial immune response. Numerous studies have shown that SARS-CoV-2 viremia (i.e., live virus particles in the bloodstream) is correlated with health outcomes.[59–65] A study by Cardenoso Domingo et al. showed that COVID-19 patients with SARS-CoV-2 viremia were 11.2 times more likely to have poor health outcomes and 13.5 times more likely to die.[59] In fact, in their study, all patients in the cohort who died had viremia. Similarly, another study by Jacobs et al. showed that RNA levels in blood correlated strongly with whether a COVID-19 patient was hospitalized and whether the hospitalization included the intensive care unit (ICU).[60] Li et al. reported that viremia predicted the severity of COVID-19 disease and death in a dose-dependent manner.[61] These studies point to the significance of viremia as an indicator of health outcomes. In fact, Fajnzylber et al. showed that RNA load in blood is a better predictor of outcomes than nasopharyngeal swabs.[62]

While SARS-CoV-2 primarily infects the respiratory system, it is known to afflict the entire body and to persist in the form of post-acute sequelae of COVID-19 (PASC). In PASC, or long COVID, patients experience new, returning, or ongoing health problems four or more weeks following the initial SARS-CoV-2 infection.[66–68] Symptoms of PASC include post-exertional malaise, fatigue, brain fog, dizziness, gastrointestinal symptoms, palpitations, changes in sexual desire or capacity, loss of or change in smell or taste, thirst, chronic cough, chest pain, and abnormal movements.[68]

Viremia appears to be the link between the initial respiratory infection and extrapulmonary multi-organ disease.[61] In fact, Su et al. determined that circulating SARS-CoV-2 RNA is a predicting factor for PASC.[69] Moreover, one study found that PASC patients had circulating SARS-CoV-2 RNA levels equivalent to levels at hospitalization.[70] Also, a study by Siddiqi et al. supported this as well, as 76% of patients with viremia suffered myocardial injury.[71]

It is evident that detecting SARS-CoV-2 virus (or RNA) in blood could be used as a predictor for short term and long-term health outcomes, as well as a diagnostic for PASC. Ideally, this could be implemented in the form of a point-of-care (PoC) diagnostic so that tests could be performed in walk-in clinics, emergency departments, and primary care provider offices. However, while PoC tests for COVID-19 diagnosis from nasal swabs are commercially available, PoC tests for viremia are unavailable. Viremia tests represent a significant challenge for PoC tests, as the viral load is much lower than nasopharyngeal swabs and thus RNA amplification is required; this implies RNA purification from a blood sample. While this can be done in a sophisticated lab setting with trained technicians and expensive equipment, PoC tests must be low in cost, portable, and sample-to-answer (i.e., no user interventions).

For decades the field of microfluidics has pursued PoC diagnostics for nucleic acid amplification tests (NAATs) with an aim to miniaturize and automate diagnostic methodologies. However, commercial success has been elusive due to the challenges of meeting the requirements of low-cost, portability, and sample-to-answer. Numerous groups have been able to implement most or all of the required steps on chip,[75–80] but many still require off-chip lysis, manual interventions, expensive microfluidic devices,

and peripheral equipment. Two notable sample-to-answer NAAT demonstrations are Stumpf et al., who reported a sample-to-answer test for Influenza A using spinning disk microfluidics,[44] and Tang et al., who reported a sample-to-answer test for SARS-CoV-2 in saliva.[81] However, to our knowledge there are still no demonstrations of sample-to-answer PoC systems that can detect viruses directly from whole blood samples using microfluidics.

In recent years, magnetofluidics has emerged as a potential solution for sample-to-answer diagnostics. Magnetic actuation of molecularly functionalized paramagnetic beads through various reagents may eliminate pipetting steps as well as the need for pumps. In the earliest realizations of magnetofluidics, ferrofluids on top of an open device surface were manipulated with magnets underneath the device.[46–49,52] The primary application for these devices was to bind DNA/RNA from a lysate, transport it through rinse solutions and into an elution solution for a NAAT. More recently, magnetofluidics has been implemented within enclosed cassettes or chips, which offer a more pragmatic implementation. Generally, these implementations use oil to separate aqueous reagent layers; paramagnetic beads can be pulled through oil layers from one reagent to the next without disturbing the partitions. Multiple reports have demonstrated integration of some of the sample preparation steps with NAATs using microfluidic channels.[82–84] However, manufacturing of microfluidic chips with integrated oil partitions may be challenging. In an alternative approach, Shin et al. have demonstrated the use of multi-well cassettes with an oil layer covering the wells to maintain partitioning; an external magnet transfers beads from each well to the next to

perform sample preparation and qPCR.[50,85] Trick et al. incorporated a filter onto the cassette to enable compatibility with whole blood samples.[86]

We have developed a magnetofluidic approach for sample-to-answer from complex samples that does not require pumps or microfluidics, and that is stable to device agitation. This approach is enabled by Thermally Responsive Alkane Partitions (TRAPs), which we described and characterized in previous work.[87] A TRAP is solid at ambient temperature and liquid at a moderately elevated temperature, specific to the type of alkane. When melted in between two partitioned liquids in a millimeter-scale channel, if thin enough the TRAP will breach and the two liquids on either side will combine (i.e. a removable TRAP). This behavior enables automatic controlled reagent combination. At the same time, if the TRAP is sufficiently thick, the melted TRAP will continue to partition the two liquids (i.e. a stationary TRAP). In this state, the TRAP becomes permeable to magnetic microbeads but continues to partition aqueous reagents. We have proven that magnetically transferring beads (~1 μm diameter) across a TRAP causes minimal leakage that can be further negated with the addition of rinse layers.

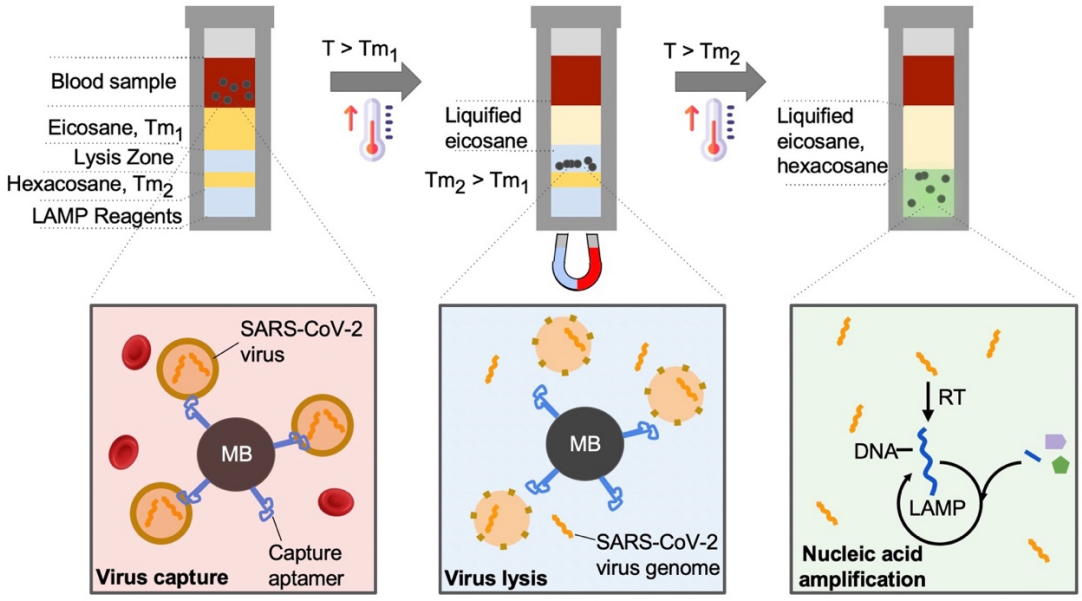

Figure 17. Schematic of the mechanisms within a cassette during the diagnostic test. After a blood sample is loaded into the cassette, magnetic microbeads functionalized with aptamers capture virus particles present in the sample. The temperature is increased to melt the eicosane layer, allowing a magnet to pull beads through, isolating virus particles from the blood sample. Once through, the virus particles are lysed. After lysis, the hexacosane layer is melted, initiating the LAMP reaction.

We previously applied removable TRAPs to detect circulating histones in blood,[74] and we applied stationary TRAPs to create a portable PoC system to detect SARS-CoV-2 antibodies from whole blood.[88] The current work refines the TRAP system to be more robust, more user-friendly, and more capable. Specifically, we demonstrate for the first time sample-to-answer detection of SARS-CoV-2 viremia in a low-cost portable format. To do this, we combine both TRAP behaviors described above (removable and stationary), as illustrated in Figure 17. Virus isolation from a whole blood sample is achieved by capturing virus onto aptamer-functionalized paramagnetic microbeads and magnetically pulling the beads through a melted stationary TRAP. We show effective virus particle lysis via an incubation with Proteinase K. Automatic initiation of reverse transcription loop-mediated isothermal

amplification (RT-LAMP) is accomplished by combining reagents upon melting a removable TRAP following lysis. Finally, we demonstrate the PoC system's ability to distinguish SARS-CoV-2-positive and SARS-CoV-2-negative spiked whole blood samples as well as patient blood plasma samples collected during the height of the COVID-19 pandemic.

4.3 Materials & Methods

4.3.1 Materials

Cassettes were fabricated by cutting an acrylic sheet with 24 mm thickness (McMaster-Carr) into 6.35 mm diameter cylinders each with a channel 3.2 mm in diameter and 23 mm deep via CNC. The alkanes in this work include n-eicosane (melting point ~37 °C), 99%, and n-hexacosane (melting point ~57 °C), 99%, both from ThermoFisher Scientific. Pierce™ Streptavidin Magnetic Beads (1.05 μm diameter) were purchased from ThermoFisher Scientific. Antarctic Thermolabile Uracil DNA Glycosylase (UDG) was purchased from NEB and is used throughout this work paired with DNA amplification reactions that result in nucleic acid products containing uracil bases. UDG helps reduce the risk of carry-over contamination from previous DNA amplification reactions. WarmStart® Multi-Purpose LAMP/RT-LAMP Master Mix with UDG was purchased from NEB. Thermolabile Proteinase K was also purchased from NEB. Mineral oil (light, lab grade) was purchased from VWR. Gamma-irradiated SARS-CoV-2 was supplied as a ~10^9 copies/mL stock solution from BEI Resources. The biotinylated SARS-CoV-2 RBD aptamer[89] used in this work as well as LAMP

primers for the N15 gene[90] were purchased from IDT and their sequences can be found below.

Biotinylated CoV2-RBD-4C aptamer

5'–ATCCAGAGTGACGCAGCATTTCATCGGGTCCAAAAGGGGCTGCTCGGG
ATTGCGGATATGGACACGTTTTTTTT /3Bio/ – 3'

LAMP Primers (N15 gene)

FIP 5' – TGCTCCCTTCTGCGTAGAAGCCAATGCTGCAATCGTGCTAC – 3'
BIP 5' – GGCGGCAGTCAAGCCTCTTCCCTACTGCTGCCTGGAGTT – 3'
F3 5' – AGATCACATTGGCACCCG – 3'
B3 5' – CCATTGCCAGCCATTCTAGC – 3'
LF 5' – GCAATGTTGTTCCTTGAGGAAGTT – 3'
LB 5' – GTTCCTCATCACGTAGTCGCAACA – 3'

4.3.2 RT-LAMP Reaction

Based in part on the recommended protocol from the NEB website, our benchtop LAMP tests consisted of the following procedure. A solution containing 1X WarmStart® Multi-Purpose LAMP/RT-LAMP Master Mix with UDG (NEB), 1X LAMP Fluorescent Dye (NEB), and LAMP primers (1.6 μM FIP/BIP, 0.2 μM F3/B3, and 0.4 μM LoopF/B) for the N15 gene is created using nuclease-free water to reach the appropriate concentrations. The volume made equals 20 μL times the number of samples being tested plus one to account for possible pipetting error. After vortexing the solution, 20 μL is loaded into PCR tubes. Then 5 μL of each sample is added to each tube. Finally, each tube is inserted into a MiniOpticon (Bio Rad) which heats the solutions to 65 °C for 60 minutes while recording the fluorescence of each solution (one reading every 30 seconds).

4.3.3 Portable Controller and Reader Device

The device used in this work consists of an ArduCAM MT9M001 Camera with an ArduCAM USB2 Camera Shield, a 530 nm longpass filter (Thorlabs), four 470 nm blue LEDs (one for each sample cassette), a DS18B20 digital temperature sensor, a pair of 30 mm x 40 mm polyimide heaters (DWEII) positioned about 8 mm from the inserted cassettes, and two 10 mm tall neodymium magnet cylinders 25 mm in diameter (K & J Magnetics) initially positioned below the inserted cassettes. Components are housed in a 3D printed casing that fits in the palm of a hand. A photo of the device and an exploded view are shown in Figure 18.

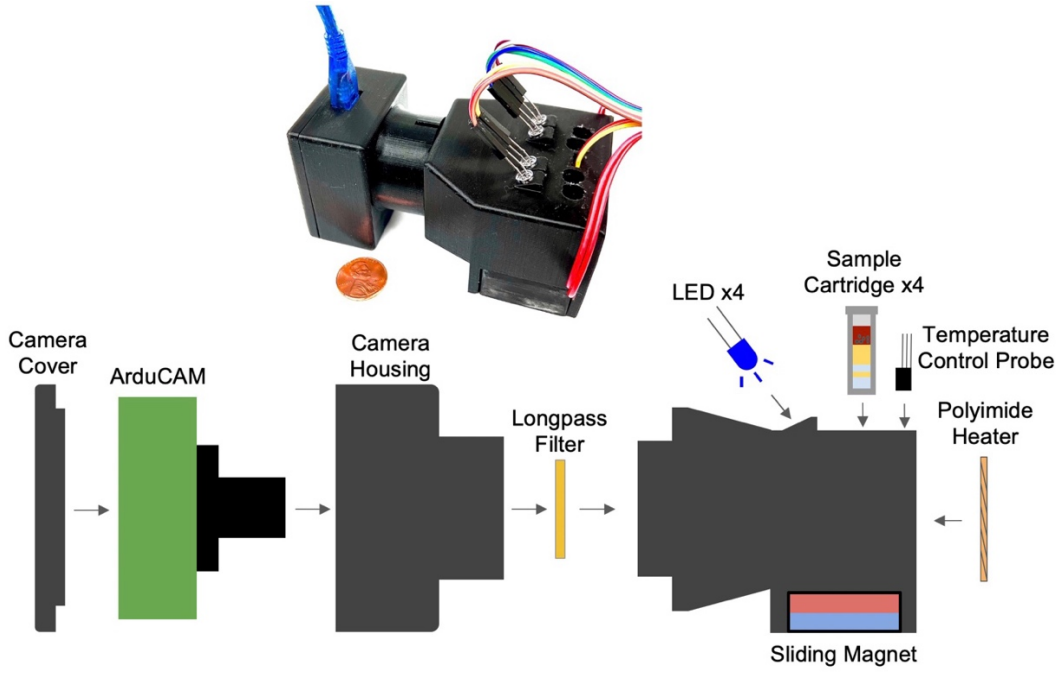

Figure 18. Photo and schematic of prototype device hardware. The photo includes a penny for scale. This device is capable of testing four samples at one time.

4.3.4 TRAP Demonstration

To show the capabilities of the two-TRAP assay displayed in Figure 17, the following experiment was conducted. Aliquots of eicosane and hexacosane were melted on a hot plate set to 180 °C. 15 µL of a yellow dyed solution containing 0.1% Tween 20 in water (a similar surfactant concentration to that of the LAMP master mix used in this work) was loaded into the bottom of a channel. 8 µL of hexacosane was loaded on top of the yellow solution to seal it in place. 10 µL of blue dyed water was loaded on top of the hardened hexacosane. 35 µL of eicosane was placed on top of the blue solution to seal it in place. Finally, 25 µL of a red dyed solution containing 100 µg of streptavidin magnetic beads was loaded on top of the hardened eicosane. The assembled cassette was then placed onto a magnet with a polyimide heater attached. The heater increased the temperature of the magnet and cassette to about 65 °C while a video of the resulting behavior was recorded. To quantify mixing, the red color value of the bottom layer of the cassette was extracted.

4.3.5 Virus Particle Lysis

In our proposed assay, which captures and isolates virus particles from complex samples, it is necessary to lyse the virus particles to release the virus genome for amplification and detection. In this work, we use thermolabile Proteinase K (NEB) to lyse virus particles. To determine how effective Proteinase K is at lysing virus particles, first a pure (free of extra-viral RNA) virus particle solution must be made. This was done by incubating a 50 µL solution including PBS and 10000 copies/µL gamma-irradiated SARS-CoV-2 (BEI Resources) with 1 µL (20 µg) Monarch RNase A (NEB) for 5 minutes at 56 °C. 1.6 µL (64 units) of RNase Inhibitor (Murine, NEB) was added

to the solution after the incubation. Six of these extra-viral RNA-free SARS-CoV-2 solutions were made. In three of them, 2.5 μL (0.3 units) thermolabile Proteinase K was added. These three solutions incubated at 37 °C for 15 minutes to allow Proteinase K to digest proteins. Then the solutions incubated at 55 °C for 10 minutes to inactivate the Proteinase K. To prepare the RT-LAMP detection reaction, nine 20 μL solutions were created as described above in the RT-LAMP Reaction subsection. 5 μL of each solution that underwent Proteinase K incubations as well as each solution that did not was added to LAMP reagents to create six separate LAMP reactions. Three more reactions were prepared with 5 μL of PBS used as a negative control. Each solution then incubated at 65 °C for 60 minutes, with fluorescence measurements taken every 30 seconds in the MiniOpticon.

4.3.6 Virus Viability Across a Melted TRAP

In order for our proposed assay to work properly, captured virus particles must remain intact and attached to magnetic beads while subjected to the increased temperature of a melted TRAP. To determine whether viruses remain viable after crossing a TRAP, the following experiment was conducted. First, 900 μg of streptavidin magnetic microbeads were rinsed with wash buffer then incubated with 225 pmol biotinylated capture aptamers in 18 μL of PBS for 60 minutes. Following the incubation, 12 μL of the mixture was added to a 178 μL solution containing PBS and 10000 copies/μL gamma-irradiated SARS-CoV-2. Simultaneously, the remaining 6 μL of the aptamer-bead mixture was added to 84 μL PBS (to act as the no-target control). Both mixtures incubated for 15 minutes. Eicosane was melted on a hot plate set to 180 °C. Six cassettes were loaded initially with 30 μL of the aptamer-bead-virus mixture, while

three cassettes were loaded with 30 µL of the no-target control mixture. 40 µL of melted eicosane was added to the three cassettes loaded with the no-target control and to three of the cassettes that were loaded with the aptamer-bead-virus mixture to form TRAPs. To the three cassettes that remained, mineral oil was used in place of eicosane. 50 µL of water was then added to each cassette, with a careful deposition on top of the oil to ensure no mixing occurred between the layers. The six cassettes containing TRAPs were placed horizontally on a hot plate set to 65 °C for 5 minutes to melt the TRAPs. Once melted, a neodymium magnet was used to transfer the beads across each melted TRAP, as well as across the oil partition in the cassettes (not on the hot plate). After bead transfer, the cassettes with TRAPs were removed from the hot plate to allow eicosane to harden. Once the eicosane hardened, 40 µL of the mixture on top of each TRAP and oil partition (now containing the magnetic beads) was pipetted out and into separate tubes each containing 1 µL of thermolabile Proteinase K. The nine tubes incubated at 37 °C for 15 minutes to allow Proteinase K to break down proteins in any virus particle that made it across the TRAP or oil partition. Then a 10-minute incubation at 55 °C inactivated the Proteinase K. An RT-LAMP detection reaction was prepared in the meantime: nine 20 µL solutions were created as described above in the RT-LAMP Reaction subsection. 5 µL of the supernatant of each mixture that underwent Proteinase K incubations (obtained by moving the beads out of the way of a pipette via a magnet) was transferred to each 20 µL LAMP solution. Each solution was then incubated at 65 °C for 60 minutes while fluorescence data was recorded in the MiniOpticon.

4.3.7 Sample-to-Answer SARS-CoV-2 Blood Test

To demonstrate that our sample-to-answer system can detect viruses in blood, the following experiment was conducted. 100 pmol biotinylated capture aptamers were attached to 400 μg streptavidin magnetic beads via a 15-minute incubation in 8 μL of PBS. A LAMP solution and a lysis solution were prepared by combining and mixing the following reagents. 1) LAMP solution: 50 μL WarmStart® Multi-Purpose LAMP/RT-LAMP 2X Master Mix with UDG (NEB), 2 μL 50X LAMP Fluorescent Dye (NEB), and 8 μL water. 2) Lysis solution: 4 μL (~0.5 units) Thermolabile Proteinase K, 10 μL LAMP primer mix containing 16 μM FIP/BIP, 2 μM F3/B3, and 4 μM LoopF/B for the N15 gene, 2 μL (2 units) Antarctic Thermolabile UDG, and 24 μL water. 15 μL of the LAMP solution was added to the bottom of four acrylic cassettes, followed by an 8 μL hexacosane seal, then 10 μL of the lysis solution was added after the hexacosane hardened, then 38 μL eicosane, then 2 μL of the bead mixture after the eicosane hardened. 20 μL of whole blood (obtained via finger prick) with 7 μg sodium polyanethole sulfonate (to prevent blood from coagulating around the magnetic beads), spiked with 5 μL of varying amounts of gamma-irradiated SARS-CoV-2 in PBS was added to each cassette. The cassettes were capped, then inserted into our portable fluorescence reader to commence the assay reactions.

The cassettes are subjected to 45 °C for 6 minutes to melt the first TRAP (made of eicosane); after it melts, the beads are pulled through the eicosane by a magnet at the bottom of the cassettes. After 5 minutes, the magnet positioned below the cassettes is moved away to remove the beads from its influence. At this point, the magnetic bead complexes are in the lysis solution, isolated from the blood sample (Figure 17). The

heating element within the fluorescence reader is shut off for 6 minutes to allow Proteinase K to degrade any virus envelope proteins, compromising the stability of virus shells and releasing viral genome from virus particles present in the mixture. The heating element is turned on again to deactivate the Proteinase K, melt the second TRAP (made of hexacosane) to combine LAMP reagents, and initiate the LAMP reaction. The space within the device stabilizes to 65 °C after about 15 minutes. This temperature is held until 60 minutes have passed since the insertion of the cassettes. Fluorescence measurements are recorded as normalized grayscale pixel values collected by the ArduCAM. These measurements begin 23 minutes into the test as that is the point in which the hexacosane TRAP melts, initiating the LAMP reaction.

4.3.8 SARS-CoV-2 Patient Plasma Test

Plasma samples (deidentified) from COVID-19 patients were obtained from the University of Maryland Medical Center. Samples were acquired from hospitalized COVID-19 patients between the dates 2020-09-18 and 2022-02-15 under approved IRB protocols. Each sample was tested by the MiniOpticon benchtop RT-qPCR system. Using the QIAamp Viral RNA Kit (Qiagen), 140 µL of each plasma sample was filtered into 60 µL of elution buffer containing extracted virus genomes that may have been present in the plasma sample. 5 µL of the resulting solution was added to a 1-step RT-qPCR master mix (Promega). Each solution underwent a 15-minute reverse transcription step at 45 °C for 15 minutes, followed by two minutes in a 95 °C initial denaturation step, then 45 PCR cycles with each cycle being 95 °C for 3 seconds, and 55 °C for 30 seconds. The threshold cycle in this work is defined as the first PCR cycle that resulted in a fluorescence measurement higher than 0.011 AU. To estimate the

number of copies in each solution, dilutions of SARS-CoV-2 (BEI) were subjected to the same sample treatment and qPCR reaction, and a standard curve was created (Electronic Supporting Information). Cycle thresholds from tested patient samples were compared to the standard curve. Plasma samples were also tested with our sample-to-answer diagnostic. The experimental setup above in the Sample-to-Answer SARS-CoV-2 Blood Test subsection was repeated but instead of adding 20 μL of whole blood spiked with 5 μL of SARS-CoV-2, 25 μL of plasma from COVID-19 patients was loaded into the cassettes.

4.4 Results & Discussion

4.4.1 TRAP Operation

Our previous work has shown that by melting a removable TRAP, we can control when pre-partitioned reagents mix, simply by adjusting temperature.[72] We have also shown stationary TRAPs that enable a sample-to-answer immunoassay.[88] In this work, which presents an assay capable of detecting virus genomes from complex samples, both forms of TRAPs are utilized. A stationary TRAP is required so that, when melted, it will prevent the sample (e.g. whole blood) from interfering with detection chemistry while still allowing virus particles captured onto magnetic beads to transition to the lysis reagent. Meanwhile, a removable TRAP enables the sequential steps of virus lysis and RT-LAMP. The RT-LAMP reagents must be sequestered during proteolytic lysis (to avoid degradation of the polymerase) and then added following the heat-kill of the protease. Thermolabile Proteinase K is inactivated at a temperature lower than the melting temperature of the removable TRAP, and thus when increasing the temperature

to release the TRAP and combine the reagents, the Proteinase K is inactivated. Once the removable TRAP is melted, the nucleic acid amplification reaction (RT-LAMP) commences.

Figure 19A illustrates the process described above using dyes so that it is observable. The red solution (representing the blood sample in the assay) remains separated from the blue solution (representing the lysis reagent layer) while the beads traverse the stationary TRAP. As the temperature increases to melt the removable TRAP, the blue solution and the yellow solution (representing RT-LAMP reagents) quickly mix. The sharp slope in Figure 19B indicates a quick mixing upon melting the removable TRAP. A full video of the setup displayed in Figure 19 can be found in the Electronic Supporting Information. This demonstrates that the combination of the two types of TRAPs in a single cassette can maintain partitioning of the blood sample away from the assay while sequentially enabling the assay steps, including the precise addition of reagents and rapid mixing.

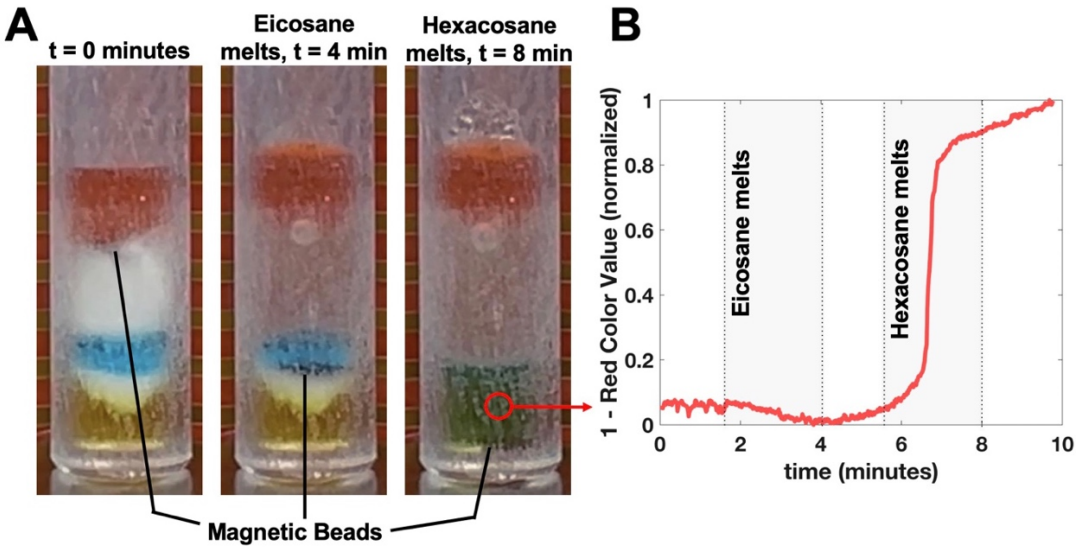

Figure 19. (A) Photos depicting each stage of the assay within a cassette with dyes in each solution. Magnetic beads traverse the eicosane stationary TRAP without red dye leaking through. When the hexacosane removable TRAP melts, the layers on either side quickly mix. (B) Data representing the speed at which two liquids mix upon melting a removable TRAP.

4.4.2 Thermolabile Proteinase K Enables RNA Release from Virus and is Compatible with Sample-to-Answer LAMP

It has been shown that Proteinase K can act as a viral lysis reagent and streamline sample preparation before RT-qPCR.[91] It works by breaking down proteins which are abundant in the envelope of many viruses. Here we utilize a thermolabile Proteinase K that is heat-inactivated below the operation temperature of LAMP. Notably, it is active at a temperature above the melt temperature of the stationary TRAP and below the temperature of the removable TRAP. Figure 20 demonstrates the effectiveness of Proteinase K at lysing the SARS-CoV-2 virus. The data compares the LAMP-based amplification of the SARS-CoV-2 genomes for three aliquots of virus treated with Proteinase K to three samples that were not treated. Note that no subsequent purification steps are performed after lysis; the sample is heated to inactivate the

Proteinase K and then directly added to LAMP master mix. As Figure 20 shows, the sample treated with Proteinase K amplified quickly, while the untreated sample is essentially not detected.

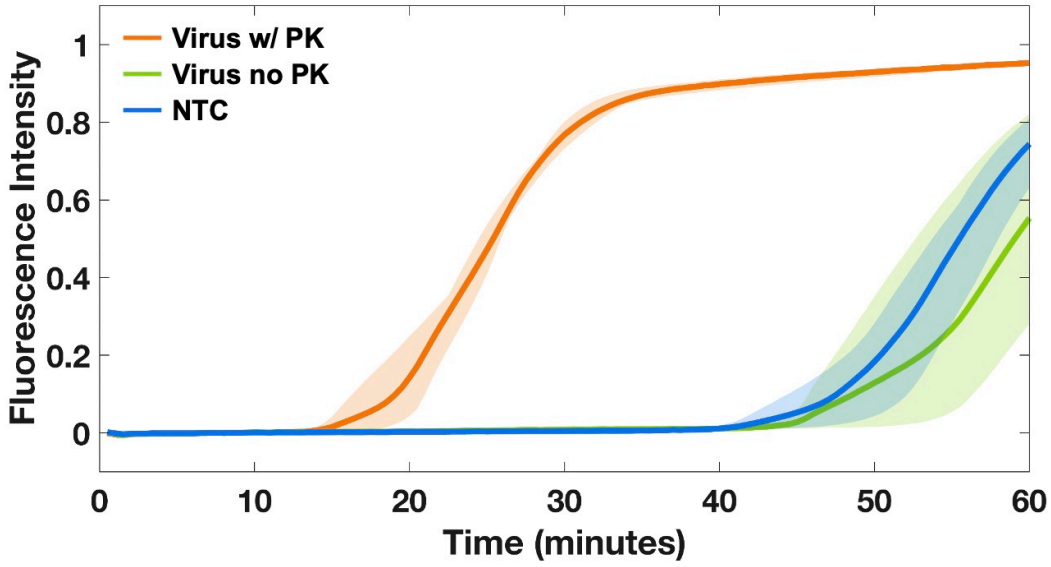

Figure 20. LAMP results from a sample of virus particles after an incubation with Proteinase K (orange curve) compared to a sample of virus particles without a Proteinase K incubation (green curve), along with a no-target control (blue curve).

4.4.3 Aptamer-Beads Pull Virus Through a Melted TRAP

In previous work, we demonstrated that antibody-antigen complexes attached onto magnetic bead traversed melted stationary TRAPs without releasing.[88] Here, however, the cargo is virus particles which are captured via aptamers instead of antibodies. Therefore, it was necessary to investigate whether our bead-aptamer-virus complex remains viable after traversing a melted TRAP. We compared the amplification of virus that traversed a melted eicosane TRAP on aptamer-functionalized magnetic beads with the amplification of virus that was similarly pulled through a mineral oil partition at

room temperature. LAMP data from both experiments is presented in Figure 21. The timing of the amplification signal for the two cases is not statistically significantly different. We conclude that the elevated temperature of the TRAP results in minimal or no virus loss while beads are traversing a melted TRAP.

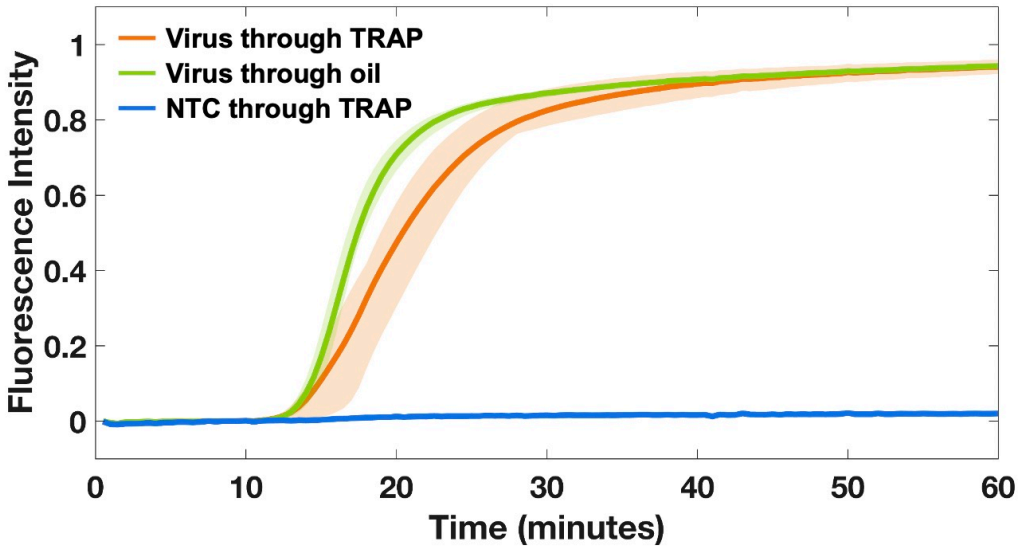

Figure 21. LAMP results from a sample of virus particles after capture onto magnetic beads and transfer across a melted eicosane TRAP (orange curve) compared to transfer across an oil partition at room temperature (green curve), along with a no-target control (blue curve).

4.4.4 Sample-to-Answer Detection of SARS-CoV-2 in Blood

To demonstrate the capability of our sample-to-answer system to detect viruses in whole blood, we spiked whole blood (drawn from finger pricks) with specific concentrations of SARS-CoV-2 virus and tested it in our dual-TRAP cassette. Specifically, 20 µL of whole blood was spiked with 5 µL of PBS containing 5000, 500, 50, 5, or 0 copies of SARS-CoV-2 (according to the stock concentration reported by BEI). Figure 22A shows the average amplification curves for three samples with 5000 copies (orange curve) and three blank samples (blue curve). The curves show rapid

amplification for the positive sample with minimal variation in the time to positive (TTP); additionally, the curves show a significant amount of time between the TTP of the positive and negative samples.

Figure 22B reports the results of 35 different blood sample tests, seven for each concentration of spiked SARS-CoV-2. If a blood sample resulted in a TTP of 22 minutes or less after the initiation of the LAMP reaction, the sample was deemed positive. The samples that had a TTP of greater than 22 minutes or never amplified for the duration of the test were deemed negative. Samples containing at least 500 copies of SARS-CoV-2 resulted in 100% accuracy. One false negative was reported for the seven samples with 50 copies, and two false negatives were reported for the seven samples with 5 copies. Thus, without any sample preprocessing, highly sensitive detection of virus directly from a whole blood sample is made possible by our diagnostic system. This capability to detect virus directly from whole blood has potential to significantly improve the viremia diagnostic pathway, drastically decreasing time to diagnosis.

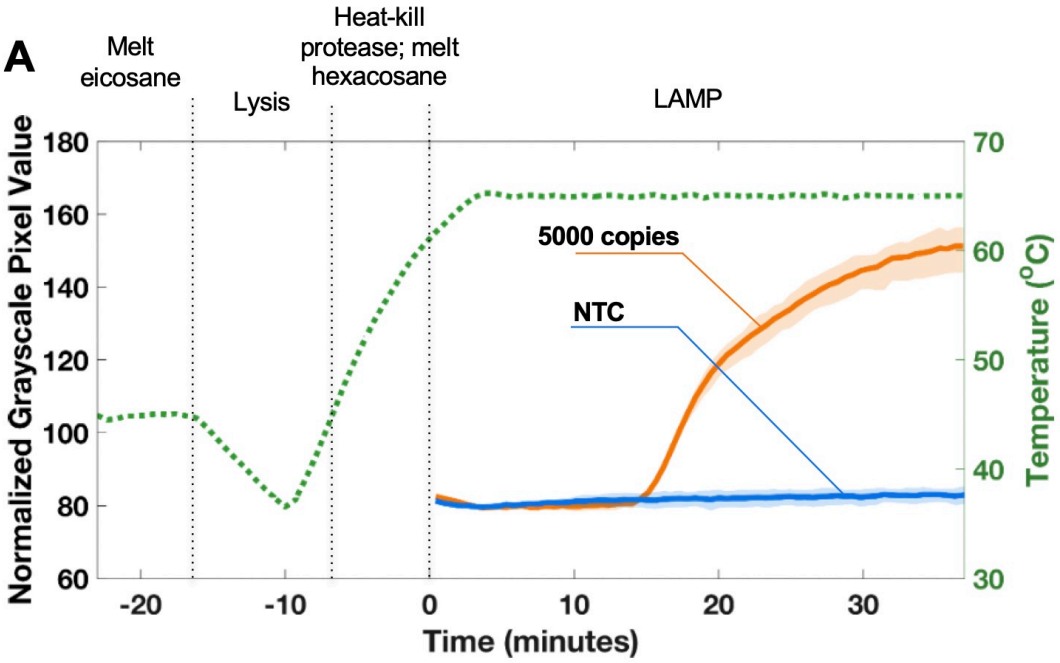

B

SARS-CoV-2 sample	Test (*N*=7)
5000 copies	+ + + + + + +
500 copies	+ + + + + + +
50 copies	+ + + + + + -
5 copies	+ + + + + - -
0 copies	- - - - - - -

Figure 22. (A) Fluorescence data from our portable reader device plotted on an annotated graph that includes the temperature profile inside the device (dotted line). (B) Compiled results from 35 blood tests using our device.

4.4.5 Detection of SARS-CoV-2 in COVID-19 Patient Plasma Samples

To further validate the capability of our system to detect viremia, we used our dual-TRAP cassette and handheld device to test plasma samples from patients with severe

COVID-19 disease. The samples were first tested by conventional RT-qPCR; samples with a cycle threshold of less than 35 were determined to be positive for viremia. Three samples tested positive, while six were negative. The correlation between our sample-to-answer system and conventional RT-qPCR is presented in Figure 23. All three of the patient samples that were determined to be positive by RT-qPCR were also reported as positive for the virus by our device; each LAMP reaction had a TTP within 16 minutes of reaction initiation (i.e. when the hexacosane TRAP melted). All of the LAMP signals in our device that resulted from testing SARS-CoV-2-negative plasma samples occurred at later time points compared to the positive samples, with many not appearing until after 30 minutes into the LAMP reaction. Two trials of the negative samples, however, resulted in a LAMP signal close to the positive samples.

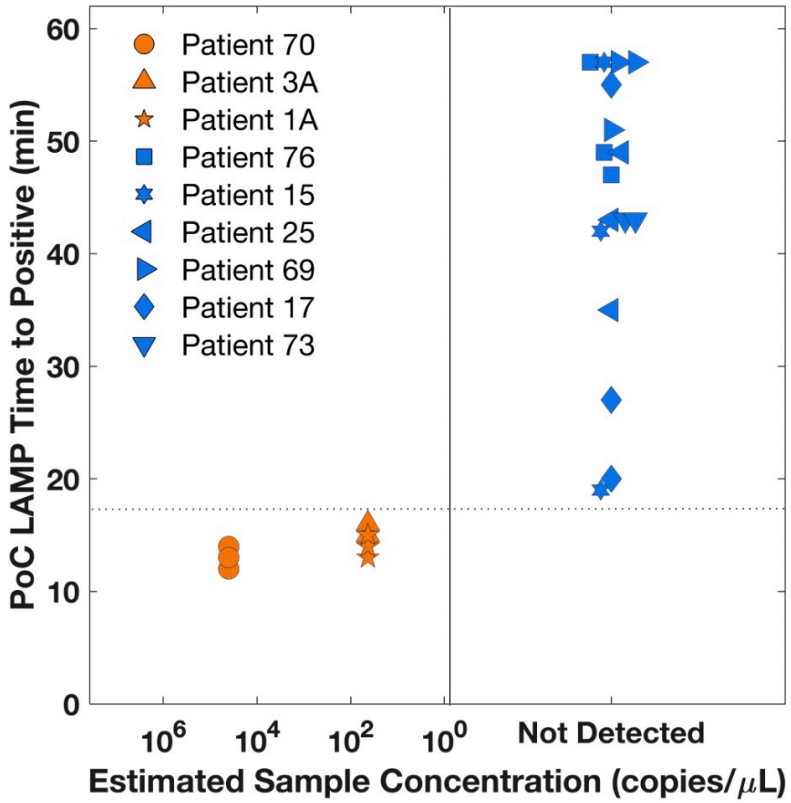

Figure 23. COVID-19 patient plasma samples tested via RT-qPCR (x-axis) and via our sample-to-answer device (y-axis). Samples confirmed positive by RT-qPCR are colored orange while those not detected by RT-qPCR are colored blue.

4.5 Conclusions

In this work, we have demonstrated the sample-to-answer detection of SARS-CoV-2 virus in blood samples. Our system positively identified the virus in 100% of blood samples spiked with 500 copies/sample and greater than 70% of blood samples spiked with 5 copies/sample. In addition, our system showed good agreement with conventional RT-qPCR in detecting SARS-CoV-2 viremia in banked samples from patients with severe COVID-19 disease. Notably, our sample-to-answer system utilizes an easy-to-manufacture cassette and an automated portable device that does not require

microfluidics, a pump, or precise sample handling steps. Future work will reduce the footprint of the portable device and will include a motorized arm to slide the magnet in and out of position under the cassette. Additionally, we can broaden the application of our system simply by changing the aptamer sequence and the primer sequences. We aim to detect other life-threatening diseases, such as Hepatitis C and HIV.

Chapter 5: Saliva-STAT: a Sample-to-Answer Saliva Test for COVID-19

Reprinted from a submitted manuscript: "Saliva-STAT: Sample-to-Answer Saliva Test for COVID-19" by D. Boegner, J. Rzasa, E. Benke, and I. White. Submitted 2024

5.1 Overview

Highly accessible and highly accurate diagnostics are necessary to combat rapidly-spreading infectious diseases, such as the recent COVID-19 pandemic. While lateral flow antigen tests have become pervasive, they are insufficiently sensitive to detect early or asymptomatic disease. Nucleic acid amplification tests provide the needed sensitivity, but accessibility of these tests continues to be a challenge due to the need for precise sample processing steps. Here we report a sample-to-answer test for saliva samples (***S***aliva-STAT) that utilizes a battery-powered handheld instrument and a low-cost easily-manufacturable sample cassette to perform a nucleic acid amplification test for viral pathogens. To enable a completely automated assay, we leverage thermally responsive alkane partitions (TRAPs) and paramagnetic beads for virus purification and concentration, as well as reagent addition and mixing. Notably, the saliva STAT easily accommodates directly-dispensed saliva samples (in contrast to microfluidic devices), which is necessary for self-testing. Using the ***S***aliva-STAT platform, we demonstrate detection of down to 0.2 copies/μL of SARS-CoV-2 virus in saliva samples. We envision that the ***S***aliva-STAT could be used in walk-in clinics, mobile clinics, public testing locations, and in the home. With minor adjustments to the assay, the ***S***aliva-STAT platform can easily be adapted for other respiratory viruses, such as Influenza.

5.2 Introduction

The COVID-19 pandemic has had a tremendous global impact, including millions of deaths,[58] tens of millions of long-COVID cases,[92] trillions of dollars in economic losses,[93] growing inequality,[94,95] prolonged disruption of student learning,[96] and many others. One of the primary tools to inhibit the spread of a pandemic is the utilization of widely available testing.[97] Soon after the start of the COVID-19, pandemic, RT-qPCR tests were quickly developed and approved for use. However, the impact of the tests was less than expected because they were confined to central laboratories, leading to delayed results and inaccessibility in many regions around the world. Several months later, lateral flow antigen tests were developed and approved. These tests gave a broader population the capability to test at home and quarantine immediately following the test when necessary. However, these tests are not as sensitive as genomic tests. Moreover, the tests take several months to develop and approve because of the need to create antibodies against the viral antigens. To be prepared to combat future pandemics, the world needs low-cost, easy-to-use tests that can be developed at the start of the pandemic and that have the sensitivity to identify the infection in the early stages while contagion is high but symptoms are low.

The majority of COVID-19 tests to date have utilized nasopharyngeal swabs as the sample medium. In healthcare settings, the use of swabs exposes healthcare workers; meanwhile, the swabs are less reliable for self-testing. Saliva may offer a better alternative for a sample medium. It is less invasive than swabs, it is compatible with self-testing, and it is less vulnerable to supply-chain shortages.[91,98,99] Several trials confirmed saliva as an effective sample medium for COVID-19 testing.[91,100–104] In

addition, saliva may have an advantage over swabs, as swab-based genomic tests are known to remain positive for weeks after the infection is resolved, while saliva may be a more accurate representation of the active infection.[98]

Despite the ease of sample collection, genomic tests with saliva samples have been limited to central labs. Detection of the viral RNA requires viral lysis, RNA extraction and purification, reverse transcription, and DNA amplification. Moreover, while saliva has several advantages noted above, it also comes with challenges. The sample volume is much larger than the RT-qPCR reaction, preventing it from being directly coupled with the amplification step. In addition, the sample volume cannot be well controlled. Finally, saliva has variable viscosity and mucus content. In one report, Landry et al. noted that one third of the samples utilized in their study were "thick, stringy, and difficult to pipet."[101] A saliva self-test must be low in cost, extremely easy to use, compatible with large and varying sample volumes, and tolerant of a range of sample viscosity and mucus content.

Preferably, the test would be sample-to-answer; i.e., the saliva sample is collected in a tube or cassette, and then the patient receives the answer from a device (or attached smartphone/tablet) a short time later. Significant progress has been made toward the development of point-of-care diagnostic technologies,[44,50,78,82,84,86,105,106] but to date there are very few reports of portable, low-cost, sample-to-answer technology for saliva samples. Notably, Tang et al. demonstrated detection of SARS-CoV-2 in saliva using a sample-to-answer system with reagents integrated into a microfluidic chip, driven by a pump.[81] While this system represents a significant advancement, there remains potential for simplification.

We recently developed a sample-to-answer diagnostic platform that utilizes a low-cost easily manufacturable cassette and a simple portable device to analyze complex samples. The key enabling technology is thermally responsive alkane partitions (TRAPs), which enable automated addition and mixing of reagents, as well as reagent transfer steps.[72,74,87,88] TRAPs, which are formed from purified higher order alkanes, are initially solid at ambient temperature and partition reagents integrated into the cassette. When warmed above the melt temperature, (i) thinner TRAPs breach, enabling the automated addition and mixing of the two surrounding reagents, while (ii) thicker TRAPs continue to partition the surrounding aqueous reagents, but allow molecularly functionalized paramagnetic beads to be pulled through from one reagent to another. The TRAPs do not require microfluidic confinement to partition reagents and they are sufficiently robust to survive severe mechanical agitation.[87] Moreover, because the sample remains partitioned from the assay by the TRAPs, the assay is independent of the sample complexity, including the viscosity of the sample and reaction inhibitors present in the sample.

In this work, we demonstrate sample-to-answer detection of viruses in large-volume saliva samples. The sample cassette and the assay are diagrammed in Figure 24. The assay cassette is designed to accept a saliva sample directly from the user. As it is impossible for a user to precisely dispense sub-100 μL volumes of sample, the cassette must accept larger volumes, and the assay must be tolerant to variations in sample volume. After the sample is deposited in the cassette, aptamer-modified paramagnetic beads capture virus from the sample. Upon warming the cassette, the beads are pulled through a stationary TRAP into a protease-based lysis solution by a

magnet positioned below the cassette. Following lysis, the cassette is further warmed to inactivate the protease and to melt a second TRAP, which releases reagents for loop mediated isothermal amplification (LAMP). The assay is controlled and analyzed by a handheld battery-powered instrument that provides temperature control, manipulates a magnet, and measures fluorescence. Using this sample-to-answer test for saliva samples (Saliva-STAT), we demonstrate sensitive and specific detection of SARS-CoV-2 virus in saliva down to 0.2 copies/µL in sample volumes as high as 500 µL.

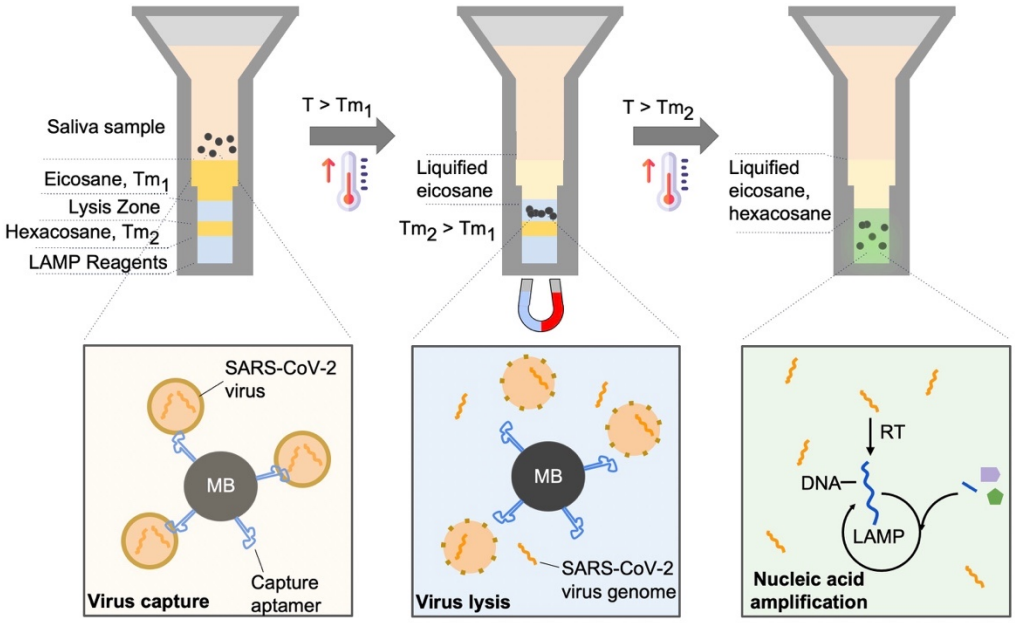

Figure 24. Schematic of the Saliva-STAT diagnostic test for the SARS-CoV-2 virus. After a saliva sample is deposited into the funnel attached to a cassette, magnetic microbeads functionalized with aptamers capture virus particles present in the sample. The temperature is increased to melt the eicosane layer, allowing a magnet to pull beads through, isolating virus particles from the saliva sample. Once through, the virus particles are lysed. After lysis, the hexacosane layer is melted, initiating the LAMP reaction.

5.3 Materials & Methods

5.3.1 Materials

The alkanes in this work include n-eicosane (melting point ~37 °C), 99%, and n-hexacosane (melting point ~57 °C), 99%, both from ThermoFisher Scientific. Pierce Streptavidin Magnetic Beads (1.05 μm diameter) were purchased from ThermoFisher Scientific. Antarctic Thermolabile Uracil DNA Glycosylase (UDG) was purchased from NEB and is used throughout this work paired with DNA amplification reactions that result in nucleic acid products containing uracil bases. UDG helps to reduce the risk of carry-over contamination from previous DNA amplification reactions. WarmStart® Multi-Purpose LAMP/RT-LAMP Master Mix with UDG, LAMP Fluorescent Dye, and thermolabile Proteinase K were purchased from NEB. Gamma-irradiated SARS-CoV-2 was supplied as a ~109 copies/mL stock solution from BEI Resources. The biotinylated SARS-CoV-2 RBD aptamer[89] used in this work as well as LAMP primers for the N15 gene[90] were purchased from IDT and their sequences can be found below.

Biotinylated CoV2-RBD-4C aptamer

5'–ATCCAGAGTGACGCAGCATTTCATCGGGTCCAAAAGGGGCTGCTCGGG
ATTGCGGATATGGACACGTTTTTTTT /3Bio/ – 3'

LAMP Primers (N15 gene)

FIP 5’ – TGCTCCCTTCTGCGTAGAAGCCAATGCTGCAATCGTGCTAC – 3’
BIP 5’ – GGCGGCAGTCAAGCCTCTTCCCTACTGCTGCCTGGAGTT – 3’
F3 5’ – AGATCACATTGGCACCCG – 3’
B3 5’ – CCATTGCCAGCCATTCTAGC – 3’
LF 5’ – GCAATGTTGTTCCTTGAGGAAGTT – 3’
LB 5’ – GTTCCTCATCACGTAGTCGCAACA – 3’

5.3.2 Saliva-STAT Instrument

We designed and fabricated a battery-powered handheld instrument to control the assay and to measure fluorescence from the LAMP reaction. An exploded view of the instrument is shown in Figure 25A. A photo of the instrument and the assay cassette is shown in Figure 25B. The 3D-printed case has dimensions of 9.4 x 9.4 x 4 cm^3. The instrument is composed of three subsystems: (1) a custom PCB with microcontroller (ATMEGA328P, Atmel), USB converter, heater controller, photodetector (FDS100, Thorlabs) and transimpedance amplifier, LED (470 nm), and analog-digital converter (AD4116, Analog Devices); (2) a custom-milled aluminum chamber that surrounds the cassette under test and holds a Peltier heater (NL1023T-01AC, Marlow Industries), digital temperature probe (DS18B20, Maxim Integrated), and optical bandpass filter (521nm center wavelength, 20nm full-width at half max, #26-717, Edmund Optics); and (3) a neodymium cylinder magnet 12.7 mm tall and 25.4 mm in diameter (DX08, K&J Magnetics) attached to a servo motor (SG92R, Adafruit) that automatically positions the magnet below or away from the assay cassette. Three indicator LEDs are also included on the PCB to indicate the instrument and assay status. The instrument is powered by a lithium polymer battery (ICR18650, Pkcell). An onboard charge controller (MCP73871, Microchip Inc.) and a boost converter (TPS61090, Texas Instruments) manage charging and power distribution to the rest of the system.

To aid with prototyping, a custom graphical user interface (GUI) was created in C# to operate the instrument and to display the temperature and fluorescence in real time. The assay can be initiated through the GUI or by pressing the “start” button on the instrument. The GUI connects to the microcontroller through USB. The

microcontroller is programmed using the Arduino IDE programming software. The microcontroller utilizes a pulse-width modulation PID feedback loop to dynamically control the temperature of the assay cassette utilizing the Peltier heater and the temperature probe. The microcontroller cycles the temperature through the stages indicated in Figure 24. For prototyping purposes, the stage timing and temperature can be controlled via the GUI. Additionally, the microcontroller turns on the excitation LED and collects the fluorescence emission readings from the analog-digital controller for the duration of the assay. Fluorescence values are sent through USB to the GUI for real time display. The microcontroller is also programmed to reposition the magnet using the servo motor. Initially the magnet is located below the assay cassette. After the paramagnetic beads are pulled through the first TRAP, the microcontroller actuates the servo motor to move the magnet away from the assay cassette.

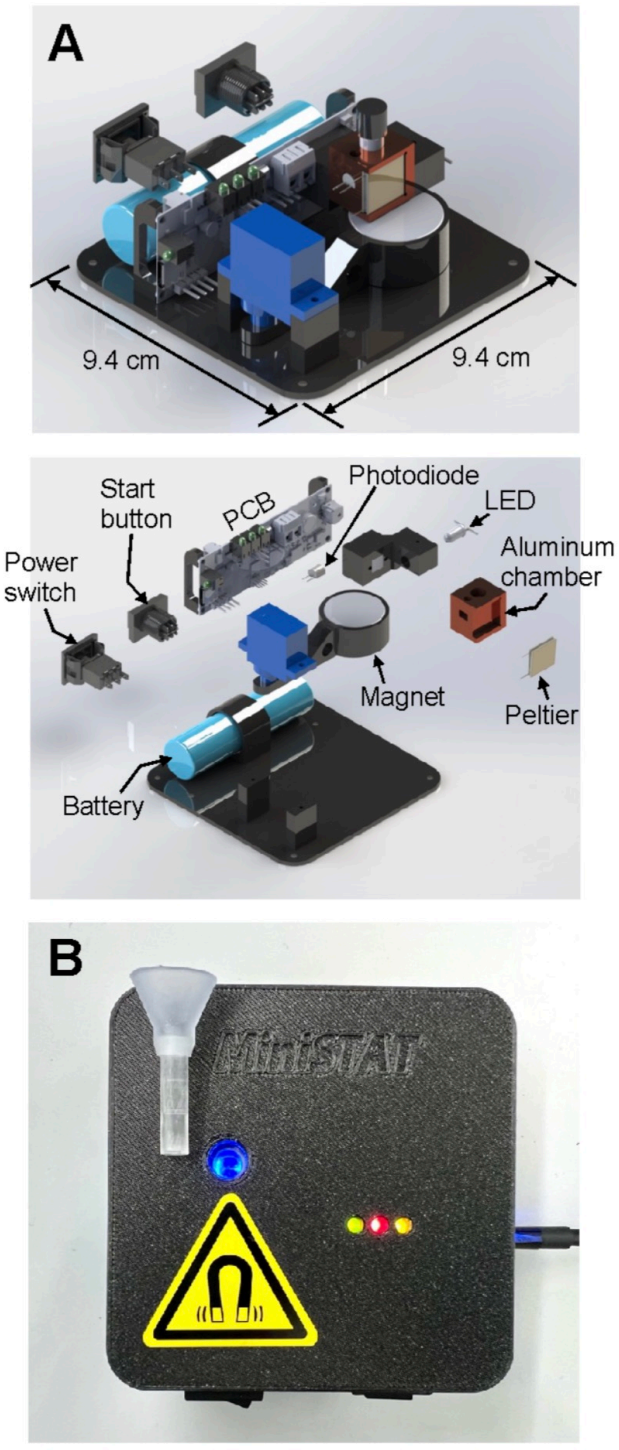

Figure 25. (A) Rendering of the assembled Saliva-STAT handheld instrument and exploded view. (B) Photo of the instrument with a sample cassette.

5.3.3 Assay Cassettes

Two types of cassettes were fabricated, the first by cutting via CNC an acrylic sheet with 24 mm thickness (McMaster-Carr) into 6.35 mm diameter cylinders, each with a channel 3.2 mm in diameter and 23 mm deep. The second type was fabricated by a similar method except the upper 14.5 mm of the channel was 4.6 mm in diameter. A funnel attachment was 3D printed via SLA using 3DM-Tough clear resin and the SL1S printer from Prusa. This funnel piece fits onto the opening of the larger volume cassette to allow for up to 500 μL of sample in the assay.

5.3.4 Paramagnetic Bead Manipulation in the Saliva-STAT Cassette

To quantify how well the magnet can gather beads to the alkane-saliva interface from a 500 μL sample of saliva, the following experiment was conducted. 25 μL of water was placed at the bottom of a larger volume cassette. 40 μL of eicosane was deposited on top of the water. Then, with the funnel attachment on the cassette, 500 μL of saliva with 100 μg paramagnetic beads was placed into the cassette on top of the eicosane layer. The cassette was placed onto a magnet and a video was recorded. The red color value of an area near the top of the funnel was extracted to show the movement of beads out of the saliva sample volume and toward the magnet.

5.3.5 Automatic Reagent Addition & Mixing in the Saliva-STAT

To demonstrate automatic reagent addition and rapid mixing, we partitioned a DNA solution and an intercalating dye solution by a thin TRAP in a cassette and then recorded the fluorescence as the temperature was increased. First, the bottom of a channel was loaded with 15 μL of DNA (a product of a previously run LAMP reaction,

so the precise concentration of DNA is unknown). 8 µL of melted hexacosane was then placed on top of the DNA solution, where it solidified into a thin TRAP. Then, 10 µL 5X NEB LAMP Fluorescent Dye was loaded on top of the hardened hexacosane. To prevent evaporation, 40 µL eicosane was deposited on top to seal the solutions. The assembled cassette was then placed into the **S**aliva-STAT instrument and fluorescence measurements were recorded as it heated up to 60 °C to melt the hexacosane.

5.3.6 LAMP in a Benchtop Thermocycler Using Saliva Samples

As a benchmark to compare with the CoV-STAT device, LAMP reactions were run in PCR tubes using a MiniOpticon thermocycler. Two setups were prepared. The first setup consisted of five LAMP reactions containing 5000, 500, 50, 5, and 0 copies of SARS-CoV-2 genome. Prior to the LAMP setup, 50 µL solutions of saliva spiked with the said amount of virus genomes were prepared. Each sample incubated with 2.5 µL of Proteinase K for 15 minutes at 37 °C, then 10 minutes at 55 °C to inactivate the Proteinase K. Based in part on the recommended LAMP protocol from the NEB website, the LAMP solution was prepared as follows: A solution containing 1X WarmStart® Multi-Purpose LAMP/RT-LAMP Master Mix with UDG (NEB), 1X LAMP Fluorescent Dye (NEB), and LAMP primers (1.6 µM FIP/BIP, 0.2 µM F3/B3, and 0.4 µM LoopF/B) for the N15 gene is created using nuclease-free water to reach the appropriate concentrations, with a volume of 100 µL. This solution was divided into five PCR tubes, each with 20 µL. 5 µL of each of the SARS-CoV-2 saliva sample solutions was added to each 20 µL solution. After vortexing, the tubes were then loaded into the MiniOpticon and incubated for 100 minutes at 65 °C.

The second setup follows a bead-based isolation protocol for the virus particles. First, 250 µg of streptavidin magnetic beads were rinsed then incubated with 100 pmol biotinylated CoV2-RBD-4C aptamers in 10 µL PBS for 15 minutes. Then, 2 µL aliquots of the mixture were distributed into five PCR tubes each containing saliva samples spiked with either 5000, 500, 50, 5, or 0 copies of SARS-CoV-2. The beads complexes were allowed to incubate with the virus samples for another 15 minutes. Following the incubation, a magnet was used to gather the beads to the side of the PCR tubes and three 80 µL PBS rinses were conducted to the beads. After the last rinse, 50 µL PBS was added to the beads, along with 2.5 µL Proteinase K. Each tube then incubated for 15 minutes at 37 °C, followed by 10 minutes at 55 °C. 5 µL of the supernatant from each tube was taken and added to separate 20 µL LAMP solutions prepared the same way as described above. After vortexing, the tubes were then loaded into the MiniOpticon and incubated for 100 minutes at 65 °C.

5.3.7 Saliva-STAT LAMP Capabilities

To demonstrate the capability of the Saliva-STAT instrument and cassette to rapidly amplify and detect genomic RNA, LAMP reactions with varying concentrations of SARS-CoV-2 genome were run within the **S**aliva-STAT instrument. First, 50 µL of 104 copies/µL SARS-CoV-2 virus was incubated with 2.5 µL (0.3 units) of Proteinase K in PBS for 15 minutes at 37 °C, then 10 minutes at 55 °C to inactivate the Proteinase K. This solution was then diluted with PBS into several solutions of decreasing concentrations. Based in part on the recommended LAMP protocol from NEB, the 20 µL LAMP solution was prepared in nuclease-free water as follows: 1X WarmStart® Multi-Purpose LAMP/RT-LAMP Master Mix with UDG (NEB), 1X LAMP

Fluorescent Dye (NEB), and LAMP primers (1.6 µM FIP/BIP, 0.2 µM F3/B3, and 0.4 µM LoopF/B) for the N15 gene. 5 µL of each of the lysed SARS-CoV-2 solutions was added to LAMP reaction solutions. After vortexing, each sample was loaded into a cassette. The cassette was then loaded into the **S**aliva-STAT instrument, which heated it at 65 °C for 60 minutes while recording the fluorescence of the solution. For the amplification curves, the time-to-positive (TTP) was calculated as the first timepoint for which the fluorescence value was 0.5% larger than the value one minute prior.

5.3.8 Detection of SARS-CoV-2 in Saliva Samples with the Saliva-STAT

To demonstrate virus detection in saliva samples using our sample-to-answer system, we tested SARS-CoV-2 spiked samples with small volume (25 µL) samples and larger volume (500 µL) samples. First, 200 µg streptavidin paramagnetic beads were incubated with 50 pmol biotinylated capture aptamers for 15 minutes in 4 µL of PBS. The LAMP reaction solution was prepared by combining 25 µL WarmStart® Multi-Purpose LAMP/RT-LAMP 2X Master Mix with UDG (NEB), 1 µL 50X LAMP Fluorescent Dye (NEB), and 4 µL water. Lysis solution was prepared by combining 2 µL (~0.25 units) Thermolabile Proteinase K, 5 µL LAMP primer mix containing 16 µM FIP/BIP, 2 µM F3/B3, and 4 µM LoopF/B for the N15 gene, 1 µL (1 unit) Antarctic Thermolabile UDG, and 12 µL water. 15 µL of the LAMP solution was added to the bottom of the acrylic cassette, followed by 8 µL melted hexacosane. Then 10 µL of the lysis solution was added after the hexacosane hardened, followed by 40 µL eicosane. 2 µL of the bead mixture was added after the eicosane hardened. 20 µL or 495 µL of saliva spiked with 5 µL of varying amounts of gamma-irradiated SARS-CoV-2 in PBS was added to each cassette. Concentrations of 200, 20, 2, 0.2, and 0 copies/µL in the

500 μL saliva samples as well as 2 and 0.2 copies/μL in the 25 μL saliva samples were prepared. The 500 μL samples were tested using the larger-volume assay cassette.

In the Saliva-STAT, the cassette is subjected to ~40 °C for 6 minutes to melt the first TRAP (eicosane); after it melts, the beads are automatically pulled through the eicosane by a magnet below the cassette. After 5.5 minutes, the magnet positioned below the cassette is automatically moved away via a rotating lever attached to a motor. At this point, the paramagnetic bead complexes are in the lysis solution, isolated from the saliva sample. The instrument then holds 37 °C for 6 minutes to allow Proteinase K to degrade any virus envelope proteins, compromising the stability of virus shells and releasing viral genome. The temperature then ramps up to 55 °C for 5 minutes to inactivate the Proteinase K. Finally, the temperature is increased to 65 °C to melt the second TRAP (hexacosane) to thus to add the LAMP reagents to the lysate and initiate the LAMP reaction. This temperature is held for 60 minutes. Fluorescence measurements are recorded via the photodiode in the Saliva-STAT.

5.4 Results & Discussion

5.4.1 Paramagnetic Bead Isolation in a Large-Volume Sample Cassette

In our previous work with stationary TRAPs, the magnet for pulling the beads through stationary TRAPs was located in close proximity to small-volume reagents containing the beads.[87,88] For a fully automated saliva assay, it is necessary for the magnet to remain at the bottom of the cassette, but to pull the beads from a large volume saliva sample at the top of the cassette. In our cassette, the distance between the magnet in the instrument and the top of the eicosane TRAP (beginning of the inserted saliva sample

layer) is about 10 mm, while the distance between the magnet and the top of the saliva sample layer (in the funnel attachment) is about 30 mm.

To quantify the speed with which the paramagnetic beads are pulled down in the cassette, we loaded a 500 μL sample containing paramagnetic beads into the assay cassette and placed the cassette on top of the magnet. We then recorded a video of the beads migrating to the eicosane interface. We quantified the red color value in a region of interest near the top of the cassette. The results are presented in Figure 26. The results demonstrate that after about three minutes, a sufficiently large majority of the beads are pulled from the sample to the sample-TRAP interface.

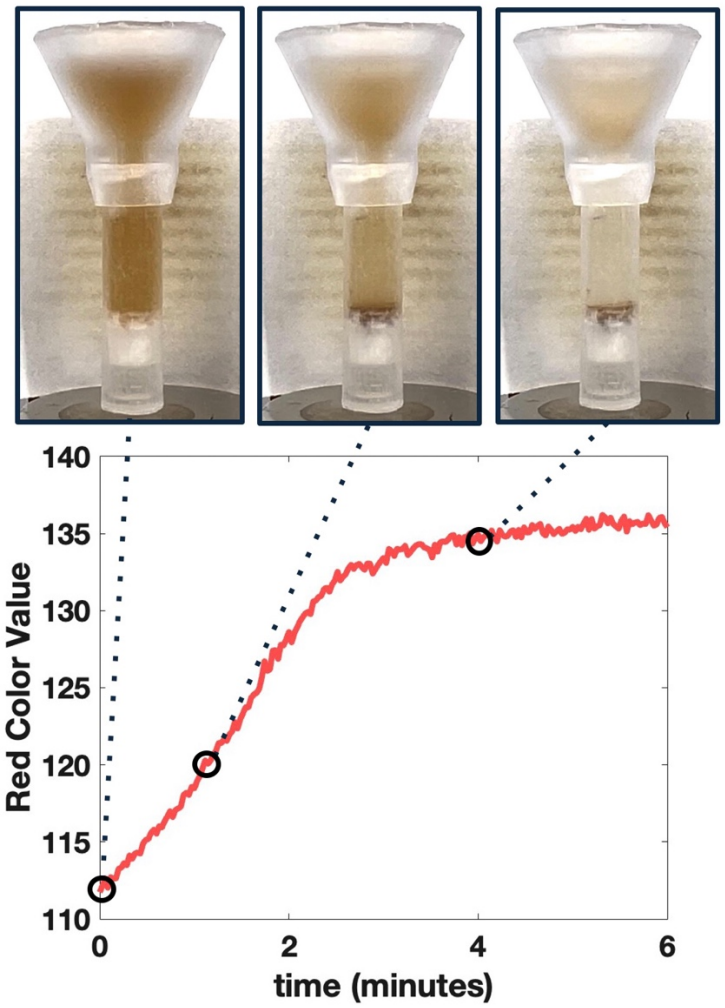

Figure 26. Images of a cassette with a funnel attachment as magnetic beads are pulled down in a saliva sample. The data represents the bead transfer from the saliva sample to the saliva-TRAP interface. The red color value was extracted from a small window in the images just under the bottom of the funnel hardware.

5.3.2 Automatic Reagent Addition & Mixing using TRAPs

Automatic reagent additions are necessary in PoC devices that depend on reactions that must run in series. In our SARS-CoV-2 saliva test, protease must lyse virus particles and then be deactivated before the solution is added to LAMP reagents. Otherwise, the protease will digest the polymerase and reverse transcriptase. Therefore, these reagents

must be partitioned during the lysis step and automatically combined after the protease is deactivated. Breaching TRAPs integrated into a cassette enable this function.

To demonstrate reagent partitioning and automated addition/mixing of reagents within the cassette, we loaded DNA and intercalating dye – partitioned by a thin hexacosane TRAP – into a cassette and placed the cassette into the instrument. Fluorescence near the bottom of the cassette was recorded while heat was applied to the cassette. The measured fluorescence and the temperature of the cassette are shown in Figure 27. The fluorescence signal demonstrates that the DNA and intercalating dye remain partitioned until the temperature reaches the melt temperature of the TRAP. Once the TRAP melts, the DNA and dye are combined, and the fluorescence signal immediately increases, demonstrating rapid mixing of the reagents. The reaction equilibrates within 1 minute of the breaching of the TRAP.

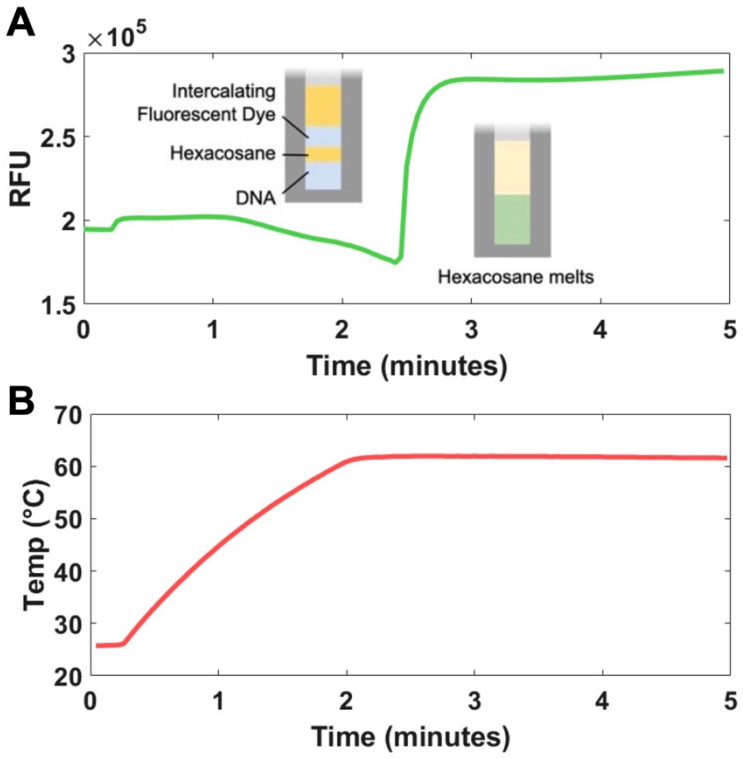

Figure 27. (A) Fluorescence readout of the bottom region in a cassette during a hexacosane melt, which causes intercalating fluorescent dye to mix with a solution of DNA. (B) The temperature profile shows that the hexacosane breaches within 1 minute of when the cassette reaches the melting point (~57 °C).

5.4.3 LAMP Detects Virus with Small Volumes of Saliva

Saliva is known to inhibit nucleic acid amplification tests including LAMP.[91] However, when using just 5 µL of a saliva sample (20% of the volume of the LAMP reaction) that underwent an incubation with Proteinase K, LAMP reagents still operate effectively. Based on Figure 28A, we can clearly see a difference in the negative control sample and the positive samples. We can even distinguish between the different concentrations of positive samples quite well. Looking at Figure 28B, however, it becomes clear that by adding the bead isolation and rinse steps to the protocol, we lose

some ability to distinguish between different concentrations and the assay loses sensitivity.

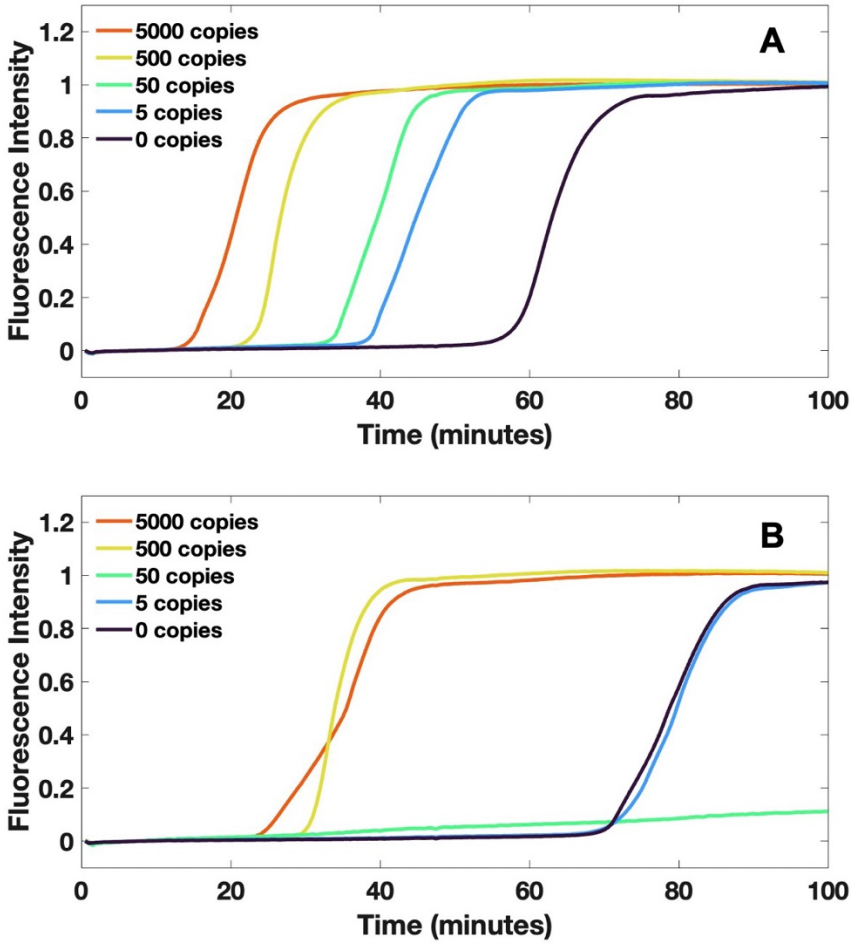

Figure 28. (A) Fluorescence curves resulting from adding 5 µL of SARS-CoV-2-spiked saliva samples directly to LAMP reaction solutions and running the reaction at 65 °C. (B) Fluorescence curves resulting from adding 5 µL of saliva-free, purified (via bead capture and rinses) SARS-CoV-2 samples.

5.4.4 LAMP in the Saliva-STAT

To demonstrate that the Saliva-STAT instrument and cassette can reliably implement LAMP amplification of viral RNA, we added a range of concentrations of SARS-CoV-2 RNA (i.e., after Proteinase K digestion of the virus) to LAMP master mix in Saliva-

STAT cassettes and capped the reaction volume with eicosane. Figure 29A shows representative amplification curves for 500 copies and 0 copies, indicating that the instrument can easily measure the amplification signal and that LAMP is not inhibited by the cassette or the alkane. Figure 29B presents the mean times-to-positive for 500, 50, 5, and 0 copies in the LAMP reaction in the Saliva-STAT. The data demonstrates that we can reliably differentiate 5 viral copies from a blank sample.

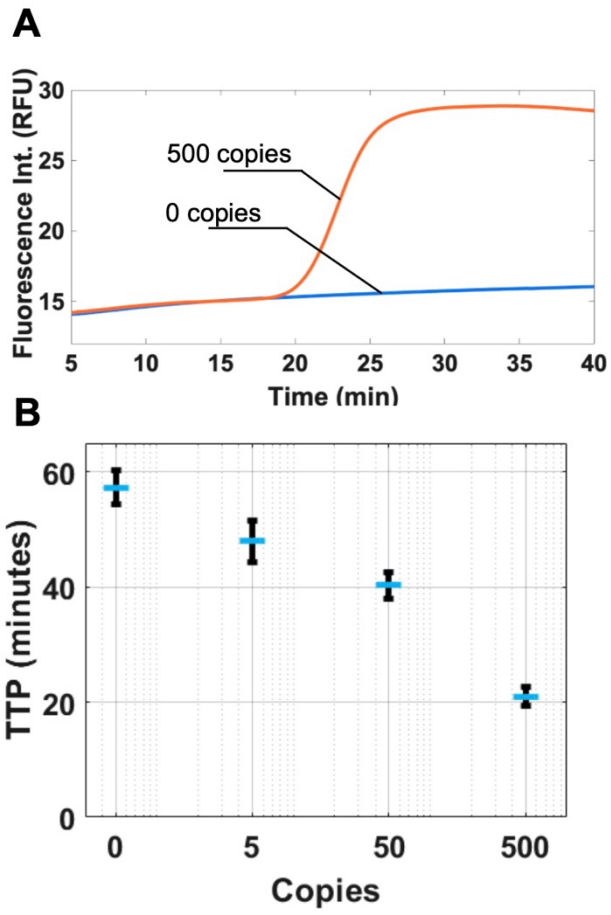

Figure 29. LAMP in the Saliva-STAT. (A) Representative amplification curves for 500 copies and 0 copies of viral RNA in the cassette under a layer of eicosane, heated and measured in the Saliva-STAT instrument. (B) Mean times-to-positive for 0, 5, 50, and 500 copies of RNA in the Saliva-STAT cassette under a layer of eicosane, heated and measured in the Saliva-STAT instrument (N=3). Error bars represent +/- one standard deviation.

5.4.5 Sample-to-Answer Detection of Virus from Large-Volume Saliva Samples

In previously reported demonstrations of point-of-care saliva-based diagnostics, precisely measured small volumes of saliva were used. This is often required because the devices utilize microfluidics for sample processing. However, it is not practical to expect a user to dispense a precise, small volume of saliva. To address this challenge, the saliva STAT is designed to accommodate large sample volumes (500 μL). The combination of paramagnetic beads and the TRAPs enables the recovery of the virus particles from the large-volume sample and the automated transfer into the precisely pre-measured small-volume assay.

We tested 500 μL saliva samples spiked with SARS-CoV-2 at concentrations of 200, 20, 2, and 0.2 copies/μL (N=5). Samples that resulted in a time-to-positive (TTP) of less than 60 minutes from initiating the assay were considered positive for the virus. As shown in Figure 30, all spiked samples were determined to be positive by the saliva STAT, while all five samples that were not spiked with virus were determined to be negative by the saliva STAT.

Accommodating larger volumes is advantageous for self-testing. Intuitively, it is also expected to have a performance advantage, as a larger sample volume will contain more viral copies. To illustrate this, we also tested 25 μL saliva samples spiked with SARS-CoV-2 at concentrations of 2 and 0.2 copies/μL (N=5). For 2 copies/μL, 4/5 samples were correctly identified as positive, and for 0.2 copies/μL, only 2/5 samples were correctly identified as positive. When using 500 μL samples, all samples at these concentrations were correctly identified as positive.

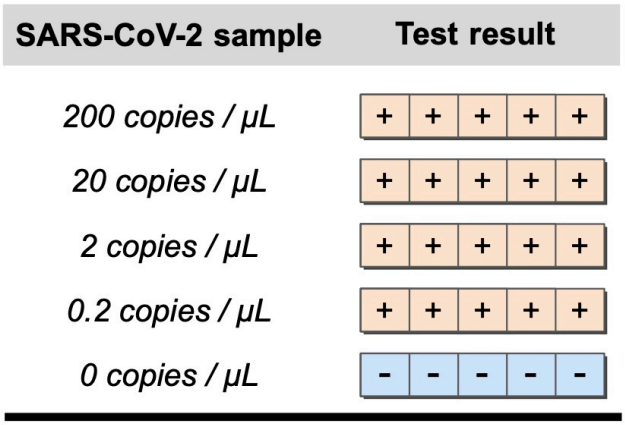

Figure 30. Compiled Saliva-STAT test results using 500 µL saliva samples with varying concentrations of SARS-CoV-2.

5.5 Conclusion

In this work, we demonstrated the sample-to-answer detection of SARS-CoV-2 in saliva samples using a fully automated, user-friendly, battery-powered handheld device and a low-cost, easily manufacturable sample cassette. Currently, point-of-care saliva-based nucleic acid amplification tests for respiratory pathogens are not available because of the challenges of automating all of the assay steps in a low-cost and portable system. We leverage a magnetofluidic assay with TRAPs to enable (i) the recovery of virus particles from the large-volume saliva sample, (ii) the addition of the virus to lysis reagent, and (iii) the addition of the released RNA to the LAMP reagents. We accomplish all of these steps with a handheld instrument and an easily manufacturable assay cassette. The saliva STAT correctly identified 20/20 spiked samples as positive, including five samples with 0.2 copies/µL of SARS-CoV-2 virus, while also correctly identifying five negative samples. We also demonstrated the value of a platform that is

capable of testing large-volume samples, as we showed that the sensitivity of testing 500 μL samples was significantly better than when testing 25 μL samples.

In future work, we will broaden the application of the Saliva-STAT to other respiratory viruses that can be detected in saliva. One only needs to change the capture aptamer on the paramagnetic beads and the LAMP primers to adapt the Saliva-STAT to other viruses. In addition, we plan to add an additional optical channel to the instrument to enable the simultaneous screening of multiple viruses, such as SARS-CoV-2 and influenza H5N1 (i.e., avian influenza).

Chapter 6: Conclusions

6.1 Thermally Responsive Alkane Partitions for Assay Automation

6.1.1 Summary

A new approach to enable sample-to-answer diagnostics that utilizes thermally responsive alkane partitions (TRAPs) as automated pseudo-valves was introduced, and geometric design rules for different TRAP behaviors and magnetic bead manipulation were established. Robust to agitation, TRAPs combined with the magnetic manipulation of microbeads enable the pumpless automation of all steps in complex assays. These assays operate in a mesofluidic scale rather than a microfluidic scale which is important as it makes them cheap to produce, resistant to clogging, and easy to load and dry reagents into the assay. In relatively narrow channel geometries, liquified alkane partitions continue to separate reagents on each side of the partition while enabling the transition of magnetic beads from one reagent to the next, replacing manual pipetting steps in conventional assays. In addition, in relatively broader geometries, liquified partitions breach, enabling the addition/mixing of preloaded reagents. Through calculation and experimentation, geometric design rules for implementing the stationary and removable partitions in fluidic channels were described. Also, magnetic microbeads can be pulled through liquified stationary TRAPs without disrupting partition integrity and without disrupting bound protein complexes attached at the microbead surface. The TRAP technology introduced here can enable a new low-cost and equipment-free approach for fully automated sample-to-answer diagnostics.

6.1.2 Scientific Contributions

- Developed and characterized a new point-of-care-enabling technology: the Thermally Responsive Alkane Partition (TRAP)
- Established design rules that result in removable TRAPs, which enable automatic reagent combination
- Established design rules that result in stationary TRAPs, which enable advanced magnetofluidic assays
- Determined parameters to enable beads to be pulled through stationary TRAPs without substantial liquid leakage through the TRAPs
- Demonstrated use-cases for TRAPs in which immunoassay pipette transfers were successfully replaced with functionalized bead transfers through TRAPs

6.2 Sample-to-Answer Detection of SARS-CoV-2 Viremia Using Thermally Responsive Alkane Partitions

6.2.1 Summary

TRAPs were applied for the sample-to-answer detection of viruses in blood using a low-cost portable device and easily manufacturable cassettes. Specifically, the detection of SARS-CoV-2 in spiked blood samples was made possible with the system developed here. 100% of blood samples spiked with 500 or more copies were classified as positive, while more than 70% of samples with just 5 virus copies were classified as positive. Successfully testing blood samples in this manner (i.e. without any processing) is a capability that, up until this point, has not been possible in point-of-care-friendly hardware. In addition, viremia in COVID-19 patient samples was

detected with good agreement to conventional RT-qPCR. This sample-to-answer system could be used to rapidly diagnose SARS-CoV-2 viremia at the point of care, leading to better health outcomes for patients with severe COVID-19 disease. With minor adjustments to the assay, the system can also be applied to the diagnosis of other life-threatening bloodborne viral diseases, including Hepatitis C and HIV.

6.2.2 Scientific Contributions

- Developed a mechanism by which disease biomarkers can be automatically isolated and transferred from a sample into a new solution
- Demonstrated automatic stepwise progression of incubations and additions of reagents via removable TRAPs
- Developed a sample-to-answer workflow in which virus particles are purified from blood, lysed, and their nucleic acid amplified and detected
- Demonstrated successful sub-65 °C sample-to-answer diagnosis of viremia for the first time in hardware with less than a $100 manufacturing cost
- Provided a point-of-care sample preparation workflow which could potentially be applied to a slew of viruses, bacteria, and other biomarkers to automatically prepare the sample and detect said biomarkers
- Designed a portable instrument capable of fluorescence measurements, controlled heating, and nucleic acid amplification detection

6.3 CoV-STAT: a SARS-CoV-2 Sample-to-Answer Test for Saliva

6.3.1 Summary

Building off of the success of the prototype device detailed in Chapter 4 – which presented a solution to automatic sample preparation in a diagnostic device via thermally responsive alkane partitions – this chapter demonstrated the automatic sample-to-answer detection of SARS-CoV-2 in saliva samples using a user-friendly, battery-powered handheld device, named "Saliva-STAT." The device is a standalone system that, when charged, does not require an outlet or computer to run. The device was tested using small volume (25 μL) samples of saliva as well as large volume (500 μL) samples, demonstrating the sample volume independency of our assay. This is especially important considering larger volumes are typically required in saliva assays, but usually are not compatible with microfluidics and other PoC assays without isolating a precise small amount of the collected sample (thus, not sample-to-answer). The Saliva-STAT correctly identified 20/20 spiked samples as positive, including five samples with 0.2 copies/μL of SARS-CoV-2 virus, while also correctly identifying five negative samples. This device could be used by clinicians, both in offices and mobile, to provide accurate SARS-CoV-2 genomic tests at the point of care. As with the system developed in Chapter 4, minor adjustments to the assay could allow this device to be applied to the diagnosis of other life-threatening bloodborne viral diseases as well, including Hepatitis C and HIV.

6.3.2 Scientific Contributions

- Demonstrated a workflow in which sample volume from a patient need not be precisely controlled in order to acquire an accurate diagnosis from nucleic acid detection chemistry
- Developed novel hardware which has potential to streamline the diagnostic pathway of many diseases in complex samples such as blood and saliva, advancing the state-of-the-art of point-of-care diagnostic technologies
- Characterized behavior of magnetic beads within TRAP assays, building a foundation for future work to reference

6.4 Future Work & Potential Significance

The immediate next steps following my work here would be to expand the applications of the technology I have developed, as well as implement modifications to the assay itself to increase its capabilities. Next, we should explore various samples to determine the limits of the TRAP assay's capabilities.

6.4.1 HCV, HIV, Dengue

Different viruses should be tested including Hepatitis C, HIV, and Dengue which currently do not have point-of-care devices effective enough to combat the spread of the diseases. Capture aptamers and LAMP primers for several viruses exist and the fundamental technology should still function properly when switching between sets of virus, aptamers, and primers, though this needs to be tested. As detrimental as these viruses are and as promising as the technology developed in this work has been,

building a diagnostic system for each of these viruses using newly developed technology is imminent.

6.4.2 Wastewater

Analyzing wastewater for viruses and other nucleic acid material enables public health officials to track infectious diseases on a population-wide scale, allowing them to make more informed decisions on policy. This could prove especially useful when the next pandemic arrives; we could monitor and predict disease rates by diagnosing wastewater samples instead of relying solely on self-reporting. However, the current diagnostic infrastructure does not allow for diagnostic answers rapid enough to provide health officials information in time to make up-to-date decisions. Rapid point-of-care devices are needed and a device utilizing the technology developed in this work could be a suitable solution.

6.4.3 Non-Virus Biomarkers

Non-virus biomarkers could also be tested utilizing the technology. Extracellular vesicles (EVs), nucleic acid fragments (e.g. cell-free DNA circulating in the bloodstream), and other extracellular particles could possibly be detected via the TRAP assay developed here. To apply the technology to these biomarkers, it may only be a matter of changing out the capture mechanism onto magnetic beads and/or changing the detection reaction on the other side of the stationary TRAP. For example, in an assay where EVs need to be isolated and lysed, surfactants may need to be introduced in place of (or in addition to) protease as EVs have fewer proteins in their membranes compared to viruses and thus may require a more aggressive lysis reaction.

6.4.4 Assay Improvements

Work should be done on replacing the streptavidin magnetic beads with magnetic beads capable of non-specifically capturing any virus genome or particle present in a sample. This would make the workflow simpler, without a reliance on the existence or the binding affinities of different aptamers. Multiplexing (detecting multiple genomes or biomarkers at once) is another capability that could be added to this assay. Multiplexing may be possible by using multiple sets of aptamers, primers, and different colored fluorophores in the same assay, or by extending the assay beyond the initial detection reaction with more TRAPs and/or different detection reactions. Initial proof-of-concept work has been done on making TRAP assays functional when the reagents are lyophilized. TRAP assays with lyophilized reagents will store for longer periods of time without worry of proteins degrading or need for refrigeration. More work needs to be done to explore limitations and to optimize TRAP assays that contain lyophilized reagents.

6.4.5 Final Note

All in all, the science and technologies developed in this dissertation have advanced the state-of-the-art of point-of-care diagnostics. These technologies provide new avenues for further progress and development of sample-to-answer systems capable of automatically diagnosing diseases from a wide variety of samples using accessible hardware. This work will universally reduce the barrier of access to proper diagnoses and treatments.

Bibliography

(1) Perry, L.; Malkin, R. Effectiveness of Medical Equipment Donations to Improve Health Systems: How Much Medical Equipment Is Broken in the Developing World? *Med Biol Eng Comput* **2011**, *49* (7), 719–722. https://doi.org/10.1007/s11517-011-0786-3.

(2) Gatrad, A. R.; Gatrad, S.; Gatrad, A. Equipment Donation to Developing Countries. *Anaesthesia* **2007**, *62* (s1), 90–95. https://doi.org/10.1111/j.1365-2044.2007.05309.x.

(3) Kettler, H.; White, K.; Hawkes, S. Mapping the Landscape of Diagnostics for Sexually Transmitted Infections: Key Findings and Recommendations, 2004. https://iris.who.int/bitstream/handle/10665/68990/TDR_STI_IDE_04.1.pdf.

(4) CLIA Categorizations, 2023. https://www.fda.gov/medical-devices/ivd-regulatory-assistance/clia-categorizations (accessed 2024-04-15).

(5) O'Connell, R. J.; Merritt, T. M.; Malia, J. A.; VanCott, T. C.; Dolan, M. J.; Zahwa, H.; Bradley, W. P.; Branson, B. M.; Michael, N. L.; De Witt, C. C. Performance of the OraQuick Rapid Antibody Test for Diagnosis of Human Immunodeficiency Virus Type 1 Infection in Patients with Various Levels of Exposure to Highly Active Antiretroviral Therapy. *J Clin Microbiol* **2003**, *41* (5), 2153–2155. https://doi.org/10.1128/JCM.41.5.2153-2155.2003.

(6) Panfilova, E. Development of a Prototype Lateral Flow Immunoassay of Cortisol in Saliva for Daily Monitoring of Stress. *Biosensors* **2021**, *11* (5), 146. https://doi.org/10.3390/bios11050146.

(7) Zangheri, M.; Cevenini, L.; Anfossi, L.; Baggiani, C.; Simoni, P.; Di Nardo, F.; Roda, A. A Simple and Compact Smartphone Accessory for Quantitative Chemiluminescence-Based Lateral Flow Immunoassay for Salivary Cortisol Detection. *Biosensors and Bioelectronics* **2015**, *64*, 63–68. https://doi.org/10.1016/j.bios.2014.08.048.

(8) Yang, X.; Liu, X.; Gu, B.; Liu, H.; Xiao, R.; Wang, C.; Wang, S. Quantitative and Simultaneous Detection of Two Inflammation Biomarkers via a Fluorescent Lateral Flow Immunoassay Using Dual-Color SiO2@QD Nanotags. *Microchim Acta* **2020**, *187* (10), 570. https://doi.org/10.1007/s00604-020-04555-6.

(9) Gannon, B. M.; Glesby, M. J.; Finkelstein, J. L.; Raj, T.; Erickson, D.; Mehta, S. A Point-of-Care Assay for Alpha-1-Acid Glycoprotein as a Diagnostic Tool for Rapid, Mobile-Based Determination of Inflammation. *Current Research in Biotechnology* **2019**, *1*, 41–48. https://doi.org/10.1016/j.crbiot.2019.09.002.

(10) Teerinen, T.; Lappalainen, T.; Erho, T. A Paper-Based Lateral Flow Assay for Morphine. *Anal Bioanal Chem* **2014**, *406* (24), 5955–5965. https://doi.org/10.1007/s00216-014-8001-7.

(11) Angelini, D. J.; Biggs, T. D.; Maughan, M. N.; Feasel, M. G.; Sisco, E.; Sekowski, J. W. Evaluation of a Lateral Flow Immunoassay for the Detection of the Synthetic Opioid Fentanyl. *Forensic Science International* **2019**, *300*, 75–81. https://doi.org/10.1016/j.forsciint.2019.04.019.

(12) Plouffe, B. D.; Murthy, S. K. Fluorescence-based Lateral Flow Assays for Rapid Oral Fluid Roadside Detection of Cannabis Use. *Electrophoresis* **2017**, *38* (3–4), 501–506. https://doi.org/10.1002/elps.201600075.

(13) Wang, C.; Peng, J.; Liu, D.-F.; Xing, K.-Y.; Zhang, G.-G.; Huang, Z.; Cheng, S.; Zhu, F.-F.; Duan, M.-L.; Zhang, K.-Y.; Yuan, M.-F.; Lai, W.-H. Lateral Flow Immunoassay Integrated with Competitive and Sandwich Models for the Detection of Aflatoxin M1 and Escherichia Coli O157:H7 in Milk. *Journal of Dairy Science* **2018**, *101* (10), 8767–8777. https://doi.org/10.3168/jds.2018-14655.

(14) Wu, K.-H.; Huang, W.-C.; Shyu, R.-H.; Chang, S.-C. Silver Nanoparticle-Base Lateral Flow Immunoassay for Rapid Detection of Staphylococcal Enterotoxin B in Milk and Honey. *Journal of Inorganic Biochemistry* **2020**, *210*, 111163. https://doi.org/10.1016/j.jinorgbio.2020.111163.

(15) Moyano, A.; Serrano-Pertierra, E.; Duque, J. M.; Ramos, V.; Teruel-Barandiarán, E.; Fernández-Sánchez, M. T.; Salvador, M.; Martínez-García, J. C.; Sánchez, L.; García-Flórez, L.; Rivas, M.; Blanco-López, M. D. C. Magnetic Lateral Flow Immunoassay for Small Extracellular Vesicles Quantification: Application to Colorectal Cancer Biomarker Detection. *Sensors* **2021**, *21* (11), 3756. https://doi.org/10.3390/s21113756.

(16) Bayoumy, S.; Hyytiä, H.; Leivo, J.; Talha, S. M.; Huhtinen, K.; Poutanen, M.; Hynninen, J.; Perheentupa, A.; Lamminmäki, U.; Gidwani, K.; Pettersson, K. Glycovariant-Based Lateral Flow Immunoassay to Detect Ovarian Cancer–Associated Serum CA125. *Commun Biol* **2020**, *3* (1), 460. https://doi.org/10.1038/s42003-020-01191-x.

(17) Brangel, P.; Sobarzo, A.; Parolo, C.; Miller, B. S.; Howes, P. D.; Gelkop, S.; Lutwama, J. J.; Dye, J. M.; McKendry, R. A.; Lobel, L.; Stevens, M. M. A Serological Point-of-Care Test for the Detection of IgG Antibodies against Ebola Virus in Human Survivors. *ACS Nano* **2018**, *12* (1), 63–73. https://doi.org/10.1021/acsnano.7b07021.

(18) Wonderly, B.; Jones, S.; Gatton, M. L.; Barber, J.; Killip, M.; Hudson, C.; Carter, L.; Brooks, T.; Simpson, A. J. H.; Semper, A.; Urassa, W.; Chua, A.; Perkins, M.; Boehme, C. Comparative Performance of Four Rapid Ebola Antigen-Detection Lateral Flow Immunoassays during the 2014-2016 Ebola Epidemic in West Africa. *PLoS ONE* **2019**, *14* (3), e0212113. https://doi.org/10.1371/journal.pone.0212113.

(19) Phan, J. C.; Pettitt, J.; George, J. S.; Fakoli, L. S.; Taweh, F. M.; Bateman, S. L.; Bennett, R. S.; Norris, S. L.; Spinnler, D. A.; Pimentel, G.; Sahr, P. K.; Bolay, F. K.; Schoepp, R. J. Lateral Flow Immunoassays for Ebola Virus Disease Detection in Liberia. *J Infect Dis.* **2016**, *214* (suppl 3), S222–S228. https://doi.org/10.1093/infdis/jiw251.

(20) Hwang, S. G.; Ha, K.; Guk, K.; Lee, D. K.; Eom, G.; Song, S.; Kang, T.; Park, H.; Jung, J.; Lim, E.-K. Rapid and Simple Detection of Tamiflu-Resistant Influenza Virus: Development of Oseltamivir Derivative-Based Lateral Flow Biosensor for Point-of-Care (POC) Diagnostics. *Sci Rep* **2018**, *8* (1), 12999. https://doi.org/10.1038/s41598-018-31311-x.

(21) Zhang, J.; Gui, X.; Zheng, Q.; Chen, Y.; Ge, S.; Zhang, J.; Xia, N. An HRP-labeled Lateral Flow Immunoassay for Rapid Simultaneous Detection and Differentiation of Influenza A and B Viruses. *Journal of Medical Virology* **2019**, *91* (3), 503–507. https://doi.org/10.1002/jmv.25322.

(22) Leonardi, G. P.; Wilson, A. M.; Zuretti, A. R. Comparison of Conventional Lateral-Flow Assays and a New Fluorescent Immunoassay to Detect Influenza Viruses. *Journal of Virological Methods* **2013**, *189* (2), 379–382. https://doi.org/10.1016/j.jviromet.2013.02.008.
(23) Li, H.; Steckl, A. J. Paper Microfluidics for Point-of-Care Blood-Based Analysis and Diagnostics. *Anal. Chem.* **2019**, *91* (1), 352–371. https://doi.org/10.1021/acs.analchem.8b03636.
(24) Liu, C.; Mauk, M.; Gross, R.; Bushman, F. D.; Edelstein, P. H.; Collman, R. G.; Bau, H. H. Membrane-Based, Sedimentation-Assisted Plasma Separator for Point-of-Care Applications. *Anal. Chem.* **2013**, *85* (21), 10463–10470. https://doi.org/10.1021/ac402459h.
(25) Kubista, M.; Andrade, J. M.; Bengtsson, M.; Forootan, A.; Jonák, J.; Lind, K.; Sindelka, R.; Sjöback, R.; Sjögreen, B.; Strömbom, L.; Ståhlberg, A.; Zoric, N. The Real-Time Polymerase Chain Reaction. *Molecular Aspects of Medicine* **2006**, *27* (2–3), 95–125. https://doi.org/10.1016/j.mam.2005.12.007.
(26) Compton, J. Nucleic Acid Sequence-Based Amplification. *Nature* **1991**, *350* (6313), 91–92. https://doi.org/10.1038/350091a0.
(27) Walker, G. T.; Little, M. C.; Nadeau, J. G.; Shank, D. D. Isothermal in Vitro Amplification of DNA by a Restriction Enzyme/DNA Polymerase System. *Proc. Natl. Acad. Sci. U.S.A.* **1992**, *89* (1), 392–396. https://doi.org/10.1073/pnas.89.1.392.
(28) Lizardi, P. M.; Huang, X.; Zhu, Z.; Bray-Ward, P.; Thomas, D. C.; Ward, D. C. Mutation Detection and Single-Molecule Counting Using Isothermal Rolling-Circle Amplification. *Nat Genet* **1998**, *19* (3), 225–232. https://doi.org/10.1038/898.
(29) Notomi, T. Loop-Mediated Isothermal Amplification of DNA. *Nucleic Acids Research* **2000**, *28* (12), 63e–663. https://doi.org/10.1093/nar/28.12.e63.
(30) Vincent, M.; Xu, Y.; Kong, H. Helicase-dependent Isothermal DNA Amplification. *EMBO Reports* **2004**, *5* (8), 795–800. https://doi.org/10.1038/sj.embor.7400200.
(31) Piepenburg, O.; Williams, C. H.; Stemple, D. L.; Armes, N. A. DNA Detection Using Recombination Proteins. *PLoS Biol* **2006**, *4* (7), e204. https://doi.org/10.1371/journal.pbio.0040204.
(32) Van Ness, J.; Van Ness, L. K.; Galas, D. J. Isothermal Reactions for the Amplification of Oligonucleotides. *Proc. Natl. Acad. Sci. U.S.A.* **2003**, *100* (8), 4504–4509. https://doi.org/10.1073/pnas.0730811100.
(33) Li, Y.; Kim, H.-J.; Zheng, C.; Chow, W. H. A.; Lim, J.; Keenan, B.; Pan, X.; Lemieux, B.; Kong, H. Primase-Based Whole Genome Amplification. *Nucleic Acids Research* **2008**, *36* (13), e79–e79. https://doi.org/10.1093/nar/gkn377.
(34) Buser, J. R.; Diesburg, S.; Singleton, J.; Guelig, D.; Bishop, J. D.; Zentner, C.; Burton, R.; LaBarre, P.; Yager, P.; Weigl, B. H. Precision Chemical Heating for Diagnostic Devices. *Lab Chip* **2015**, *15* (23), 4423–4432. https://doi.org/10.1039/C5LC01053E.
(35) Goertz, J. P.; Colvin, K. M.; Lippe, A. B.; Daristotle, J. L.; Kofinas, P.; White, I. M. Multistage Chemical Heating for Instrument-Free Biosensing. *ACS Appl.*

Mater. Interfaces **2018**, *10* (39), 33043–33048. https://doi.org/10.1021/acsami.8b11611.
(36) De Puig, H.; Lee, R. A.; Najjar, D.; Tan, X.; Soenksen, L. R.; Angenent-Mari, N. M.; Donghia, N. M.; Weckman, N. E.; Ory, A.; Ng, C. F.; Nguyen, P. Q.; Mao, A. S.; Ferrante, T. C.; Lansberry, G.; Sallum, H.; Niemi, J.; Collins, J. J. Minimally Instrumented SHERLOCK (miSHERLOCK) for CRISPR-Based Point-of-Care Diagnosis of SARS-CoV-2 and Emerging Variants. *Sci. Adv.* **2021**, *7* (32), eabh2944. https://doi.org/10.1126/sciadv.abh2944.
(37) Fahle, G. A.; Fischer, S. H. Comparison of Six Commercial DNA Extraction Kits for Recovery of Cytomegalovirus DNA from Spiked Human Specimens. *J Clin Microbiol* **2000**, *38* (10), 3860–3863. https://doi.org/10.1128/JCM.38.10.3860-3863.2000.
(38) Li, Z.; Yi, Y.; Luo, X.; Xiong, N.; Liu, Y.; Li, S.; Sun, R.; Wang, Y.; Hu, B.; Chen, W.; Zhang, Y.; Wang, J.; Huang, B.; Lin, Y.; Yang, J.; Cai, W.; Wang, X.; Cheng, J.; Chen, Z.; Sun, K.; Pan, W.; Zhan, Z.; Chen, L.; Ye, F. Development and Clinical Application of a Rapid IgM-IgG Combined Antibody Test for SARS-CoV-2 Infection Diagnosis. *Journal of Medical Virology* **2020**, *92* (9), 1518–1524. https://doi.org/10.1002/jmv.25727.
(39) Noh, J. Y.; Yoon, S.-W.; Kim, Y.; Lo, T. V.; Ahn, M.-J.; Jung, M.-C.; Le, T. B.; Na, W.; Song, D.; Le, V. P.; Haam, S.; Jeong, D. G.; Kim, H. K. Pipetting-Based Immunoassay for Point-of-Care Testing: Application for Detection of the Influenza A Virus. *Sci Rep* **2019**, *9* (1), 16661. https://doi.org/10.1038/s41598-019-53083-8.
(40) Lu, G.; Zhang, J.; Zhang, C.; Li, X.; Shi, D.; Yang, Z.; Wang, C. One-Step Reverse-Transcription FRET-PCR for Differential Detection of Five Ebolavirus Species. *PLoS ONE* **2015**, *10* (5), e0126281. https://doi.org/10.1371/journal.pone.0126281.
(41) Dirks, R. M.; Pierce, N. A. Triggered Amplification by Hybridization Chain Reaction. *Proc. Natl. Acad. Sci. U.S.A.* **2004**, *101* (43), 15275–15278. https://doi.org/10.1073/pnas.0407024101.
(42) Amanat, F.; Stadlbauer, D.; Strohmeier, S.; Nguyen, T. H. O.; Chromikova, V.; McMahon, M.; Jiang, K.; Arunkumar, G. A.; Jurczyszak, D.; Polanco, J.; Bermudez-Gonzalez, M.; Kleiner, G.; Aydillo, T.; Miorin, L.; Fierer, D. S.; Lugo, L. A.; Kojic, E. M.; Stoever, J.; Liu, S. T. H.; Cunningham-Rundles, C.; Felgner, P. L.; Moran, T.; García-Sastre, A.; Caplivski, D.; Cheng, A. C.; Kedzierska, K.; Vapalahti, O.; Hepojoki, J. M.; Simon, V.; Krammer, F. A Serological Assay to Detect SARS-CoV-2 Seroconversion in Humans. *Nat Med* **2020**, *26* (7), 1033–1036. https://doi.org/10.1038/s41591-020-0913-5.
(43) Sundberg, S. O.; Wittwer, C. T.; Gao, C.; Gale, B. K. Spinning Disk Platform for Microfluidic Digital Polymerase Chain Reaction. *Anal. Chem.* **2010**, *82* (4), 1546–1550. https://doi.org/10.1021/ac902398c.
(44) Stumpf, F.; Schwemmer, F.; Hutzenlaub, T.; Baumann, D.; Strohmeier, O.; Dingemanns, G.; Simons, G.; Sager, C.; Plobner, L.; Von Stetten, F.; Zengerle, R.; Mark, D. LabDisk with Complete Reagent Prestorage for Sample-to-Answer Nucleic Acid Based Detection of Respiratory Pathogens Verified with Influenza

A H3N2 Virus. *Lab Chip* **2016**, *16* (1), 199–207. https://doi.org/10.1039/C5LC00871A.
(45) Chin, C. D.; Laksanasopin, T.; Cheung, Y. K.; Steinmiller, D.; Linder, V.; Parsa, H.; Wang, J.; Moore, H.; Rouse, R.; Umviligihozo, G.; Karita, E.; Mwambarangwe, L.; Braunstein, S. L.; Van De Wijgert, J.; Sahabo, R.; Justman, J. E.; El-Sadr, W.; Sia, S. K. Microfluidics-Based Diagnostics of Infectious Diseases in the Developing World. *Nat Med* **2011**, *17* (8), 1015–1019. https://doi.org/10.1038/nm.2408.
(46) Zhang, Y.; Park, S.; Liu, K.; Tsuan, J.; Yang, S.; Wang, T.-H. A Surface Topography Assisted Droplet Manipulation Platform for Biomarker Detection and Pathogen Identification. *Lab Chip* **2011**, *11* (3), 398–406. https://doi.org/10.1039/C0LC00296H.
(47) Berry, S. M.; Alarid, E. T.; Beebe, D. J. One-Step Purification of Nucleic Acid for Gene Expression Analysis via Immiscible Filtration Assisted by Surface Tension (IFAST). *Lab Chip* **2011**, *11* (10), 1747. https://doi.org/10.1039/c1lc00004g.
(48) Chiou, C.-H.; Jin Shin, D.; Zhang, Y.; Wang, T.-H. Topography-Assisted Electromagnetic Platform for Blood-to-PCR in a Droplet. *Biosensors and Bioelectronics* **2013**, *50*, 91–99. https://doi.org/10.1016/j.bios.2013.06.011.
(49) Lehmann, U.; Vandevyver, C.; Parashar, V. K.; Gijs, M. A. M. Droplet-Based DNA Purification in a Magnetic Lab-on-a-Chip. *Angew Chem Int Ed* **2006**, *45* (19), 3062–3067. https://doi.org/10.1002/anie.200503624.
(50) Shin, D. J.; Trick, A. Y.; Hsieh, Y.-H.; Thomas, D. L.; Wang, T.-H. Sample-to-Answer Droplet Magnetofluidic Platform for Point-of-Care Hepatitis C Viral Load Quantitation. *Sci Rep* **2018**, *8* (1), 9793. https://doi.org/10.1038/s41598-018-28124-3.
(51) Shin, D. J.; Athamanolap, P.; Chen, L.; Hardick, J.; Lewis, M.; Hsieh, Y. H.; Rothman, R. E.; Gaydos, C. A.; Wang, T. H. Mobile Nucleic Acid Amplification Testing (mobiNAAT) for Chlamydia Trachomatis Screening in Hospital Emergency Department Settings. *Sci Rep* **2017**, *7* (1), 4495. https://doi.org/10.1038/s41598-017-04781-8.
(52) Pipper, J.; Inoue, M.; Ng, L. F.-P.; Neuzil, P.; Zhang, Y.; Novak, L. Catching Bird Flu in a Droplet. *Nat Med* **2007**, *13* (10), 1259–1263. https://doi.org/10.1038/nm1634.
(53) Thurgood, P.; Baratchi, S.; Szydzik, C.; Mitchell, A.; Khoshmanesh, K. Porous PDMS Structures for the Storage and Release of Aqueous Solutions into Fluidic Environments. *Lab Chip* **2017**, *17* (14), 2517–2527. https://doi.org/10.1039/C7LC00350A.
(54) Chen, D.; Mauk, M.; Qiu, X.; Liu, C.; Kim, J.; Ramprasad, S.; Ongagna, S.; Abrams, W. R.; Malamud, D.; Corstjens, P. L. A. M.; Bau, H. H. An Integrated, Self-Contained Microfluidic Cassette for Isolation, Amplification, and Detection of Nucleic Acids. *Biomed Microdevices* **2010**, *12* (4), 705–719. https://doi.org/10.1007/s10544-010-9423-4.
(55) Czurratis, D.; Beyl, Y.; Grimm, A.; Brettschneider, T.; Zinober, S.; Lärmer, F.; Zengerle, R. Liquids On-Chip: Direct Storage and Release Employing Micro-

Perforated Vapor Barrier Films. *Lab Chip* **2015**, *15* (13), 2887–2895. https://doi.org/10.1039/C5LC00510H.
(56) Xu, G.; Hsieh, T.-M.; Lee, D. Y. S.; Ali, E. M.; Xie, H.; Looi, X. L.; Koay, E. S.-C.; Li, M.-H.; Ying, J. Y. A Self-Contained All-in-One Cartridge for Sample Preparation and Real-Time PCR in Rapid Influenza Diagnosis. *Lab Chip* **2010**, *10* (22), 3103. https://doi.org/10.1039/c005265e.
(57) Yobas, L.; Feng Cheow, L.; Tang, K.-C.; Yong, S.-E.; Kye-Zheng Ong, E.; Wong, L.; Cheng-Yong Teo, W.; Ji, H.; Rafeah, S.; Yu, C. A Self-Contained Fully-Enclosed Microfluidic Cartridge for Lab on a Chip. *Biomed Microdevices* **2009**, *11* (6), 1279–1288. https://doi.org/10.1007/s10544-009-9347-z.
(58) WHO COVID-19 Dashboard. https://data.who.int/dashboards/covid19/deaths (accessed 2024-04-17).
(59) Cardeñoso Domingo, L.; Roy Vallejo, E.; Zurita Cruz, N. D.; Chicot Llano, M.; Ávalos Pérez-Urria, E.; Barrios, A.; Hernando Santos, J.; Ortiz, J.; Rodríguez García, S. C.; Martín Ramírez, A.; Ciudad Sañudo, M.; Marcos, C.; García Castillo, E.; Fontán García-Rodrigo, L.; González, B.; Méndez, R.; Iturrate, I.; Sanz García, A.; Villa, A.; Sánchez Azofra, A.; Quicios, B.; Arribas, D.; Álvarez Rodríguez, J.; Patiño, P.; Trigueros, M.; Uriarte, M.; Triguero Martínez, A.; Arévalo, C.; Galván Román, J. M.; García-Vicuña, R.; Ancochea, J.; Soriano, J. B.; Canabal, A.; Muñoz Calleja, C.; De La Cámara, R.; Suarez Fernández, C.; González Álvaro, I.; Rodríguez-Serrano, D. A.; the PREDINMUN-COVID Group. Relevant SARS-CoV-2 Viremia Is Associated with COVID-19 Severity: Prospective Cohort Study and Validation Cohort. *Journal of Medical Virology* **2022**, *94* (11), 5260–5270. https://doi.org/10.1002/jmv.27989.
(60) Jacobs, J. L.; Bain, W.; Naqvi, A.; Staines, B.; Castanha, P. M. S.; Yang, H.; Boltz, V. F.; Barratt-Boyes, S.; Marques, E. T. A.; Mitchell, S. L.; Methé, B.; Olonisakin, T. F.; Haidar, G.; Burke, T. W.; Petzold, E.; Denny, T.; Woods, C. W.; McVerry, B. J.; Lee, J. S.; Watkins, S. C.; St Croix, C. M.; Morris, A.; Kearney, M. F.; Ladinsky, M. S.; Bjorkman, P. J.; Kitsios, G. D.; Mellors, J. W. Severe Acute Respiratory Syndrome Coronavirus 2 Viremia Is Associated With Coronavirus Disease 2019 Severity and Predicts Clinical Outcomes. *Clinical Infectious Diseases* **2022**, *74* (9), 1525–1533. https://doi.org/10.1093/cid/ciab686.
(61) Li, Y.; Schneider, A. M.; Mehta, A.; Sade-Feldman, M.; Kays, K. R.; Gentili, M.; Charland, N. C.; Gonye, A. L. K.; Gushterova, I.; Khanna, H. K.; LaSalle, T. J.; Lavin-Parsons, K. M.; Lilley, B. M.; Lodenstein, C. L.; Manakongtreecheep, K.; Margolin, J. D.; McKaig, B. N.; Parry, B. A.; Rojas-Lopez, M.; Russo, B. C.; Sharma, N.; Tantivit, J.; Thomas, M. F.; Regan, J.; Flynn, J. P.; Villani, A.-C.; Hacohen, N.; Goldberg, M. B.; Filbin, M. R.; Li, J. Z. SARS-CoV-2 Viremia Is Associated with Distinct Proteomic Pathways and Predicts COVID-19 Outcomes. *Journal of Clinical Investigation* **2021**, *131* (13), e148635. https://doi.org/10.1172/JCI148635.
(62) Fajnzylber, J.; Regan, J.; Coxen, K.; Corry, H.; Wong, C.; Rosenthal, A.; Worrall, D.; Giguel, F.; Piechocka-Trocha, A.; Atyeo, C.; Fischinger, S.; Chan, A.; Flaherty, K. T.; Hall, K.; Dougan, M.; Ryan, E. T.; Gillespie, E.; Chishti, R.;

Li, Y.; Jilg, N.; Hanidziar, D.; Baron, R. M.; Baden, L.; Tsibris, A. M.; Armstrong, K. A.; Kuritzkes, D. R.; Alter, G.; Walker, B. D.; Yu, X.; Li, J. Z.; The Massachusetts Consortium for Pathogen Readiness; Abayneh, B. A.; Allen, P.; Antille, D.; Balazs, A.; Bals, J.; Barbash, M.; Bartsch, Y.; Boucau, J.; Boyce, S.; Braley, J.; Branch, K.; Broderick, K.; Carney, J.; Chevalier, J.; Choudhary, M. C.; Chowdhury, N.; Cordwell, T.; Daley, G.; Davidson, S.; Desjardins, M.; Donahue, L.; Drew, D.; Einkauf, K.; Elizabeth, S.; Elliman, A.; Etemad, B.; Fallon, J.; Fedirko, L.; Finn, K.; Flannery, J.; Forde, P.; Garcia-Broncano, P.; Gettings, E.; Golan, D.; Goodman, K.; Griffin, A.; Grimmel, S.; Grinke, K.; Hartana, C. A.; Healy, M.; Heller, H.; Henault, D.; Holland, G.; Jiang, C.; Jordan, H.; Kaplonek, P.; Karlson, E. W.; Karpell, M.; Kayitesi, C.; Lam, E. C.; LaValle, V.; Lefteri, K.; Lian, X.; Lichterfeld, M.; Lingwood, D.; Liu, H.; Liu, J.; Lopez, K.; Lu, Y.; Luthern, S.; Ly, N. L.; MacGowan, M.; Magispoc, K.; Marchewka, J.; Martino, B.; McNamara, R.; Michell, A.; Millstrom, I.; Miranda, N.; Nambu, C.; Nelson, S.; Noone, M.; Novack, L.; O'Callaghan, C.; Ommerborn, C.; Osborn, M.; Pacheco, L. C.; Phan, N.; Pillai, S.; Porto, F. A.; Rassadkina, Y.; Reissis, A.; Ruzicka, F.; Seiger, K.; Selleck, K.; Sessa, L.; Sharpe, A.; Sharr, C.; Shin, S.; Singh, N.; Slaughenhaupt, S.; Sheppard, K. S.; Sun, W.; Sun, X.; Suschana, E.; Talabi, O.; Ticheli, H.; Weiss, S. T.; Wilson, V.; Zhu, A. SARS-CoV-2 Viral Load Is Associated with Increased Disease Severity and Mortality. *Nat Commun* **2020**, *11* (1), 5493. https://doi.org/10.1038/s41467-020-19057-5.

(63) Hogan, C. A.; Stevens, B. A.; Sahoo, M. K.; Huang, C.; Garamani, N.; Gombar, S.; Yamamoto, F.; Murugesan, K.; Kurzer, J.; Zehnder, J.; Pinsky, B. A. High Frequency of SARS-CoV-2 RNAemia and Association With Severe Disease. *Clinical Infectious Diseases* **2021**, *72* (9), e291–e295. https://doi.org/10.1093/cid/ciaa1054.

(64) Prebensen, C.; Myhre, P. L.; Jonassen, C.; Rangberg, A.; Blomfeldt, A.; Svensson, M.; Omland, T.; Berdal, J.-E. Severe Acute Respiratory Syndrome Coronavirus 2 RNA in Plasma Is Associated With Intensive Care Unit Admission and Mortality in Patients Hospitalized With Coronavirus Disease 2019. *Clinical Infectious Diseases* **2021**, *73* (3), e799–e802. https://doi.org/10.1093/cid/ciaa1338.

(65) Hagman, K.; Hedenstierna, M.; Rudling, J.; Gille-Johnson, P.; Hammas, B.; Grabbe, M.; Jakobsson, J.; Dillner, J.; Ursing, J. Duration of SARS-CoV-2 Viremia and Its Correlation to Mortality and Inflammatory Parameters in Patients Hospitalized for COVID-19: A Cohort Study. *Diagnostic Microbiology and Infectious Disease* **2022**, *102* (3), 115595. https://doi.org/10.1016/j.diagmicrobio.2021.115595.

(66) Al-Aly, Z.; Xie, Y.; Bowe, B. High-Dimensional Characterization of Post-Acute Sequelae of COVID-19. *Nature* **2021**, *594* (7862), 259–264. https://doi.org/10.1038/s41586-021-03553-9.

(67) Proal, A. D.; VanElzakker, M. B.; Aleman, S.; Bach, K.; Boribong, B. P.; Buggert, M.; Cherry, S.; Chertow, D. S.; Davies, H. E.; Dupont, C. L.; Deeks, S. G.; Eimer, W.; Ely, E. W.; Fasano, A.; Freire, M.; Geng, L. N.; Griffin, D. E.; Henrich, T. J.; Iwasaki, A.; Izquierdo-Garcia, D.; Locci, M.; Mehandru, S.;

Painter, M. M.; Peluso, M. J.; Pretorius, E.; Price, D. A.; Putrino, D.; Scheuermann, R. H.; Tan, G. S.; Tanzi, R. E.; VanBrocklin, H. F.; Yonker, L. M.; Wherry, E. J. SARS-CoV-2 Reservoir in Post-Acute Sequelae of COVID-19 (PASC). *Nat Immunol* **2023**, *24* (10), 1616–1627. https://doi.org/10.1038/s41590-023-01601-2.

(68) Thaweethai, T.; Jolley, S. E.; Karlson, E. W.; Levitan, E. B.; Levy, B.; McComsey, G. A.; McCorkell, L.; Nadkarni, G. N.; Parthasarathy, S.; Singh, U.; Walker, T. A.; Selvaggi, C. A.; Shinnick, D. J.; Schulte, C. C. M.; Atchley-Challenner, R.; Horwitz, L. I.; Foulkes, A. S.; RECOVER Consortium Authors; RECOVER Consortium; Aberg, J. A.; Adolphi, N. L.; Ahirwar, S.; Ahmed, S.; Ahuja, N.; Aikawa, M.; Akerlundh, A.; Akintonwa, T. T.; Al-Jadiri, A.; Alekhina, N.; Algren, H. A.; Alshawabkeh, A. N.; Ammar, N.; Anand, A.; Anderson, B. R.; Aponte-Soto, L.; Aschner, J. L.; Atha, M. M.; Atz, A. M.; Aupperle, R. L.; Ayache, M.; Azziz-Baumgartner, E.; Bailey, L. C.; Baker, F. C.; Balaraman, V.; Bandy, J. A.; Banerjee, D.; Barch, D. M.; Bardes, J. M.; Barlocker, J.; Barr, R. G.; Baskin-Sommers, A.; Basu, S.; Battaglia, T. A.; Baucom, L.; Beamon, C. J.; Beaty, C. L.; Beckmann, N. D.; Berry, J. A.; Bhadelia, N.; Bhargava, D.; Bhuiyan, S.; Bian, J.; Bime, C.; Bjork, J. M.; Black, L. J.; Blish, C. A.; Block, J. P.; Bogie, A.; Bolliger, D.; Bonaventura, W.; Bose-Brill, S.; Bower, M. B.; Boyd, A. D.; Boyineni, J.; Bradfute, S. B.; Bramante, C. T.; Brannock, M. D.; Bremner, J. D.; Brosnahan, S. B.; Buchbinder, N. C.; Bueler, E.; Buhimschi, I. A.; Bukulmez, H.; Bunnell, H. T.; Buse, J. B.; Calhoun, E. A.; Cao, T.; Carrithers, M. D.; Carton, T. W.; Case, A.; Casey, B. J.; Casimero, F. V. C.; Castro, L.; Cato, T.; Ceger, P.; Cerullo, C. L.; Chang, L.; Chang, A. A.; Chebrolu, P.; Chen, Y.; Chen, L. Q.; Chen, B. K.; Chestek, D.; Chew, R. F.; Chisolm, D. J.; Chow, D. C.; Chrisant, M. R.; Christakis, D. A.; Chute, C. G.; Cicek, M. S.; Clark, C. R.; Clark, D. B.; Clarke, G. D.; Clouser, K. N.; Connors, T. J.; Cook, J. A.; Coombs, K.; Cordon-Cardo, C.; Costello, J. L.; Cottrell, L.; Cowan, K.; Cowell, L. G.; Cranford, S.; Cronin, J.; Cummins, M. R.; Curry, H. L.; D'Sa, V.; Dabney, S. G.; Daniel, C. L.; Dapretto, M.; Darbar, D.; Darden, P. M.; Dasgupta, R.; Dasgupta, S.; Davis Blakley, F.; Dea, K.; Deakyne Davies, S. J.; Decker, L. A.; DeFronzo, R. A.; Dehority, W.; Deitchman, A. N.; Del Alcazar, J.; Del Boccio, P.; Del Rio, C.; Del Rios, M.; DeLisa, J. A.; Deoni, S. C.; Diaz, M. Z.; Dickinson, J. D.; Dionne, A.; Diviak, K. R.; Donohue, S. E.; Downey, M. J.; Dozor, A. J.; Dreyer, B. P.; Dummer, K. B.; Durstenfeld, M. S.; Dworkin, M. S.; Edmonds, S. L.; Elias, M. D.; Elifritz, J.; Ellingworth, E.; Elliott, A. J.; Ellison, A. M.; Enger, M. L.; Espinosa, J. M.; Esquenazi-Karonika, S.; Evans, M. D.; Evans, D. N.; Facelli, J. C.; Fang, C. S.; Faustino, E. V. S.; Fayad Lara, M. E.; Feldman, C. H.; Fiks, A. G.; Fineman, R.; Finn, A. V.; Fischer, M. S.; Fitzgerald, M. L.; Flaherman, V. J.; Flotte, T. J.; Forsha, D.; Fortune, M. R.; Foxe, J. J.; Franks, N.; Freedman, M. B.; Freeland, C. E.; Friedman, N. P.; Fry, G.; Gage Witvliet, M.; Gallagher, E. J.; Gallagher, R.; Garavan, H.; Gaur, S. M.; Gee, D. G.; Gennaro, M. L.; Gerald, L. B.; Ghosh, S. B.; Giacino, J. T.; Girvin, A. T.; Godfrey, S. L.; Goldberg, M. P.; Goodman, S. N.; Gordon, H. S.; Gouripeddi, R.; Graham, P.; Granger, J. P.; Gray, K. M.; Greimes, T.; Gross, R. S.; Guthe, N.; Gutter, E.; Haasnoot, S.; Hadley, E. C.;

Haendel, M. A.; Hafner, S.; Halabi, K. C.; Hanley, P. C.; Harahsheh, A. S.; Harkins, M. S.; Hartwig, K. L.; Hasbani, K.; Hasek, S.; Hauser, K. S.; Heath, A. C.; Hebson, C. L.; Heitzeg, M. M.; Hendrickson, M.; Henrich, T. J.; Hernandez-Romieu, A. C.; Hester, C. M.; Higginbotham, M.; Hill, S.; Hirabayashi, K.; Ho, O.; Hobart-Porter, L.; Hoffman, M. C.; Holtcamp, M.; Hong, T. K.; Horne, B. D.; Horowitz, C. R.; Hsia, D. S.; Hsu, H.; Hsue, P. Y.; Huentelman, M.; Huerta, B. E.; Huling, J. D.; Hummel, K.; Iacono, W. G.; Ibanez, A. L.; Ibeawuchi, C.; Irby, K.; Ismail, N.; Jacobus, J.; Jacoby, V. L.; Jason, L. A.; Javia, V.; Jennette, K. J.; Jernigan, T. L.; Jiang, S.; Jing, N.; Johnny, J. D.; Johnson, N.; Johnson, B.; Johnson, B.; Jone, P.-N.; Judd, S. E.; Juskowich, J. J.; Kabagambe, E. K.; Kaelber, D. C.; Kanjilal, D. G.; Kansal, M. M.; Kasmarcak, T. J.; Kaufman, D.; Kawakami, R.; Kellogg, D. L.; Kent, D. A.; Kewlani, D.; Khullar, D.; Kim, K. S.; Kim, A. Y.; Kinser, P. A.; Kleinman, L. C.; Klerman, E. B.; Kluko, M. J.; Knight, S.; Kobayashi, M.; Kopp, K. J.; Koropsak, M.; Kosut, J. S.; Kraig, E.; Krausert, A.; Krieger, A. C.; Krishna, H.; Krishnamoorthy, A.; Krishnan, S. S.; Lahs, J. P.; Laird, A. R.; Laleau, V.; Lamendola-Essel, M. F.; Landeo-Gutierrez, J.; Lang, S. M.; Larson, C. L.; Lash, J. P.; Lasky-Su, J.; Laynor, G.; Lee, S.; Lee, G. M.; Lee, F. E.; Lee, M. A.; Leese, P. J.; Lefebvre, R. C.; Levreault, A. J.; Lewis, K. C.; Li, L.; Lim, P. P. C.; Lin, J. Y.; Lisdahl, K. M.; Litvack, M. B.; Liu, X.; Lloyd, J.; Logue, J. K.; Loomba, J. J.; Lorman, V.; Lu, Y.; Ludwig, K. R.; Lutz, A. M.; Mack, J.; Mahmoud, A. M.; Maier, C. L.; Malakooti, S. K.; Malchenko, S.; Mallett, G. L.; Maranga, G.; Martel, M. W.; Martin-Herz, S. P.; Martinez-Lage, M.; Maughan, C.; Mauntel-Medici, C.; May, H. T.; Mayer, K. H.; Mazzotti, D. R.; McCallum, C. M.; McCrindle, B. W.; McCulloh, R. J.; McDonald, D.; McInnis, S.; McMurry, J. A.; Mejias, A.; Melamed, J.; Menchaca, M.; Mendelsohn, A. L.; Miele, L.; Miglis, M. G.; Milne, C.; Milner, J. D.; Mitchell, R. A.; Mittleman, M. A.; Mohandas, S.; Monteiro, J. G.; Monzon, V.; Moreno, D. J.; Morgan, L. M.; Morozyuk, D.; Morse, K. E.; Moyneur, E.; Mudumbi, P. C.; Müller-Oehring, E. M.; Muramatsu, N.; Musick, H.; Nagavedu, K.; Nahin, E. R.; Nambiar, A. M.; Natelson, B. H.; Neale, M. C.; Ness-Cochinwala, M.; Newburger, J. W.; Newman, L. T.; Nguyen, A. N.; Nichols, L.; Nolan, S. M.; Noland, S.; Novak, R. M.; O'Connor, G. T.; O'Keefe, J. J.; Ogbogu, P. U.; Oliveira, C. R.; Oster, M. E.; Padera, R. F.; Paik, H. H.; Pajor, N. M.; Pan, H. H.; Pant, D.; Partridge, A.; Patel, P. B.; Patel, S.; Patel, K.; Paulus, M. P.; Payne, R. M.; Pearman, A.; Peralta-Carcelen, M.; Perez, N. L.; Pfaff, E. R.; Pillers, D.-A. M.; Pitsch, C. E.; Pliskin, N. H.; Portman, M. A.; Postelnicu, R.; Potter, J. S.; Prabhakar, B. S.; Prahalad, P.; Prasad, B.; Predki, B.; Preiss, A. J.; Prendergast, H. M.; Quinn, D. K.; Quintana, Y.; Rabideau, D. J.; Radosta, J. M.; Radwell, J.; Raissy, H.; Ramchandran, R.; Randall, I.; Rao, S.; Rapkiewicz, A.; Rasmussen, S. A.; Razzaghi, H.; Rebello, C. J.; Rebolledo, P. A.; Reddy, N. V.; Reddy, U. M.; Reedy, C.; Rehman, J.; Reichard, R. R.; Reid, K. M.; Reusch, J. E.; Rhee, K. E.; Rice, M. B.; Rizzo, J.-R. R.; Roan, N. R.; Robarts, P.; Roberts, T. R.; Rochez, N.; Rodgers, K. E.; Rogerson, C. M.; Romero, M. E.; Rosas, J. M.; Rosenzweig, E. B.; Rothman, R. L.; Rouphael, N. G.; Russell, M. W.; Rutherfoord, M.; Sabati, A. A.; Sader, S. B.; Salehi, M.; Salisbury, A. L.; Sampson, B. A.; Sanil, Y.; Sato, A. I.; Saydah, S. H.;

Schechter, M. S.; Schenck, E. J.; Schlepphorst, K. I.; Schuchard, J.; Schuh, T. L.; Sculley, J. A.; Seifert, A. C.; Sekar, A. K.; Selvarangan, R.; Seshadri, S.; Sesso, H. D.; Shah, D. P.; Shakti, D.; Shapiro, N. L.; Sharma, S.; Sharma, K.; Sharma, S.; Sharma, K.; Shaw, G.; Shemesh, E.; Shen, Y.; Shenkman, E.; Shiau, S.; Siciliano, M.; Simsir, A.; Smith, V. E.; Snowden, J. N.; Solomon, I. H.; Spikes, L. A.; Squeglia, L. M.; Srivastava, S.; St. Jean, M. L.; Stapleford, K. A.; Stein, C. R.; Stevenson, M. D.; Stewart De Ramirez, S. A.; Stiles, L. E.; Stock, A.; Stockwell, M. S.; Stone, J. R.; Stratford, J.; Stürmer, T.; Subbian, V.; Sun, J.; Suthar, M. S.; Sylvera, A.; Systrom, D. M.; Szmuszkovicz, J.; Talavera-Barber, M. M.; Tantisira, K. G.; Tartt, N.; Terlinde, T.; Teufel, R. J.; Thacker, D.; Thakrar, M.; Thibodeau, S. N.; Thomas, G. L.; Thomason, M. E.; Tong, J.; Torres, R.; Traenkner, J.; Tragus, R.; Trinity, J. D.; Tronieri, J. S.; Troxel, A. B.; Truong, J.; Truong, D. T.; Tsevat, J.; Udosen, M. M.; Unterberger, K.; Utz, P. J.; Vaccarino, V.; Vallejos, B. B.; Vanden Hoek, T. L.; Vangeepuram, N.; Varma, J. K.; Vernon, S. D.; Vidal, C. M.; Vivensi, S.; Vohra, A. S.; Wagner, L. K.; Wang, F.; Warburton, D.; Warner, M. R.; Watkins, R. L.; Watson, S. E.; Webb, R.; Weeks, R. M.; Weiner, M. G.; Werzberger, A.; West, S. C.; Weyer, J. C.; Wheeler, J. L.; Wilkins, K. J.; Williams, N. J.; Williams, C. T.; Wimberly, E. S.; Winter, T. J.; Woller, S. C.; Wong, R.; Wood, J. P.; Wood, J. C.; Wood, M. J. J.; Wu, Q.; Xia, Y.; Xu, J.; Yang, S.; Yin, H. S.; Yin, H. S.; Yoo, Y. J.; Young, C. E.; Young, N. M.; Zang, C.; Zempsky, W. T.; Zhang, B.; Zhang, Y.; Zhang, D.; Zimmerman, E.; Andrefsky, J.; Marrazzo, J. M.; Dixon, J.; Gale, L.; Maholovich, P.; Sudhindra, P.; Thompson, T.; Sheehan, E.; Parada, A.; Knowlton, K.; Anderson, J. L.; McIntyre, M.; McCandless, S.; Montoya, S.; Davis, D.; Spanier, E.; Wodushek, T.; Sokol, R.; Maldonado, Y.; Jacobson, K.; Jia, X. “Kathleen”; Scott, J.; Quintero, O.; Haddad, F.; Valantine, H.; Zamanian, R.; Pathak, D.; Boyce, J.; Facco, F.; Hankle, S.; Vargo, J. A.; Campbell, D.; Armstrong, D.; Mann, M.; Burrell, N.; Bartholomew, A.; Grobman, W. A.; Cackovic, B.; Klopfenstein, B.; Weigand, S.; Snow, E. K.; Fennig, K.; Esplin, M. S.; Lamb, D.; Nelsen, A.; Phipers, J.; Fischer, L.; Docter, O.; Brown, J.; DeMartino, A.; Allard, D.; Miller, E.; Bousleiman, S. Z.; Loffredo, M. M.; Vanneman, A.; Beche, I.; Chan-Akeley, R.; Pacheco, L. D.; DeVolder, J. D.; Salazar, A.; Thibodeaux, L.; Cornwell, J.; Nounes, A. A.; Sweet, E.; Pierse, A.; Desantis, B.; Gill-Jones, P.; Hackney, D. N.; Chauhan, S. P.; Ortiz, F.; Treadway, J.; Rugerio, J.; Clark, K.; Leatherland, M.; Timlin, S.; Grinnan, C.; Ferrara, J.; Kominiarek, M.; Jones, D.; Reynolds, T.; Kearns, K. M.; Saffian, E.; Karasti, M.; Pizzi, C.; Filipczak, A.; Long, E.; Mitchell, M.; Barrett, K. J.; Mullowney, C.; Macones, G. A.; Alba, G. A.; Alicic, R.; Altman, N.; Anglin, K.; Argueta, U.; Ashktorab, H.; Baslet, G.; Bassett, I. V.; Bateman, L.; Bedi, B.; Bhattacharyya, S.; Bind, M.-A.; Blomkalns, A. L.; Bonilla, H.; Brim, H.; Bush, P. A.; Castro, M.; Chan, J.; Charney, A. W.; Chen, P.; Chibnik, L. B.; Chu, H. Y.; Clifton, R. G.; Costantine, M. M.; Cribbs, S. K.; Davila Nieves, S. I.; Deeks, S. G.; Duven, A.; Emery, I. F.; Erdmann, N.; Erlandson, K. M.; Ernst, K. C.; Farah-Abraham, R.; Farner, C. E.; Feuerriegel, E. M.; Fleurimont, J.; Fonseca, V.; Franko, N.; Gainer, V.; Gander, J. C.; Gardner, E. M.; Geng, L. N.; Gibson, K. S.; Go, M.; Goldman, J. D.; Grebe, H.; Greenway, F. L.; Habli, M.; Hafner,

J.; Han, J. E.; Hanson, K. A.; Heath, J.; Hernandez, C.; Hess, R.; Hodder, S. L.; Hoffman, M. K.; Hoover, S. E.; Huang, B.; Hughes, B. L.; Jagannathan, P.; John, J.; Jordan, M. R.; Katz, S. D.; Kaufman, E. S.; Kelly, J. D.; Kelly, S. W.; Kemp, M. M.; Kirwan, J. P.; Klein, J. D.; Knox, K. S.; Krishnan, J. A.; Kumar, A.; Laiyemo, A. O.; Lambert, A. A.; Lanca, M.; Lee-Iannotti, J. K.; Logarbo, B. P.; Longo, M. T.; Luciano, C. A.; Lutrick, K.; Maley, J. H.; Mallett, G.; Marathe, J. G.; Marconi, V.; Marshall, G. D.; Martin, C. F.; Matusov, Y.; Mehari, A.; Mendez-Figueroa, H.; Mermelstein, R.; Metz, T. D.; Morse, R.; Mosier, J.; Mouchati, C.; Mullington, J.; Murphy, S. N.; Neuman, R. B.; Nikolich, J. Z.; Ofotokun, I.; Ojemakinde, E.; Palatnik, A.; Palomares, K.; Parimon, T.; Parry, S.; Patterson, J. E.; Patterson, T. F.; Patzer, R. E.; Peluso, M. J.; Pemu, P.; Pettker, C. M.; Plunkett, B. A.; Pogreba-Brown, K.; Poppas, A.; Quigley, J. G.; Reddy, U.; Reece, R.; Reeder, H.; Reeves, W. B.; Reiman, E. M.; Rischard, F.; Rosand, J.; Rouse, D. J.; Ruff, A.; Saade, G.; Sandoval, G. J.; Santana, J. L.; Schlater, S. M.; Sciurba, F. C.; Shepherd, F.; Sherif, Z. A.; Simhan, H.; Singer, N. G.; Skupski, D. W.; Sowles, A.; Sparks, J. A.; Sukhera, F. I.; Taylor, B. S.; Teunis, L.; Thomas, R. J.; Thorp, J. M.; Thuluvath, P.; Ticotsky, A.; Tita, A. T.; Tuttle, K. R.; Urdaneta, A. E.; Valdivieso, D.; VanWagoner, T. M.; Vasey, A.; Verduzco-Gutierrez, M.; Wallace, Z. S.; Ward, H. D.; Warren, D. E.; Weiner, S. J.; Welch, S.; Whiteheart, S. W.; Wiley, Z.; Wisnivesky, J. P.; Yee, L. M.; Zisis, S. Development of a Definition of Postacute Sequelae of SARS-CoV-2 Infection. *JAMA* **2023**, *329* (22), 1934. https://doi.org/10.1001/jama.2023.8823.

(69) Su, Y.; Yuan, D.; Chen, D. G.; Ng, R. H.; Wang, K.; Choi, J.; Li, S.; Hong, S.; Zhang, R.; Xie, J.; Kornilov, S. A.; Scherler, K.; Pavlovitch-Bedzyk, A. J.; Dong, S.; Lausted, C.; Lee, I.; Fallen, S.; Dai, C. L.; Baloni, P.; Smith, B.; Duvvuri, V. R.; Anderson, K. G.; Li, J.; Yang, F.; Duncombe, C. J.; McCulloch, D. J.; Rostomily, C.; Troisch, P.; Zhou, J.; Mackay, S.; DeGottardi, Q.; May, D. H.; Taniguchi, R.; Gittelman, R. M.; Klinger, M.; Snyder, T. M.; Roper, R.; Wojciechowska, G.; Murray, K.; Edmark, R.; Evans, S.; Jones, L.; Zhou, Y.; Rowen, L.; Liu, R.; Chour, W.; Algren, H. A.; Berrington, W. R.; Wallick, J. A.; Cochran, R. A.; Micikas, M. E.; Wrin, T.; Petropoulos, C. J.; Cole, H. R.; Fischer, T. D.; Wei, W.; Hoon, D. S. B.; Price, N. D.; Subramanian, N.; Hill, J. A.; Hadlock, J.; Magis, A. T.; Ribas, A.; Lanier, L. L.; Boyd, S. D.; Bluestone, J. A.; Chu, H.; Hood, L.; Gottardo, R.; Greenberg, P. D.; Davis, M. M.; Goldman, J. D.; Heath, J. R. Multiple Early Factors Anticipate Post-Acute COVID-19 Sequelae. *Cell* **2022**, *185* (5), 881-895.e20. https://doi.org/10.1016/j.cell.2022.01.014.

(70) Craddock, V.; Mahajan, A.; Spikes, L.; Krishnamachary, B.; Ram, A. K.; Kumar, A.; Chen, L.; Chalise, P.; Dhillon, N. K. Persistent Circulation of Soluble and Extracellular Vesicle-linked Spike Protein in Individuals with Postacute Sequelae of COVID-19. *Journal of Medical Virology* **2023**, *95* (2), e28568. https://doi.org/10.1002/jmv.28568.

(71) Siddiqi, H. K.; Weber, B.; Zhou, G.; Regan, J.; Fajnzylber, J.; Coxen, K.; Corry, H.; Yu, X. G.; DiCarli, M.; Li, J. Z.; Bhatt, D. L. Increased Prevalence of Myocardial Injury in Patients with SARS-CoV-2 Viremia. *The American*

Journal of Medicine **2021**, *134* (4), 542–546. https://doi.org/10.1016/j.amjmed.2020.09.046.
(72) Goertz, J. P.; White, I. M. Phase-Change Partitions for Thermal Automation of Multistep Reactions. *Anal. Chem.* **2018**, *90* (6), 3708–3713. https://doi.org/10.1021/acs.analchem.7b05400.
(73) Goertz, J.; Lippe, A.; White, I. Thermally-Triggered Effervescent Mixing for Assay Automation. September 18, 2018. https://doi.org/10.26434/chemrxiv.7094297.v1.
(74) Everitt, M. L.; Boegner, D. J.; Birukov, K. G.; White, I. M. Sample-to-Answer Diagnostic System for the Detection of Circulating Histones in Whole Blood. *ACS Sens.* **2021**, *6* (8), 3006–3012. https://doi.org/10.1021/acssensors.1c00886.
(75) Ferguson, B. S.; Buchsbaum, S. F.; Wu, T.-T.; Hsieh, K.; Xiao, Y.; Sun, R.; Soh, H. T. Genetic Analysis of H1N1 Influenza Virus from Throat Swab Samples in a Microfluidic System for Point-of-Care Diagnostics. *J. Am. Chem. Soc.* **2011**, *133* (23), 9129–9135. https://doi.org/10.1021/ja203981w.
(76) Cao, Q.; Mahalanabis, M.; Chang, J.; Carey, B.; Hsieh, C.; Stanley, A.; Odell, C. A.; Mitchell, P.; Feldman, J.; Pollock, N. R.; Klapperich, C. M. Microfluidic Chip for Molecular Amplification of Influenza A RNA in Human Respiratory Specimens. *PLoS ONE* **2012**, *7* (3), e33176. https://doi.org/10.1371/journal.pone.0033176.
(77) Hagan, K. A.; Reedy, C. R.; Uchimoto, M. L.; Basu, D.; Engel, D. A.; Landers, J. P. An Integrated, Valveless System for Microfluidic Purification and Reverse Transcription-PCR Amplification of RNA for Detection of Infectious Agents. *Lab Chip* **2011**, *11* (5), 957–961. https://doi.org/10.1039/C0LC00136H.
(78) Shen, K.-M.; Sabbavarapu, N. M.; Fu, C.-Y.; Jan, J.-T.; Wang, J.-R.; Hung, S.-C.; Lee, G.-B. An Integrated Microfluidic System for Rapid Detection and Multiple Subtyping of Influenza A Viruses by Using Glycan-Coated Magnetic Beads and RT-PCR. *Lab Chip* **2019**, *19* (7), 1277–1286. https://doi.org/10.1039/C8LC01369A.
(79) Choi, G.; Song, D.; Shrestha, S.; Miao, J.; Cui, L.; Guan, W. A Field-Deployable Mobile Molecular Diagnostic System for Malaria at the Point of Need. *Lab Chip* **2016**, *16* (22), 4341–4349. https://doi.org/10.1039/C6LC01078D.
(80) Jung, C.; Chung, J. W.; Kim, U. O.; Kim, M. H.; Park, H. G. Isothermal Target and Signaling Probe Amplification Method, Based on a Combination of an Isothermal Chain Amplification Technique and a Fluorescence Resonance Energy Transfer Cycling Probe Technology. *Anal. Chem.* **2010**, *82* (14), 5937–5943. https://doi.org/10.1021/ac100606m.
(81) Tang, Z.; Cui, J.; Kshirsagar, A.; Liu, T.; Yon, M.; Kuchipudi, S. V.; Guan, W. SLIDE: Saliva-Based SARS-CoV-2 Self-Testing with RT-LAMP in a Mobile Device. *ACS Sens.* **2022**, *7* (8), 2370–2378. https://doi.org/10.1021/acssensors.2c01023.
(82) Kshirsagar, A.; Choi, G.; Santosh, V.; Harvey, T.; Bernhards, R. C.; Guan, W. Handheld Purification-Free Nucleic Acid Testing Device for Point-of-Need Detection of Malaria from Whole Blood. *ACS Sens.* **2023**, *8* (2), 673–683. https://doi.org/10.1021/acssensors.2c02169.

(83) Changtor, P.; Rodriguez-Mateos, P.; Buddhachat, K.; Wattanachaiyingcharoen, W.; Iles, A.; Kerdphon, S.; Yimtragool, N.; Pamme, N. Integration of IFAST-Based Nucleic Acid Extraction and LAMP for on-Chip Rapid Detection of Agroathelia Rolfsii in Soil. *Biosensors and Bioelectronics* **2024**, *250*, 116051. https://doi.org/10.1016/j.bios.2024.116051.
(84) Liu, T.; Choi, G.; Tang, Z.; Kshirsagar, A.; Politza, A. J.; Guan, W. Fingerpick Blood-Based Nucleic Acid Testing on A USB Interfaced Device towards HIV Self-Testing. *Biosensors and Bioelectronics* **2022**, *209*, 114255. https://doi.org/10.1016/j.bios.2022.114255.
(85) Ngo, H. T.; Jin, M.; Trick, A. Y.; Chen, F.-E.; Chen, L.; Hsieh, K.; Wang, T.-H. Sensitive and Quantitative Point-of-Care HIV Viral Load Quantification from Blood Using a Power-Free Plasma Separation and Portable Magnetofluidic Polymerase Chain Reaction Instrument. *Anal. Chem.* **2022**, acs.analchem.2c03897. https://doi.org/10.1021/acs.analchem.2c03897.
(86) Trick, A. Y.; Ngo, H. T.; Nambiar, A. H.; Morakis, M. M.; Chen, F.-E.; Chen, L.; Hsieh, K.; Wang, T.-H. Filtration-Assisted Magnetofluidic Cartridge Platform for HIV RNA Detection from Blood. *Lab Chip* **2022**, *22* (5), 945–953. https://doi.org/10.1039/D1LC00820J.
(87) Boegner, D. J.; Everitt, M. L.; White, I. M. Thermally Responsive Alkane Partitions for Assay Automation. *ACS Appl. Mater. Interfaces* **2022**, *14* (7), 8865–8875. https://doi.org/10.1021/acsami.2c00493.
(88) Everitt, M. L.; Boegner, D. J.; White, I. M. Sample-to-Answer Immuno-Magnetic Assay Using Thermally Responsive Alkane Partitions. *Biosensors* **2022**, *12* (11), 1030. https://doi.org/10.3390/bios12111030.
(89) Song, Y.; Song, J.; Wei, X.; Huang, M.; Sun, M.; Zhu, L.; Lin, B.; Shen, H.; Zhu, Z.; Yang, C. Discovery of Aptamers Targeting the Receptor-Binding Domain of the SARS-CoV-2 Spike Glycoprotein. *Anal. Chem.* **2020**, *92* (14), 9895–9900. https://doi.org/10.1021/acs.analchem.0c01394.
(90) Huang, W. E.; Lim, B.; Hsu, C.; Xiong, D.; Wu, W.; Yu, Y.; Jia, H.; Wang, Y.; Zeng, Y.; Ji, M.; Chang, H.; Zhang, X.; Wang, H.; Cui, Z. RT-LAMP for Rapid Diagnosis of Coronavirus SARS-CoV-2. *Microbial Biotechnology* **2020**, *13* (4), 950–961. https://doi.org/10.1111/1751-7915.13586.
(91) Vogels, C. B. F.; Watkins, A. E.; Harden, C. A.; Brackney, D. E.; Shafer, J.; Wang, J.; Caraballo, C.; Kalinich, C. C.; Ott, I. M.; Fauver, J. R.; Kudo, E.; Lu, P.; Venkataraman, A.; Tokuyama, M.; Moore, A. J.; Muenker, M. C.; Casanovas-Massana, A.; Fournier, J.; Bermejo, S.; Campbell, M.; Datta, R.; Nelson, A.; Dela Cruz, C. S.; Ko, A. I.; Iwasaki, A.; Krumholz, H. M.; Matheus, J. D.; Hui, P.; Liu, C.; Farhadian, S. F.; Sikka, R.; Wyllie, A. L.; Grubaugh, N. D.; Anastasio, K.; Askenase, M. H.; Batsu, M.; Bickerton, S.; Brower, K.; Bucklin, M. L.; Cahill, S.; Cao, Y.; Courchaine, E.; DeIuliis, G.; Earnest, R.; Geng, B.; Goldman-Israelow, B.; Handoko, R.; Khoury-Hanold, W.; Kim, D.; Knaggs, L.; Kuang, M.; Lapidus, S.; Lim, J.; Linehan, M.; Lu-Culligan, A.; Martin, A.; Matos, I.; McDonald, D.; Minasyan, M.; Nakahata, M.; Naushad, N.; Nouws, J.; Obaid, A.; Odio, C.; Oh, J. E.; Omer, S.; Park, A.; Park, H.-J.; Peng, X.; Petrone, M.; Prophet, S.; Rice, T.; Rose, K.-A.; Sewanan, L.; Sharma, L.; Shaw, A. C.; Shepard, D.; Smolgovsky, M.; Sonnert, N.; Strong, Y.;

Todeasa, C.; Valdez, J.; Velazquez, S.; Vijayakumar, P.; White, E. B.; Yang, Y. SalivaDirect: A Simplified and Flexible Platform to Enhance SARS-CoV-2 Testing Capacity. *Med* **2021**, *2* (3), 263-280.e6. https://doi.org/10.1016/j.medj.2020.12.010.
(92) Davis, H. E.; McCorkell, L.; Vogel, J. M.; Topol, E. J. Long COVID: Major Findings, Mechanisms and Recommendations. *Nat Rev Microbiol* **2023**, *21* (3), 133–146. https://doi.org/10.1038/s41579-022-00846-2.
(93) Cutler, D. M.; Summers, L. H. The COVID-19 Pandemic and the $16 Trillion Virus. *JAMA* **2020**, *324* (15), 1495. https://doi.org/10.1001/jama.2020.19759.
(94) Murshed, S. M. Consequences of the Covid-19 Pandemic for Economic Inequality. In *COVID-19 and International Development*; Papyrakis, E., Ed.; Springer International Publishing: Cham, 2022; pp 59–70. https://doi.org/10.1007/978-3-030-82339-9_5.
(95) Bambra, C.; Riordan, R.; Ford, J.; Matthews, F. The COVID-19 Pandemic and Health Inequalities. *J Epidemiol Community Health* **2020**, jech-2020-214401. https://doi.org/10.1136/jech-2020-214401.
(96) Engzell, P.; Frey, A.; Verhagen, M. D. Learning Loss Due to School Closures during the COVID-19 Pandemic. *Proc. Natl. Acad. Sci. U.S.A.* **2021**, *118* (17), e2022376118. https://doi.org/10.1073/pnas.2022376118.
(97) *Disease Control Priorities, Third Edition (Volume 9): Improving Health and Reducing Poverty*; Jamison, D. T., Gelband, H., Horton, S., Jha, P., Laxminarayan, R., Mock, C. N., Nugent, R., Eds.; The World Bank, 2017. https://doi.org/10.1596/978-1-4648-0527-1.
(98) Tan, S. H.; Allicock, O.; Armstrong-Hough, M.; Wyllie, A. L. Saliva as a Gold-Standard Sample for SARS-CoV-2 Detection. *The Lancet Respiratory Medicine* **2021**, *9* (6), 562–564. https://doi.org/10.1016/S2213-2600(21)00178-8.
(99) Williams, E.; Bond, K.; Zhang, B.; Putland, M.; Williamson, D. A. Saliva as a Noninvasive Specimen for Detection of SARS-CoV-2. *J Clin Microbiol* **2020**, *58* (8), e00776-20. https://doi.org/10.1128/JCM.00776-20.
(100) Azzi, L.; Carcano, G.; Gianfagna, F.; Grossi, P.; Gasperina, D. D.; Genoni, A.; Fasano, M.; Sessa, F.; Tettamanti, L.; Carinci, F.; Maurino, V.; Rossi, A.; Tagliabue, A.; Baj, A. Saliva Is a Reliable Tool to Detect SARS-CoV-2. *Journal of Infection* **2020**, *81* (1), e45–e50. https://doi.org/10.1016/j.jinf.2020.04.005.
(101) Landry, M. L.; Criscuolo, J.; Peaper, D. R. Challenges in Use of Saliva for Detection of SARS CoV-2 RNA in Symptomatic Outpatients. *Journal of Clinical Virology* **2020**, *130*, 104567. https://doi.org/10.1016/j.jcv.2020.104567.
(102) Ganguli, A.; Mostafa, A.; Berger, J.; Lim, J.; Araud, E.; Baek, J.; Stewart De Ramirez, S. A.; Baltaji, A.; Roth, K.; Aamir, M.; Aedma, S.; Mady, M.; Mahajan, P.; Sathe, S.; Johnson, M.; White, K.; Kumar, J.; Valera, E.; Bashir, R. Reverse Transcription Loop-Mediated Isothermal Amplification Assay for Ultrasensitive Detection of SARS-CoV-2 in Saliva and Viral Transport Medium Clinical Samples. *Anal. Chem.* **2021**, *93* (22), 7797–7807. https://doi.org/10.1021/acs.analchem.0c05170.
(103) Ter-Ovanesyan, D.; Gilboa, T.; Lazarovits, R.; Rosenthal, A.; Yu, X.; Li, J. Z.; Church, G. M.; Walt, D. R. Ultrasensitive Measurement of Both SARS-CoV-

2 RNA and Antibodies from Saliva. *Anal. Chem.* **2021**, *93* (13), 5365–5370. https://doi.org/10.1021/acs.analchem.1c00515.
(104) Rao, M.; Rashid, F. A.; Sabri, F. S. A. H.; Jamil, N. N.; Zain, R.; Hashim, R.; Amran, F.; Kok, H. T.; Samad, M. A. A.; Ahmad, N. Comparing Nasopharyngeal Swab and Early Morning Saliva for the Identification of Severe Acute Respiratory Syndrome Coronavirus 2 (SARS-CoV-2). *Clinical Infectious Diseases* **2021**, *72* (9), e352–e356. https://doi.org/10.1093/cid/ciaa1156.
(105) Zhang, J.; Xu, L.; Sheng, Z.; Zheng, J.; Chen, W.; Hu, Q.; Shen, F. Combination-Lock SlipChip Integrating Nucleic Acid Sample Preparation and Isothermal LAMP Amplification for the Detection of SARS-CoV-2. *ACS Sens.* **2024**, *9* (2), 646–653. https://doi.org/10.1021/acssensors.3c01727.
(106) Priye, A.; Bird, S. W.; Light, Y. K.; Ball, C. S.; Negrete, O. A.; Meagher, R. J. A Smartphone-Based Diagnostic Platform for Rapid Detection of Zika, Chikungunya, and Dengue Viruses. *Sci Rep* **2017**, *7* (1), 44778. https://doi.org/10.1038/srep44778.